

The Modern-Era Retrospective Analysis for Research and Applications, Version 2 (MERRA-2)

Ronald Gelaro¹, Will McCarty¹, Max J. Suárez², Ricardo Todling¹, Andrea Molod¹,
Lawrence Takacs³, Cynthia Randles^{4†}, Anton Darmenov¹, Michael G. Bosilovich¹, Rolf
Reichle¹, Krzysztof Wargan³, Lawrence Coy³, Richard Cullather⁵, Clara Draper²,
Santha Akella³, Virginie Buchard², Austin Conaty³, Arlindo da Silva¹, Wei Gu³,
Gi-Kong Kim¹, Randal Koster¹, Robert Lucchesi³, Dagmar Merkova^{3‡}, Jon Eric
Nielsen³, Gary Partyka³, Steven Pawson¹, William Putman¹, Michele Rienecker¹,
Siegfried D. Schubert¹, Meta Sienkiewicz³, and Bin Zhao⁶

¹*Global Modeling and Assimilation Office, NASA Goddard Space Flight Center,
Greenbelt, MD*

²*Universities Space Research Association, Columbia, MD*

³*Science Systems and Applications, Inc., Lanham, MD*

⁴*Morgan State University, Baltimore, MD*

⁵*Earth System Science Interdisciplinary Center, College Park, MD*

⁶*Science Applications International Corporation, Beltsville, MD*

[†]*Current affiliation: ExxonMobil Corporate Strategic Research, Annandale, NJ*

[‡]*Current affiliation: I.M. System Group, Inc., Rockville, MD*

Revised 23 March 2017

Accepted for publication in *Journal of Climate* on 29 March 2017
MERRA-2 Special Collection

Corresponding author: Ronald Gelaro, Global Modeling and Assimilation Office, NASA
Goddard Space Flight Center, Greenbelt, MD 20771, USA. Email: ron.gelaro@nasa.gov

24 **Abstract**

25 The Modern-Era Retrospective Analysis for Research and Applications, Version 2 (MERRA-
26 2) is the latest atmospheric reanalysis of the modern satellite era produced by NASA's
27 Global Modeling and Assimilation Office (GMAO). MERRA-2 assimilates observation
28 types not available to its predecessor, MERRA, and includes updates to the Goddard
29 Earth Observing System (GEOS) model and analysis scheme so as to provide a viable
30 ongoing climate analysis beyond MERRA's terminus. While addressing known limita-
31 tions of MERRA, MERRA-2 is also intended to be a development milestone for a future
32 integrated Earth system analysis (IESA) currently under development at GMAO. This
33 paper provides an overview of the MERRA-2 system and various performance metrics.
34 Among the advances in MERRA-2 relevant to IESA are the assimilation of aerosol
35 observations, several improvements to the representation of the stratosphere including
36 ozone, and improved representations of cryospheric processes. Other improvements in
37 the quality of MERRA-2 compared with MERRA include the reduction of some spuri-
38 ous trends and jumps related to changes in the observing system, and reduced biases
39 and imbalances in aspects of the water cycle. Remaining deficiencies are also identified.
40 Production of MERRA-2 began in June 2014 in four processing streams, and converged
41 to a single near-real time stream in mid 2015. MERRA-2 products are accessible online
42 through the NASA Goddard Earth Sciences Data Information Services Center (GES
43 DISC).

44 1. Introduction

45 Reanalysis is the process whereby an unchanging data assimilation system is used to
46 provide a consistent reprocessing of meteorological observations, typically spanning an
47 extended segment of the historical data record. The process relies on an underlying
48 forecast model to combine disparate observations in a physically consistent manner, en-
49 abling production of gridded data sets for a broad range of variables including ones that
50 are sparsely or not directly observed. As such, and with appropriate consideration of the
51 inherent uncertainties, reanalysis products have not only become a staple of the atmo-
52 spheric research community, but are used increasingly for climate monitoring as well as
53 for business applications in, for example, energy and agriculture. Recent reanalyses from
54 the National Oceanic and Atmospheric Administration/National Centers for Environ-
55 mental Prediction (NOAA/NCEP), the European Centre for Medium-Range Weather
56 Forecasts (ECMWF), the National Aeronautics and Space Administration/Global Mod-
57 eling and Assimilation Office (NASA/GMAO), and the Japan Meteorological Agency
58 (JMA) provide a rich ensemble of climate data products beginning more or less with
59 the period of regular conventional and satellite observations in the mid to late twentieth
60 century (Saha et al. 2010; Dee et al. 2011; Rienecker et al. 2011; Kobayashi et al. 2015).
61 However, there have also been successful efforts to extend atmospheric reanalyses back
62 to the late nineteenth and early twentieth centuries using only surface pressure obser-
63 vations (Compo et al. 2011) or surface and mean sea level pressure observations plus
64 surface marine winds (Poli et al. 2013). As noted by Dee et al. (2011), these century-
65 long reanalyses have also sparked remarkable data recovery and digitization efforts by
66 various groups around the world.

67 The GMAO’s reanalysis development effort began (under its predecessor organization,
68 the Data Assimilation Office) with the production of the Goddard Earth Observing

69 System, version 1 (GEOS-1) reanalysis (Schubert et al. 1993), but advanced significantly
70 with the more recent production of the Modern-Era Retrospective Analysis for Research
71 and Applications (MERRA, Rienecker et al. 2011). MERRA encompassed the period
72 1979–2016 and was undertaken with two primary objectives: to place NASA’s Earth
73 Observing System (EOS) satellite observations in a climate context and to improve
74 the representation of the atmospheric branch of the hydrological cycle compared with
75 previous reanalyses. MERRA succeeded in meeting these objectives overall and was
76 found to be of comparable quality to contemporaneous reanalyses produced by NCEP
77 and ECMWF (e.g., Decker et al. 2011). However, it also suffered from a number
78 of known, but not necessarily unique, deficiencies. These include unphysical jumps
79 and trends in precipitation in response to changes in the observing system, biases and
80 imbalances in certain atmospheric and land surface hydrological quantities, and a poor
81 representation of the upper stratosphere (e.g., Bosilovich et al. 2011; Robertson et al.
82 2011; Reichle et al. 2011; Rienecker et al. 2011). In addition, the long-term viability
83 of MERRA was limited by system constraints that precluded the incorporation of new
84 satellite data sources beyond NOAA-18, which launched in 2005. At the time of its
85 termination in March 2016, MERRA was at risk of suffering a significant degradation
86 in quality were certain observing platforms to fail, including, for example, EOS Aqua,
87 which was already well beyond its designed lifetime and provided MERRA with its only
88 sources of hyperspectral infrared and afternoon-orbit microwave radiances.

89 The Modern Era Retrospective Analysis for Research and Applications, version 2 (MERRA-
90 2) was undertaken to provide a timely replacement for MERRA and to sustain GMAO’s
91 commitment to having an ongoing near-real-time climate analysis. MERRA-2 is in-
92 tended as an intermediate reanalysis; one that leverages recent developments at GMAO
93 in modeling and data assimilation to address some of the known limitations of MERRA,
94 but also provides a stepping stone to GMAO’s longer term goal of developing an in-

95 tegrated Earth system analysis (IESA) capability that couples assimilation systems for
96 the atmosphere, ocean, land and chemistry. Toward the latter goal MERRA-2 includes
97 aerosol data assimilation, thereby providing a multi-decadal reanalysis in which aerosol
98 and meteorological observations are jointly assimilated within a global data assimilation
99 system. Other new developments in MERRA-2 relevant to IESA focus on aspects of
100 the cryosphere and stratosphere, including the representation of ozone, and on the use
101 of precipitation observations to force the land surface. At the same time, basic aspects
102 of the MERRA-2 system, such as the variational analysis algorithm and observation
103 handling, are largely unchanged since MERRA. Also unchanged is the preparation of
104 most conventional data sources used originally in MERRA.

105 This paper presents an overview of MERRA-2, including a description of the data as-
106 simulation system and various measures of performance. Some of these measures focus
107 on difficulties encountered in MERRA while others highlight new capabilities such as
108 the assimilation of aerosol observations. This paper also serves as an introduction to a
109 series of companion papers that provide more detailed analyses of the topics covered in
110 this overview as well as others. For example, a detailed description of the MERRA-2
111 aerosol analysis system and its validation are presented in Randles et al. (2017) and
112 Buchard et al. (2017). Reichle et al. (2017a,b) assess the land surface precipitation
113 and land surface hydrology, while Draper et al. (2017) examine the land surface en-
114 ergy budget. Bosilovich et al. (2017) evaluate the global water balance and water cycle
115 variability in MERRA-2. Collow et al. (2016) examine MERRA-2's representation of
116 US summertime extreme precipitation events, and Lim et al. (2017) investigate aspects
117 of major El Niño events. Collow and Miller (2016) examine the radiation budget and
118 cloud radiative effect over the Amazon. Segal-Rosenhemier et al. (2017) examine surface
119 radiative fluxes in polar marginal ice zones. Several papers investigate aspects of the
120 stratosphere in MERRA-2: Wargan et al. (2017) examine the representation of lower

121 stratospheric ozone and the effect of assimilating ozone observations from NASA’s Aura
122 satellite; Coy et al. (2016) examine the representation of the quasi-biennial oscillation
123 in MERRA-2; and Wargan and Coy (2016) present a case study of the 2009 sudden
124 stratospheric warming.

125 Section 2 provides an overview of the MERRA-2 data assimilation system, focusing pri-
126 marily on developments since MERRA, including new observation sources. Basic met-
127 rics of the assimilation system performance are presented in section 3. The MERRA-2
128 aerosol analysis is described in section 4, along with sample results and validation statis-
129 tics. Section 5 examines global and regional aspects of the representation of precipitation
130 in MERRA-2, focusing on areas of difficulty in MERRA. Stratospheric processes and
131 the representation of ozone are discussed in section 6. Section 7 addresses the represen-
132 tation of the cryosphere in MERRA-2, with focus on glaciated land surface processes.
133 Section 8 provides information about MERRA-2 products and how they can be accessed.
134 It is noted here that each MERRA-2 data collection has its own digital object identifier
135 (DOI) number, so data used in scientific publications can be cited exactly. Most of the
136 results shown for MERRA-2 in this paper are derived from these collections, which are
137 individually cited in the corresponding figure captions. Finally, a brief summary and
138 perspective on future work are presented in section 9. A list of acronyms is given in the
139 Appendix.

140 **2. MERRA-2 system description**

141 MERRA-2 is produced with version 5.12.4 of the Goddard Earth Observing System
142 (GEOS-5.12.4) atmospheric data assimilation system. The key components of the system
143 are the GEOS atmospheric model (Rienecker et al. 2008; Molod et al. 2015) and the
144 Gridpoint Statistical Interpolation (GSI) analysis scheme (Wu et al. 2002; Kleist et

al. 2009b). The model includes the finite-volume dynamical core of Putman and Lin (2007), which uses a cubed sphere horizontal discretization at an approximate resolution of $0.5^\circ \times 0.625^\circ$ and 72 hybrid-eta levels from the surface to 0.01 hPa. The analysis is computed on a latitude-longitude grid at the same spatial resolution as the atmospheric model using a three-dimensional variational (3DVAR) algorithm based on the GSI with a 6-h update cycle and the so-called first-guess-at-appropriate-time (FGAT) procedure for computing temporally accurate observation-minus-background departures. The analysis is applied as a correction to the background state using an incremental analysis update (IAU) procedure (Bloom et al. 1996).

The MERRA-2 system has many of the same basic features as the MERRA system (GEOS-5.2.0) described in Rienecker et al. (2011) but includes a number of important updates. An overview of these updates is provided here, with additional details provided in companion publications as cited. Unless otherwise stated, other aspects of the system configuration and preparation of the input data are as described in Rienecker et al. (2011). The updates discussed here include changes to the forecast model (section 2a), the analysis algorithm (section 2b), the observing system (section 2c), the radiance assimilation (section 2d), the bias correction of aircraft observations (section 2e), the mass conservation and water balance (section 2f), the precipitation used to force the land surface and drive wet aerosol deposition (section 2g), the boundary conditions for sea surface temperature and sea ice concentration (section 2h), and reanalysis production (section 2i).

a. Forecast model

Since MERRA, the GEOS model has undergone changes to both its dynamical core and its physical parameterizations. Whereas in MERRA the horizontal discretization of

169 the model was computed on a latitude-longitude grid, MERRA-2 uses a cubed sphere
 170 grid. This allows relatively uniform grid spacing at all latitudes and mitigates the more
 171 severe grid spacing singularities that occur on a latitude-longitude grid. Upgrades to
 172 the physical parameterization schemes include increased re-evaporation of frozen pre-
 173 cipitation and cloud condensate, changes to the background gravity wave drag, and
 174 an improved relationship between the ocean surface roughness and ocean surface stress
 175 (Molod et al. 2015). The MERRA-2 model also includes a Tokioka-type trigger on deep
 176 convection as part of the Relaxed Arakawa-Schubert (RAS, Moorthi and Suárez 1992)
 177 convective parameterization scheme, which governs the lower limit on the allowable en-
 178 trainment plumes (Bacmeister and Stephens 2011). A new glaciated land representation
 179 and seasonally-varying sea ice albedo have been implemented, leading to improved air
 180 temperatures and reduced biases in the net energy flux over these surfaces (Cullather et
 181 al. 2014).

182 *b. Analysis algorithm*

183 The control variable for moisture used in recent versions of GSI and MERRA-2 differs
 184 from the one used in MERRA. Whereas MERRA used the so-called pseudo-relative
 185 humidity (Dee and da Silva, 2003) defined by the water vapor mixing ratio scaled by
 186 its saturation value, MERRA-2 uses the normalized pseudo-relative humidity (Holm
 187 2003) defined by the pseudo-relative humidity scaled by its background error standard
 188 deviation. The latter has a near Gaussian error distribution, making it more suitable for
 189 the minimization procedure employed in the assimilation scheme. Also within the GSI,
 190 a tangent linear normal mode constraint (TLNMC, Kleist et al. 2009a) is applied during
 191 the minimization procedure to control noise and improve the overall use of observations.
 192 The background error statistics used in the GSI have been updated as well in MERRA-

2. As in MERRA, the statistics are estimated using the ‘NMC’ method (Parrish and Derber, 1992) by calculating variances and covariances from the differences between 24-h and 48-h forecasts, but from a more recent version of GEOS. Compared with the MERRA system, the background error statistics for the MERRA-2 system exhibit generally smaller standard deviations for most variables, but both larger and smaller correlation length scales depending on the variable, latitude and vertical level.

c. Observing system

MERRA included no new satellite observation sources after the introduction of NOAA-18 in 2005. MERRA-2, in contrast, includes numerous additional satellite observations both before and after this time. The complete set of input observations assimilated in MERRA-2 is summarized in Table 1, while a detailed description of their use is provided in McCarty et al. (2016). Additions to the MERRA-2 observing system compared with MERRA include:

- Atmospheric motion vectors from the Advanced Very High Resolution Radiometer (AVHRR);
- Surface wind speeds from the Special Sensor Microwave Imager/Sounder (SSMIS);
- Surface wind vectors from the Meteorological Operational Satellite-A (Metop-A) Advanced Scatterometer (ASCAT) and WindSat;
- Temperature and ozone profiles from the EOS Aura Microwave Limb Sounder (MLS);
- Total column ozone from the EOS Aura Ozone Monitoring Instrument (OMI);
- Bending angle from Global Positioning System radio occultations (GPSRO);

- 215 • Microwave and infrared sounding radiances from the Advanced TIROS Operational
216 Vertical Sounder (ATOVS) on NOAA-19, Metop-A and -B;
- 217 • Microwave sounding radiances from the Advanced Technology Microwave Sounder
218 (ATMS) on the Suomi National Polar-orbiting Partnership (SNPP);
- 219 • Hyperspectral infrared radiances from the Infrared Atmospheric Sounding Inter-
220 ferometer (IASI) on Metop-A and -B, and from the Cross-track Infrared Sounder
221 (CrIS) on SNPP;
- 222 • Geostationary radiances from the Meteosat Second Generation (MSG) Spinning
223 Enhanced Visible Infrared Imager (SEVIRI) and Geostationary Operational En-
224 vironmental Satellites (GOES-11, -13 and -15).

225 Time series of the various types of observations assimilated in MERRA and MERRA-2
226 are shown in Figure 1. The number of assimilated observations in MERRA-2 grows
227 from approximately two million per 6-h cycle in 2002 to almost five million in 2015,
228 while MERRA assimilates approximately 1.5 million observations per 6-h cycle from
229 2002 onward. The GSI in MERRA-2 is also capable of assimilating microwave and hy-
230 perspectral infrared radiances from planned future satellites including Metop-C and the
231 Joint Polar Satellite System (JPSS). The temporary spike in the number of QuikSCAT
232 data assimilated in MERRA-2 in late 2000 is due to an error in preprocessing which
233 led to observations beyond the mid-swath “sweet spot” being used in the analysis. This
234 has no discernible impact on the quality of the analyzed fields or on the use of other
235 observations in the assimilation system.

236 MERRA-2 also assimilates reprocessed versions of some of the same satellite observation
237 types used in MERRA. In MERRA-2, Remote Sensing Systems version 7 (RSS v7)
238 recalibrated radiances and retrieved surface wind speeds from the Defense Meteorological

239 Satellite Program (DMSP) Special Sensor Microwave Imager (SSM/I) are used, whereas
 240 MERRA used RSS v6. The use of retrieved ozone from the Solar Backscatter Ultraviolet
 241 Radiometer (SBUV) also differs, with MERRA-2 assimilating version 8.6 on 21 layers
 242 from 1980 thru 2004 before switching to OMI and MLS in October 2004. In contrast,
 243 MERRA used SBUV version 8 throughout, in a form degraded from its original 21 layers
 244 to 12.

245 *d. Radiance assimilation*

246 Radiative transfer calculations necessary for the assimilation of satellite radiances in
 247 MERRA-2 are performed using the Community Radiative Transfer Model (CRTM, Han
 248 et al. 2006, Chen et al. 2008). MERRA-2 uses version 2.1.3 of the CRTM for assimilation
 249 of all satellite radiances, whereas MERRA used a prototype version of the CRTM for
 250 all radiances except those from the Stratospheric Sounding Unit (SSU), for which the
 251 Goddard Laboratory for Atmospheres TOVS forward model (GLATOVs, Susskind et
 252 al. 1983) was used. Differences between the prototype and version 2.1.3 of the CRTM
 253 are too numerous to mention here, but a detailed description of the latter can be found
 254 in Liu and Boukabara (2014).

255 The actively assimilated channels for each satellite sensor type in MERRA-2 are sum-
 256 marized in Table 2. Microwave temperature sounding channels with strong surface
 257 sensitivity—so-called window channels—are not assimilated in MERRA-2, in part be-
 258 cause of the strong sensitivity of global precipitation and humidity to these data found in
 259 MERRA (Robertson et al. 2011). These include channels 1–3 and 15 on the Advanced
 260 Microwave Sounding Unit-A (AMSU-A), channels 1–4 and 16 on ATMS, and channel
 261 1 on the Microwave Sounding Unit (MSU). For microwave humidity sounders includ-
 262 ing the the Advanced Microwave Sounding Unit-B (AMSU-B) and Microwave Humid-

ity Sounder (MHS), window channels are actively assimilated along with the sounding channels. For heritage infrared sounders, channels 13–15 on the High-resolution Infrared Radiation Sounder (HIRS) were assimilated in MERRA but are excluded in MERRA-2. The channel selections for hyper-spectral infrared sounders and performance assessments for selected instruments are provided in McCarty et al. (2016).

Like MERRA, MERRA-2 uses an automated bias correction scheme for the assimilation of most satellite radiance observations. Bias estimates for individual sensor channels are represented by a small number of predictors which can depend on the atmospheric state, the radiative transfer model, and the sensor characteristics. Air-mass- and viewing angle-dependent biases are estimated using a variational scheme in which the predictor coefficients are updated as part of the control vector used to minimize the analysis cost function (Derber and Wu, 1998). Satellite scan-position-dependent bias is estimated directly as an exponential moving average filter of the observation-minus-background departures for brightness temperature. For both the variational and scan-position predictors, initial values of the coefficients for MERRA-2 were derived from GEOS operations and other long production runs using system versions similar to that used for MERRA-2. In the few cases where no recent coefficient information was available, initial values were derived from MERRA. Note that no bias correction is applied to a small number of sensor channels that peak in the upper stratosphere, including channel 14 on AMSU-A, channel 15 on ATMS, and channel 3 on SSU. This is done to prevent the variational bias correction scheme—which is formulated to remove systematic discrepancies between the observations and the background state irrespective of the source—from making erroneous adjustments to the observations at levels where model biases are known to be large.

e. Bias correction of aircraft temperature observations

288 A bias correction scheme for aircraft temperature observations has been implemented in
289 MERRA-2, motivated by the known warm bias of these measurements compared with
290 other data sources (Cardinali et al. 2003, Ballish and Kumar 2008; Rienecker et al.
291 2011). The scheme uses the mean observed-minus-background departures to estimate
292 the bias for temperature reports from individual aircraft, identified by their tail number.
293 The bias estimates are updated after each analysis. The scheme is used to correct
294 Aircraft Meteorological Data Relay (AMDAR) and Aircraft Communications Addressing
295 and Reporting (ACARS) reports only, since other sources of aircraft observations in
296 MERRA-2 do not have unique identifiers by which they can be tracked. As of 2015, bias
297 corrections for approximately 3700 separate aircraft are tracked in MERRA-2.

298 The performance of the scheme is discussed in McCarty et al (2016). As expected,
299 the scheme is shown to reduce the bias between the corrected aircraft observations
300 and the background forecast, as well as reduce the variance of the corrected background
301 departures, allowing more aircraft observations to be used in the analysis. Unfortunately,
302 the MERRA-2 background state was found to have a larger than expected positive bias
303 in the mid- to upper troposphere, which feeds back to the bias estimates. The result
304 is that the bias correction actually increases the aircraft temperatures in some cases,
305 and the fit to other unbiased observation types such as radiosondes is degraded. This is
306 discussed further in section 3.

307 *f. Mass conservation and water balance*

308 Studies have documented the difficulty of maintaining realistic balances between varia-
309 tions in total mass and total water content in previous reanalyses (e.g., Trenberth and

Smith 2005; Bosilovich et al. 2011; Berrisford et al. 2011). These studies show that analysis adjustments to moisture are often large (when, ideally, they should be small), highly sensitive to changes in the observing system, and mostly balanced by unphysical changes in precipitation. Takacs et al. (2016) argue that, in attempting to analyze the total mass of the atmosphere from surface pressure observations, reanalyses may violate the simple physical constraint that, to an excellent approximation, the total dry mass of the atmosphere is invariant, and so changes in total mass must be essentially equivalent to changes in total water mass. At the same time, Berrisford et al. (2011) argue that, while the observing system may not provide the data to determine exactly the total mass of the atmosphere, the degree to which dry mass is preserved in a reanalysis provides a useful diagnostic of reanalysis quality.

Reconsideration of these issues during the development of MERRA-2 prompted modifications to GEOS to conserve atmospheric dry mass and to guarantee that the net source of water from precipitation and surface evaporation equals the change in total atmospheric water. As described by Takacs et al. (2016), this has been achieved by making the following changes to the forecast model and assimilation procedure:

- Sources and sinks of atmospheric water have been added to the model continuity equation so that changes in total mass are driven purely by changes in total water.
- A constraint that penalizes analysis increments of dry air has been added to the GSI.
- Tendencies in the IAU are rescaled so that the global mean is removed from the analysis increment of water.

The global impact of these modifications is illustrated in Figures 2 and 3, which compare

different components of atmospheric mass in MERRA and MERRA-2. Figure 2 shows monthly mean anomalies from the mean seasonal cycle for total mass, total water, and dry-air mass in the two reanalyses. In MERRA, there is an increase in total water over the period, with significant inter-annual variations, but these features do not necessarily match the changes in total mass. There also are spurious anomalies in dry-air mass throughout, some of which track closely with the changes in total mass. In MERRA-2, changes in total mass and total water track each other almost perfectly, by design, and the dry-air mass remains a constant whose value must be specified. For the latter, the value 983.24 hPa is chosen based on MERRA. This value falls within 0.1% of the values derived from other recent reanalyses (Takacs et al. 2016).

Figure 3 shows monthly mean values of evaporation minus precipitation ($E - P$, or water source term), the vertically integrated analysis increment of water, and the atmospheric water storage. Note that the atmospheric water storage has similar magnitude in both reanalyses and is dominated by the seasonal cycle. In MERRA, however, the storage is determined by a near balance between the large and highly variable contributions from the analysis increment on the one hand, and unphysical variations in $E - P$ of the opposite sign on the other hand. This includes an abrupt change in the sign of these quantities after the introduction of AMSU-A in 1998 (Robertson et al. 2011). In MERRA-2, the globally integrated analysis increment is zero, by design, and the water storage is determined as in nature by small seasonal differences in E and P . It should be noted that removing the global mean analysis increments of total mass and water mass does not imply that the analysis increments of water vapor or surface pressure vanish locally, as shown in Section 3 of this paper and discussed in further detail by Bosilovich et al. (2017).

g. Observation-corrected precipitation forcing

358 The precipitation generated by the atmospheric model during the IAU segment of the
359 assimilation procedure is subject to considerable errors that can propagate into land
360 surface hydrological fields and beyond (Reichle et al. 2011). To mitigate these effects
361 in MERRA-2, the model-generated precipitation is corrected with observations before
362 being used to force the land surface or affect the wet deposition of aerosols over land
363 and ocean. Both the model-generated precipitation and the precipitation seen by the
364 land surface and the aerosols are available in the MERRA-2 output. MERRA-2 is
365 one of several recent applications of GEOS that uses observation-corrected precipitation
366 estimates. Others include the GMAO seasonal forecasting system (Ham et al. 2014), the
367 MERRA-Land data product (Reichle et al. 2011), and the MERRAero aerosol reanalysis
368 (Buchard et al. 2015). Precipitation observations have also been used in reanalyses
369 produced by NOAA, including the North American Regional Reanalysis (Mesinger et al.
370 2006) and in the Climate Forecast System Reanalysis (CFSR, Saha et al. 2010; Meng
371 et al. 2012), although in both cases the approaches differ from that used in MERRA-2.
372 Some discussion of the differences between the approaches used in MERRA-2 and CFSR
373 can be found in Reichle et al. (2017a).

374 The corrected precipitation in MERRA-2 is derived from publicly available, observa-
375 tionally based global precipitation products disaggregated from daily or pentad totals
376 to hourly accumulations using precipitation estimates from MERRA (Reichle and Liu
377 2014; Reichle et al. 2017a). The land surface in MERRA-2 sees a combination of cor-
378 rected and model-generated precipitation depending on latitude, with the land surface
379 forced primarily by the corrected estimates at low to mid-latitudes, by the MERRA-2
380 model-generated precipitation at high latitudes, and by a weighted mixture in between
381 to prevent spatial discontinuities in climatological means. This is illustrated in Figure 4,

382 which shows the annual average adjustment made to the model-generated precipitation
383 in MERRA-2 for the period 1980–2015 using this technique. The greatest adjustments
384 are made in the tropics, where precipitation is greatest and the corrected estimates are
385 given most weight, while no adjustments are made poleward of 62.5° in either hemi-
386 sphere.

387 Based on the evaluation of several metrics, Reichle et al. (2017a) found the observation-
388 corrected precipitation to be more realistic overall than that generated by the model
389 within the cycling MERRA-2 system, or that of the MERRA and MERRA-Land data
390 products. Exceptions include discontinuities in the MERRA-2 corrected precipitation
391 that result from errors in the underlying gauge products, for example, in Myanmar and
392 South America. Another issue is the high bias in MERRA-2 summer precipitation in the
393 high latitudes (where precipitation observations are not used). Moreover, the diurnal
394 cycle of the MERRA-2 corrected precipitation has reasonable amplitudes compared to
395 independent observations, but the time-of-day of maximum precipitation is inherited
396 from MERRA and is unrealistic.

397 The improvements in the precipitation forcing are also reflected in the MERRA-2 land
398 surface estimates. Reichle et al. (2017b) show that soil moisture, snow, terrestrial
399 water storage, and runoff in MERRA-2 agree better with independent observations than
400 estimates from MERRA. Draper et al. (2017) further demonstrate that the temporal
401 behavior and long term mean values of the land-atmosphere turbulent fluxes in MERRA-
402 2 are improved. Moreover, by applying the precipitation corrections within the coupled
403 atmosphere-land modeling system, MERRA-2 can provide more self-consistent surface
404 meteorological data than were used for MERRA-Land (Reichle et al. 2017a). This self-
405 consistency is important for applications such as forcing land-only model simulations.

406 Finally, it should be noted that the atmospheric water and energy prognostic variables
407 associated with the creation of precipitation in MERRA-2 are not directly modified by
408 the corrected estimates, although they can be indirectly modified through subsequent
409 feedback with the land surface.

410 *h. Sea surface temperature and sea ice concentration*

411 The boundary conditions for sea surface temperature (SST) and sea ice concentration
412 (SIC) in MERRA were based on the 1° weekly (or monthly) product of Reynolds et al.
413 (2002). In MERRA-2, SST and SIC boundary conditions are instead based on currently
414 available high-resolution (finer than 1°) daily products. However, as there exists no
415 continuous source of daily global high-resolution SST and SIC for the entire period
416 of MERRA-2—and no source of daily data whatsoever prior to 1982—the following
417 products were used in combination (Table 3): monthly 1° data from the Coupled Model
418 Intercomparison Project (CMIP) as in Taylor et al. (2000) for the period prior to
419 1982; daily $1/4^\circ$ data from the NOAA Optimum Interpolation Sea Surface Temperature
420 (OISST) as in Reynolds et al. (2007) from 1982 thru March 2006; and daily $1/20^\circ$
421 data from the Operational Sea Surface Temperature and Sea Ice Analysis (OSTIA) as
422 in Donlon et al. (2012) from April 2006 onwards. Note that different versions of the
423 NOAA OISST product are used prior to and after January 2003, the latter including
424 satellite data from both AVHRR and the Advanced Microwave Scanning Radiometer-
425 EOS (AMSR-E) on NASA’s Aqua satellite, and the former including satellite data from
426 AVHRR only. The processing of these products into a unified gridded set of daily SST
427 and SIC boundary conditions for MERRA-2 is described in Bosilovich et al. (2015).
428 Care was taken to use both SST and SIC from the same data source to avoid potential
429 inconsistencies, especially in marginal ice zones.

Figure 5 shows 12-month running averaged values of SST between 60°N and 60°S for MERRA-2 and several other reanalyses, including MERRA. In all cases, there is a positive trend in SST throughout the period. The running means for all the reanalyses are within 1 K for the 30 years spanning 1980–2010, and the anomalies (not shown) are separated by less than 0.2 K. At the same time, there are clear systematic differences between reanalyses, with the MERRA-2 SST’s on the one hand being cooler than those used in the other reanalyses shown except CFSR (which used similar input data sets), especially before the transition to OSTIA in 2006. The values for JRA-55, on the other hand, are on the order of 0.1 K higher than other reanalyses throughout the 35-year period. It can also be seen that the MERRA-2 SSTs increase slightly with the change in NOAA OISST versions after 2003. The reader is referred to Bosilovich et al. (2015) for a more detailed list of known issues with the SST and SIC boundary conditions for MERRA-2.

i. Production

MERRA-2 was produced in four separate streams, each of which was spun up for a year at full resolution beginning on 1 January 1979 (stream 1), 1 January 1991 (stream 2), 1 January 2000 (stream 3) and 1 January 2010 (stream 4). The land surface restart files for each MERRA-2 stream were themselves spun up for at least 20 years using the off-line MERRA-2 land model forced by MERRA surface meteorological fields, and with the precipitation replaced by the observation-corrected estimates described in section 2g. The final MERRA-2 product distribution is from stream 1 for 1 January 1980–31 December 1991, followed by stream 2 for 1 January 1992–31 December 2000, then stream 3 for 1 January 2001–31 December 2010, and finally stream 4 for 1 January 2011–present. With streams 1–3 complete, MERRA-2 production continues as a near-real time climate

analysis from stream 4 alone. The decision to begin stream 1 in January 1979 and distribute products beginning in January 1980—a year later than the schedule followed in MERRA—was based on the fact that the products used to create the observation-corrected precipitation estimates for MERRA-2 only start on 1 January 1979, leaving no viable way to initialize the land surface properly before this time (which requires several months of spin-up, after initialization from climatological conditions).

The overlap periods between successive streams were examined to determine the adequacy of the spin-up procedure and to quantify the uncertainty in individual fields. Differences between overlapping MERRA-2 streams were found to be minimal for most fields after one year, with the exception of certain land surface variables including the deep-level soil temperature and land surface soil moisture storage at high latitudes. The spin-up of the land surface is addressed separately in Reichle et al. (2017a); section 3d and Figure 13 of that paper discuss specific examples of the aforementioned discontinuities across consecutive MERRA-2 streams. Users should be aware of these discontinuities when the data are used for specific applications.

3. Data assimilation diagnostics

By-products of the data assimilation procedure in the form of differences between forecasts and observations, analysis increments, and estimates of bias can be used effectively to monitor the quality of both the input and output of the assimilation. In this section, examples of such diagnostics are presented for MERRA-2, focused mainly on feedbacks with respect to in-situ conventional observations and on the net correction, or increment, brought by the entirety of the assimilated observations. The reader is referred to McCarty et al. (2016) for examples of feedbacks related to the treatment of satellite radiance observations.

478 *a. Background departure statistics*

479 Differences between the assimilated observations and the background forecast, referred
480 to as innovations or background departures, provide important information about the
481 quality of the assimilation. In particular, it is important that the assimilation system be
482 able to predict high-quality observations, especially for conventional data types which
483 provide direct measurements of the analyzed variables. In addition to affecting the anal-
484 ysis directly, many conventional data play an important role in anchoring the variational
485 bias estimates used in the assimilation of satellite radiances. Generally speaking, smaller
486 background departures indicate a higher quality assimilation. The results shown here
487 are selected to highlight both strengths and weaknesses of MERRA-2 in this regard.
488 As in MERRA, for convenience, gridded versions of the observations and corresponding
489 departures used in MERRA-2 will be made available to users.

490 Figure 6 shows time series of monthly mean and root mean square (RMS) background
491 departure statistics for all assimilated surface pressure observations in MERRA and
492 MERRA-2 for both the Northern and Southern Hemisphere. Also shown are the monthly
493 mean numbers of surface pressure observations assimilated in each 6-h assimilation cycle
494 in MERRA-2. The RMS values decrease with time in both reanalyses, especially in the
495 Southern Hemisphere after the early to mid 1990's when the number of observations
496 begins to increase significantly. The RMS values in the Northern Hemisphere (Fig-
497 ure 6a) are smaller than in the Southern Hemisphere initially and decrease more slowly
498 with time, reflecting the greater number of conventional observations available over land
499 throughout the period. This decrease is slightly more pronounced in MERRA-2 after
500 the mid 1990's when the number of surfaces pressure observations from land stations
501 increases significantly. In the Southern Hemisphere (Figure 6b), the RMS values are
502 larger in MERRA-2 than in MERRA before the mid 1990's but smaller by the end of

the period. The larger values early on are due to the use of larger observation errors for surface ship observations (and some other conventional data types) in MERRA-2, allowing more “outliers” with larger departure values to pass the quality control procedure in the analysis.¹ The impact diminishes by the mid 1990’s as other observation types, including from satellites, become more abundant. There is no similar effect in the Northern Hemisphere where surface pressure observations from land stations are dominant early in the period; the observation errors specified for these data are the same in MERRA and MERRA-2. Finally, the jump in RMS values in the Southern Hemisphere evident in both reanalyses at the beginning of 1985 coincides with the introduction of regularly spaced synthetic surface pressure observations over southern ocean areas.

The mean background departures for surface pressure in the Northern Hemisphere are consistently less biased in MERRA-2 than in MERRA, especially after the mid 1990’s. In the Southern Hemisphere, however, the departures for MERRA-2 show a negative bias throughout the period; this is discussed further in section 3b. The mean departures in MERRA-2 also show a more pronounced annual cycle in this hemisphere. As a point of reference, the background departure statistics for other reanalyses including, for example, ERA-Interim (Dee et al. 2011) exhibit a clear annual cycle, but with somewhat smaller amplitude than in MERRA-2.

Figure 7 shows global background departure statistics for radiosonde temperatures for MERRA and MERRA-2 at selected pressure levels in the troposphere (300 hPa and 700 hPa) and stratosphere (10 hPa and 50 hPa). Also shown for each level are the monthly mean numbers of radiosonde temperature observations assimilated in each 6-h assimilation cycle in MERRA-2. In the troposphere (Figures 7c and d), the performance of MERRA-2 is degraded compared to that of MERRA, especially at 300 hPa. The

¹The observation errors for conventional data types have been adjusted since MERRA-2.

527 RMS values for MERRA-2 decrease with time but remain 10–20% larger than those for
528 MERRA during much of the period. Again, this is due at least partially to the use of
529 larger observation errors for radiosonde temperatures and other conventional data types
530 in MERRA-2. Noticeable improvements occur first in the mid 1990’s when satellite
531 observations become more abundant, and again in 2006 when the number of GPSRO
532 observations increases significantly.

533 The mean departure values at 300 hPa for both MERRA and MERRA-2 exhibit a clear
534 negative bias. The bias is generally larger in MERRA-2, reaching a maximum amplitude
535 of greater than 0.5 K during the early 2000’s. This is due to a warm model bias in the
536 upper troposphere which worsened during the course of development between MERRA
537 and MERRA-2 (see also Figure 10). However, aspects of the assimilation process may
538 exacerbate the problem. It can be seen for example that the bias in the background
539 departures at 300 hPa increases noticeably after the mid 1990’s, especially in MERRA-2,
540 when the numbers of both aircraft temperature observations and satellite radiances begin
541 to increase significantly (Figure 1). The design of the bias correction procedures for both
542 observation types is such that they result in an adjustment of the observations regardless
543 of the source of the bias. In the presence of a strong model bias this can reinforce the
544 actual observational bias and cause the assimilation system to drift further toward the
545 model state, as noted in the case of the aircraft bias corrections described in section 2e.
546 A similar, though less direct, effect may occur through the observational bias corrections
547 used to assimilate satellite radiances, although other aspects of the variational scheme
548 used to adjust these data act to reduce this risk (Dee and Uppala 2009). At 700 hPa, the
549 mean departures for both reanalyses are generally more comparable and considerably
550 less biased.

551 In the stratosphere (Figures 7a and b), there are fewer significant differences between

the results for MERRA and MERRA-2 although the departures at 10 hPa for MERRA-2 show a larger negative bias of -0.2 K to -0.3 K prior to the early 2000's. After 2002, when assimilation of AIRS radiances begins, the biases at 10 hPa in both reanalyses exhibit an upward trend and eventually become positive, first in MERRA around 2003 and then in MERRA-2 in 2005. There is a discernible jump in the mean departures at this level for MERRA-2 in 2005. This is around the time when assimilation of both MLS temperature retrievals (above 5 hPa) and GPSRO bending angle observations (up to approximately 10 hPa) begins in MERRA-2, but this does not appear to improve the fit to radiosondes at 10 hPa compared with MERRA. After 2006, the biases in both reanalyses have average values of 0.2 K to 0.3 K. Finally, at 50 hPa, the departure values for both reanalyses are very similar and exhibit only a small positive bias throughout.

Figure 8 shows statistics for radiosonde specific humidity background departures at 500 and 850 hPa in the tropics. The performance of MERRA-2 is slightly worse than that of MERRA in the middle troposphere in terms of both RMS and bias, but similar or slightly better in the lower troposphere. Again, the mean departure values are consistent with known biases in the GEOS model.

b. Analysis increments

The analysis increments represent the net adjustment to the background state by the assimilation scheme in response to all the observations. As this adjustment depends in a complex way on assumed or crudely estimated errors in the observations and background state, and on the forward operator that transforms the model variables to observation space, the increments do not necessarily represent errors in the background state. Nonetheless, their spatial and temporal variations provide an important diagnostic of system performance, including how changes in the observing system may affect the con-

576 sistency of the analysis. Systematic increments often indicate the presence of biases in
577 the model or observations which may complicate the use of reanalyses for estimating
578 budgets and identifying trends (Dee et al. 2011).

579 As described in section 2, the GEOS assimilation system uses an IAU procedure which,
580 instead of correcting the initial condition, applies the analysis increment to the model
581 as a constant tendency term during the 6-h assimilation window. It is this contribution
582 to the time tendency from the analysis that is provided as a standard output quantity
583 in MERRA-2, examples of which are presented here. For convenience, these are referred
584 to as simply the analysis increments in the discussion that follows.

585 Figure 9 shows the mean and standard deviation in time of the monthly mean analysis
586 increment of surface pressure in MERRA-2 for the period January 1980 through De-
587 cember 2015. The monthly means themselves have been computed from sub-daily data,
588 eight times per day. The pattern of the mean increments indicates that the analysis
589 tends to move mass from the oceans to the continents, as noted also by Takacs et al.
590 (2016), although this pattern is arguably most robust in the Southern Hemisphere. (The
591 mostly negative surface pressure increments over Canada provide an obvious counter ex-
592 ample.) These results are consistent with those in Figure 6 showing a negative bias in
593 the Southern Hemisphere background departures in MERRA-2. The standard devia-
594 tion of the increments shows that the largest variations in surface pressure occur in the
595 middle and high latitudes, and especially over coastal Antarctica and the mountainous
596 regions of southern and eastern Asia, as well as southern Alaska.

597 Time series of the global monthly mean and standard deviation of the analysis increments
598 of temperature from the surface to 70 hPa in MERRA-2 are shown in Figure 10. The
599 most striking feature in the mean increments is the persistent cooling by the analysis

600 in the layer between 250 and 400 hPa. This is consistent with the negative bias in the
601 background departures at 300 hPa shown in Figure 7 and provides further evidence of
602 the warm model bias at these levels. Except for seasonal variations, the magnitude
603 of the cooling remains relatively constant throughout much of the period, although
604 noticeable changes occur, for example, beginning in the mid to late 1990's as the number
605 of aircraft and satellite observations increase, and again in 2006, possibly in response
606 to the introduction of data from IASI and GPSRO. Warming by the analysis is evident
607 above 200 hPa and below 700 hPa. In this global view, the mean increments close to the
608 surface exhibit a negative trend with strong warming before the early 1990's turning to
609 slight cooling after 2010, but this is in fact the net effect of distinct regional differences
610 in the increments (not shown). In particular, near-surface warming by the analysis in
611 response to a cold model bias over northern midlatitude land masses is offset by cooling
612 over southern oceans that generally increases with time beginning with the assimilation
613 of data from the first microwave humidity sensors in the late 1980's. These differences
614 also contribute to the large variability of the increments below 700 hPa (Figure 10b).
615 The variability in the mid troposphere is noticeable but small compared with that at
616 low levels, again highlighting the consistency of the cooling by the observations between
617 250 and 400 hPa.

618 The increments of specific humidity in the tropics are shown in Figure 11 for levels
619 between the surface and 250 hPa (the values become exceedingly small above this level).
620 The mean increments indicate distinct biases in the middle and lower troposphere, with
621 systematic drying between 600 and 300 hPa, and mostly moistening below 700 hPa. The
622 corrections are generally larger during the second half of the period and especially after
623 the late 1990's as more satellite observations of humidity become available. There is an
624 abrupt increase in the variability of the increments corresponding to the introduction of
625 the first SSM/I instrument in mid 1987, with additional increases corresponding to the

626 use of a second and third SSM/I instrument in late 1990 and mid-1995, respectively. The
627 use of multiple SSM/I instruments from the early 1990's to late 2000's also corresponds
628 to a strong drying and a marked increase in variability at levels very close to the surface.
629 The introduction of AMSU-B data in 1998 corresponds to marked increases in the mean
630 and variability of the increments, the latter being most pronounced in the layer between
631 800 and 900 hPa. The sensitivity of the precipitation to these observing system changes
632 is discussed in section 5.

633 **4. Aerosol data assimilation**

634 In addition to a standard meteorological analysis, MERRA-2 includes an aerosol analysis
635 as described in Randles et al. (2016, 2017) and Buchard et al. (2017). The multi-decadal
636 coverage and the coupling between aerosols and the circulation is a step forward com-
637 pared to previous EOS-era reanalyses such as MERRAero, the Navy Aerosol Analysis
638 and Prediction System (NAAPS) reanalysis (Lynch et al. 2016), the Monitoring At-
639 mospheric Composition and Climate (MACC) reanalysis (Inness et al. 2013), and the
640 more recent Copernicus Atmosphere Monitoring Service (CAMS) reanalysis (Flemming
641 et al. 2017). The MERRA-2 system produces 3-hourly analyses and gridded output of
642 both observable parameters and aerosol diagnostics not easily observed, especially on a
643 global scale, with potential applications ranging from air quality forecasting to studies
644 of aerosol-climate and aerosol-weather interactions (e.g., Bocquet et al. 2015).

645 An analysis splitting technique (Randles et al. 2017) is used to assimilate aerosol optical
646 depth (AOD) at 550 nm, in which a two-dimensional analysis is performed first using
647 error covariances derived from innovation data and then the horizontal increments are
648 projected vertically and across species using an ensemble method. AOD observations
649 are derived from several sources, including

- 650 • Reflectances from AVHRR (1979–2002, ocean-only, Heidinger et al. 2002);
- 651 • Reflectances from the Moderate Resolution Imaging Spectroradiometer (MODIS)
- 652 on Terra (2000–present) and Aqua (2002–present) (Remer et al. 2005; Levy et. al.
- 653 2007);
- 654 • AOD retrievals from the Multi-angle SpectroRadiometer (MISR) (2000–2014, bright,
- 655 desert regions only, Kahn et al. 2005);
- 656 • Direct AOD measurements from the ground-based Aerosol Robotics Network (AERONET)
- 657 (1999–2014, Holben et. al. 1998).

658 MODIS provides the vast majority of AOD observations assimilated in MERRA-2, es-
 659 pecially after 2002 when data from both the Terra and Aqua satellites become available.
 660 Prior to 2000, only AVHRR reflectances over ocean are used in MERRA-2. AOD for
 661 both MODIS and AVHRR are derived from cloud-cleared reflectances using a neural net
 662 procedure trained on AERONET measurements (Randles et al. 2017). By construction,
 663 these AOD retrievals are unbiased with respect to AERONET observations. AOD from
 664 MISR and AERONET observations are used without bias correction. Additional details
 665 about the aerosol observing system in MERRA-2 can be found in Randles et al. (2016,
 666 2017).

667 The Goddard Chemistry, Aerosol, Radiation and Transport model (GOCART; Chin et
 668 al. 2002; Colarco et al. 2010) is coupled with the GEOS atmospheric model to sim-
 669 ulate the life cycles of five externally-mixed aerosol species, including dust, sea salt,
 670 black carbon, organic carbon, and sulfate. The model carries three-dimensional mass
 671 mixing ratios of these five aerosol species as prognostic aerosol tracers. The AOD at
 672 550 nm is a column- and species-integrated optical quantity, which is calculated as the
 673 summed product of each species mass and its extinction coefficient based on aerosol

674 optical properties derived largely from the Optical Properties of Aerosols and Clouds
 675 (OPAC) dataset (see Randles et al. 2017 and references within.) Emissions of both dust
 676 and sea salt are wind-driven for each of five size bins, parameterized following Martio-
 677 corena and Bergametti (1995) and Gong (2003), respectively. Sulfate and carbonaceous
 678 aerosol emissions derive from both natural and anthropogenic sources as described in
 679 Randles et al. (2017). In particular, MERRA-2 includes volcanic sources (Diehl et al.,
 680 2012) and biomass burning emissions that utilize satellite observations, and are based on
 681 the Reanalysis of the Tropospheric chemical composition, version 2 (RETRO-2, Schultz
 682 et al. 2008), the Global Fire Emissions Database, version 3.1 (GFED-3.1, van der Werf et
 683 al. 2006), and the Quick Fire Emission Dataset, version 2.4r6 (QFED-2.4.r6, Darmenov
 684 and da Silva, 2015).

685 It should be noted that AOD observations can only directly constrain the total, species-
 686 integrated and vertically-integrated aerosol extinction — a quantity that can be related
 687 to column aerosol mass by assuming a set of optical properties. Non-analyzed aerosol
 688 properties such as the vertical distribution, aerosol speciation, and absorption are not
 689 fully constrained by the observations and are chiefly determined by the underlying model
 690 physics and error covariance assumptions. Despite this fact, Buchard et al. (2017)
 691 show that the MERRA-2 aerosol reanalysis has considerable skill in simulating numer-
 692 ous observable aerosol properties. Randles et al. (2017) show that the AOD fields in
 693 MERRA-2 generally have both high correlation and low bias relative to independent
 694 (non-assimilated) sun-photometer and aircraft observations.

695 As in the case of the meteorological analysis discussed in section 3, statistics of back-
 696 ground and analysis departures provide a basic metric of the quality of the aerosol as-
 697 simulation. Figure 12 shows probability distribution functions of collocated observation-
 698 minus-forecast and observation-minus-analysis departures from MERRA-2 for each sen-

699 sor in the aerosol observing system. Statistics are shown in terms of the log-transform
700 AOD analysis variable (i.e., $\ln[\text{AOD} + 0.01]$) which is approximately normally dis-
701 tributed (Randles et al., 2017). Note that AOD is a dimensionless quantity and log-
702 transformed AOD is typically in the range $(-4, 2)$. As expected, compared to the forecast
703 departures, the analysis departures show reduced bias with respect to the observations.
704 Note also that the innovation variances are much larger over land than ocean, a direct
705 consequence of the signal-to-noise limitation of aerosol retrievals over land.

706 Regional aspects of the global distribution of aerosols are illustrated in Figure 13, which
707 shows time series of analyzed AOD from MERRA-2 area-averaged over several major
708 aerosol source regions. The contribution of each aerosol species to the total AOD is
709 indicated by the colored shading. The seasonal cycles of dust and biomass burning
710 (carbonaceous) AOD are apparent in all regions. Large increases in sulfate aerosol occur
711 in all regions after the El Chichon (1982) and Pinatubo (1991) volcanic eruptions. Over
712 the Asian region (Figure 13a), the analysis captures high carbonaceous aerosol associated
713 with the 2003 Siberian fires and the increasing trend in AOD between the late 1990s
714 and present (commensurate with increasing anthropogenic aerosol emissions reported by
715 Diehl et al. 2012). The AOD over northern Africa (Figure 13b) is dominated by dust,
716 and major dust transport events such as in 2010 are captured (see Buchard et al. 2017
717 for details). Carbonaceous aerosol from biomass burning in major source regions such
718 as the Amazon Basin are also well captured (Figure 13c), especially after 2000 when
719 emissions inventories derive from MODIS observations (Darmenov and da Silva, 2015).

720 Figure 14 compares values of AOD from several recent aerosol reanalyses for the pe-
721 riod 2003–2010. Where such information is available, the results are partitioned by
722 species and identified as either fine or coarse mode (see caption for details). Also shown
723 are multi-model average results from Phase I of the Aerosol Comparison (AeroCom)

inter-comparison project (Kinne et al. 2006), as well as both model and observational estimates from Yu et al. (2006). The latter study includes an attempt to account for satellite clear-sky biases by combining MODIS and MISR observations with the GO-CART model. Compared to MERRAero, for example, MERRA-2 has slightly higher global average AOD due to increased contributions from dust (related to the assimilation of MISR AOD over bright surfaces) and sea salt (related to changes in model physics). MERRA-2 and NAAPS show similar global average AOD, both for fine and coarse mode aerosol. Models without assimilation (AeroCom and Yu_Model) underestimate global average AOD compared to both observational estimates (Yu_Obs) and the aerosol reanalyses. The MACC aerosol reanalysis has the highest global mean AOD (Bellouin et al. 2013), which is close to the MODIS-only value of 0.188 for the period 2003–2010 (Yu et al. 2006). MACC also has more dust and sea salt aerosol compared to the other reanalyses, particularly over the ocean (not shown).

The direct aerosol impact on the radiative energy balance of Earth is dependent on the vertical distribution of aerosol scattering and absorption, which is not fully constrained by the vertically integrated AOD measurements that MERRA-2 assimilates. An assessment of the aerosol vertical structure and absorption is presented in a companion paper (Bucharth et al. 2017). Long-term aerosol reanalyses can potentially reduce uncertainty in how aerosol direct effects have changed over time, particularly once better observational constraints on aerosol absorption become available. The direct radiative effect (DRE) of all aerosols is defined as the flux difference in W m^{-2} between clear-sky and clear clean-sky conditions (no aerosols or clouds). In the absence of clouds, this quantity is less sensitive to the vertical distribution of aerosol absorption, although it remains sensitive to absorbing aerosols over surfaces with high albedo (Chýlek and Coakley, 1974).

749 Table 4 compares the DRE from MERRA-2, MERRAero, MACC, model inter-comparisons,
 750 and the observationally constrained estimate of Yu et al. (2006). Listed are the top-of-
 751 the atmosphere (TOA), surface (SFC), and atmospheric (ATM) estimates of DRE for the
 752 period 2003–2010, averaged over land and ocean separately. Note that the atmospheric
 753 contribution to the DRE is defined as the difference between top-of-the-atmosphere
 754 and surface values, $ATM = TOA - SFC$. Over land, the DRE estimate from MACC
 755 best agrees with the observationally-constrained estimate. TOA and SFC forcing in
 756 MERRA-2 and MERRAero are lower than in MACC due to their lower AOD, although
 757 the atmospheric forcing is similar. Over ocean, the DRE estimates from MERRA-2 and
 758 MACC are lower and higher, respectively, than the observational estimate, and both re-
 759 analyses have lower estimates of atmospheric absorption. Much of the uncertainty in the
 760 DRE reported by the Intergovernmental Panel on Climate Change (IPCC) arises from
 761 differences between estimates from global models and satellite-based estimates (Myhre
 762 2009). However, as aerosol reanalyses such as MERRA-2 continue to mature and incor-
 763 porate additional observations (e.g., from lidars and multi-spectral sensors), we expect
 764 a narrowing of the gap between simulated and satellite-based estimates of the DRE.

765 **5. Precipitation**

766 The representation of precipitation in a reanalysis is key to applications in weather
 767 and climate as it ties together aspects of both the water and energy cycles. It also
 768 presents a significant challenge, however, as estimates of precipitation are only indi-
 769 rectly constrained by observations and are strongly dependent on model physics whose
 770 parameterizations have known errors and can be highly sensitive to even small changes
 771 in large-scale temperature and humidity fields. The observations themselves can some-
 772 times introduce additional uncertainty in these estimates as a result of heterogeneous

773 sampling, changes in instrumentation, and time-varying calibration (Bosilovich et al.
774 2017).

775 While improved representation of the hydrological cycle was a primary focus of MERRA,
776 the character of its global precipitation in particular was found to be highly sensitive to
777 the assimilated observations and thus to changes in the observing system (e.g., Robert-
778 son et al. 2011). Among the development aspects of MERRA-2 intended to address
779 this issue are modifications to GEOS to conserve atmospheric dry mass and ensure that
780 changes in global atmospheric total mass are equivalent to changes in total water (sec-
781 tion 2f), exclusion from the analysis of microwave temperature sounding channels with
782 strong surface sensitivity (section 2d) and, less directly, forcing of the land surface by
783 observation-corrected precipitation estimates (section 2g).

784 *a. Global aspects*

785 Bosilovich et al. (2015, 2017) have investigated the global water cycle variability in
786 MERRA-2 using comparisons with observational data sets and other recent reanalyses.
787 Those studies present a broad range of metrics on this topic, a small subset of which
788 are summarized here. Figure 15 shows time series of global mean precipitation for sev-
789 eral recent reanalyses and the observation-based estimates from the Global Precipitation
790 Climatology Project (GPCP, Adler et al. 2003). MERRA-2 exhibits larger temporal
791 variability than GPCP but similar temporal variability as other recent reanalyses, and
792 noticeably less spurious temporal variability than MERRA. The largest improvements
793 compared with MERRA in this regard relate to the decreased sensitivity of MERRA-2
794 to the introduction of AMSU-A radiances on NOAA-15 and -16 in the late 1990s, and
795 to the loss of SSM/I radiances in the late 2000s. There is still an obvious sensitivity
796 in MERRA-2 to the introduction of SSM/I in 1987, but the response to these data

797 is comparable in magnitude to those of the other reanalyses shown. The response in
 798 MERRA-2 appears accentuated due to the decrease and subsequent recovery of precip-
 799 itation through the mid 1980s. This behavior is not reflected in the GPCP time series,
 800 but is evident to lesser degrees in CFSR and ERA-Interim, especially after 1983. For
 801 MERRA-2 and CFSR, this may be related to the fact that the SST boundary condi-
 802 tions used in these reanalyses reach their global minimum value for the entire reanalysis
 803 period after 1985 (Figure 5), but further investigation is required to confirm this. The
 804 increasing trend in global precipitation in MERRA-2 from approximately 2.9 mm day^{-1}
 805 in 1988 to approximately 3.0 mm day^{-1} in 1998 is likely due to increasing evaporation
 806 over oceans driven by the assimilation of additional SSM/I wind speed observations and
 807 the tight coupling of evaporation and precipitation in MERRA-2 through the global
 808 mass constraint (Bosilovich et al. 2017). Overall, the global mean precipitation values
 809 are higher than those of GPCP but well within the envelope of other recent reanalyses.

810 Spatial comparisons provide additional insight into the strengths and weaknesses of the
 811 representation of precipitation globally in MERRA-2. Figure 16 shows maps of time-
 812 averaged differences in precipitation during boreal summer for MERRA and MERRA-2
 813 compared with GPCP. MERRA-2 shows general improvement compared to MERRA
 814 over oceanic regions in both the tropics and extratropics, but an increase in positive
 815 bias over northern high latitudes. A notable deficiency in MERRA-2 is the excessive
 816 precipitation in the vicinity of high topography in the tropics, especially along the Andes
 817 and over the maritime continent. This is related to the partitioning between resolved
 818 (large scale) and parameterized (convective) precipitation in the MERRA-2 model which,
 819 being more heavily skewed toward the former, results in large-scale precipitation over
 820 high topography that is difficult to control. In comparing these features with available
 821 gauge data, Bosilovich et al. (2015) point out that the maximum precipitation values
 822 in MERRA-2 do not always coincide with the maximum terrain height, so that other

823 effects also may play a role locally. Despite this deficiency over tropical land areas, the
824 positive bias over the warm pool present in MERRA is slightly improved in MERRA-2.
825 Additionally, the high precipitation bias over the Central America Sea in MERRA has
826 been reduced significantly in MERRA-2 and precipitation over the Bay of Bengal and
827 Arabian Sea is slightly improved. Results for other seasons (not shown) are qualitatively
828 similar to those in Figure 16.

829 *b. US summertime precipitation variability*

830 Deficiencies in the ability of MERRA to reproduce certain aspects of the summer-
831 time seasonal precipitation over the United States (US) have been well documented
832 (Bosilovich 2013). In particular, MERRA was unable to produce seasonal highs and
833 lows in regional precipitation that were similar to observations. For example, droughts
834 and floods were only weakly reproduced.

835 Figure 17 shows the time series of summertime seasonal precipitation anomalies over
836 the midwestern US as derived from the NOAA Climate Prediction Center (CPC) gauge
837 observations and from MERRA and MERRA-2 model-generated precipitation. (The
838 correlation values between various reanalyses and the gauge data for this and other
839 regions of the US are shown in Figure 18.) The limitations of MERRA are apparent,
840 especially when comparing values for 1988 (regional drought) and 1993 (large-scale flood-
841 ing) with the observed values. In contrast, MERRA-2 is able to reproduce the 1988 and
842 1993 anomalies and is generally much better at tracking the overall variability of the
843 observed anomalies. The poor performance of MERRA-2 in 1980 is a notable exception.
844 A significant drought occurred in the southern Great Plains that year, but its location
845 in MERRA-2 extended too far northeastward into the midwestern US.

Figure 18 presents regional summary statistics for US summer seasonal precipitation anomalies for selected reanalyses. The regions are defined as in Bosilovich (2013). For each region, the temporal mean, standard deviation, and anomaly correlation with respect to the CPC data are derived from time series like those shown in Figure 17. In general, precipitation mean values across the US are improved in MERRA-2 compared with MERRA (Figure 18a), and in many regions the values for MERRA-2 improve over those of other reanalyses as well. There is also a marked increase in the standard deviation of the MERRA-2 time series relative to MERRA (Figure 18b). As discussed above, for example, MERRA-2 more realistically reproduces the seasonal extremes in midwestern US precipitation. Note, however, that MERRA-2 overestimates the standard deviation with respect to the CPC estimates in some regions. Ancillary results indicate that this is due to an excess in the number of days with rain in MERRA-2. Improvements in MERRA-2 are most evident in the anomaly correlation of the seasonal time series (Figure 18c). In this measure, the two most recent reanalyses, JRA-55 and MERRA-2, generally outperform the others. MERRA-2 produces the highest values of the reanalyses shown in most regions, with substantially higher values in a few of these regions.

The detection and analysis of extreme weather, including extreme precipitation events, is a topic of societal interest and another potential application of reanalyses. At least some of this interest is related to assessing changes in the risk of such events in the context of climate change. For example, observation-based studies cite strong evidence of an upward trend in the frequency and intensity of extreme precipitation events averaged over the US during the last 50 years (Kunkel et al. 2013), although the causes of the observed trends are less certain. Figure 19 shows the accumulated precipitation amounts for the largest precipitation events (at the 99th percentile) as derived from gauge observations, MERRA, and MERRA-2. Compared with the observations, MERRA shows

872 very low values, and very little structure across the continental US. MERRA-2, on the
873 other hand, exhibits a spatial pattern more similar to the observations, and the magni-
874 tude of the extreme rainfall is also more similar to the observations. MERRA-2 does,
875 however, overestimate the precipitation values over the Midwestern US. While the re-
876 sults in Figure 19 provide an indicator of how the representation of extreme events has
877 improved in MERRA-2 compared with MERRA, the relatively coarse resolution of both
878 reanalyses limits their utility for studying such events in detail. Presumably, the trend
879 toward increasing resolution, among other improvements, will reduce these limitations
880 in future global reanalyses.

881 **6. The stratosphere**

882 In MERRA-2 the stratospheric meteorology and ozone have benefited from improve-
883 ments to the GEOS atmospheric model and GSI analysis scheme, as well as from the
884 addition of observations that were not incorporated into MERRA. The model changes
885 most relevant to the stratosphere are the use of the cubed sphere grid and the re-tuning
886 of the gravity wave drag (GWD) parameterization. The amplitude of the non-orographic
887 GWD was increased in the tropics, enabling a model-generated Quasi-Biennial Oscilla-
888 tion (QBO) that was not found in the model version used for MERRA (Molod et al.
889 2015). Having a model-generated QBO, in turn, results in smaller lower-stratospheric
890 analysis wind increments in MERRA-2 than in MERRA (Coy et al. 2016). The strength
891 of the orographic GWD was also increased in the Southern Hemisphere to better model
892 the strong, late-winter westerlies found there (Molod et al. 2015).

893 The main GSI change relevant to the stratosphere is the use in MERRA-2 of the CRTM
894 for the assimilation of SSU radiances while in MERRA the SSU assimilation was based
895 on GLATOVs (section 2d). These SSU radiance channels are a major source of strato-

spheric information during the 1980's and 1990's, although the SSU instruments during these decades span several satellite platforms, each with different bias characteristics (Kobayashi et al. 2009). The CRTM has been enhanced for SSU data assimilation since MERRA and now accounts for these biasing factors.

The main additional observations relevant to the stratosphere for MERRA-2 are GPSRO bending angle observations from the suite of platforms beginning in July 2004, and temperature and ozone measurements of the middle atmosphere from MLS and OMI on the EOS Aura satellite beginning later the same year (Froidevaux et al. 2006; Schwartz et al. 2008; McPeters et al. 2008). MERRA-2 assimilates GPSRO bending angle observations up to 30 km. Details of the GPSRO platforms assimilated by MERRA-2 can be found in McCarty et al. (2016). The GPSRO observations aid lower stratospheric bias correction by providing a stable source of temperature and moisture measurements. The MLS-retrieved temperature profiles are assimilated in MERRA-2 at altitudes above 5 hPa, providing a strong constraint on the dynamics of the stratopause and lower mesosphere. As shown below in section 6a, this improves the quality of the synoptic meteorological fields at these altitudes but may complicate the study of trends. The MLS and OMI contributions to ozone assimilation are discussed in section 6b.

a. Meteorology

The cubed sphere discretization of the MERRA-2 model eliminates computational instabilities near the poles, a characteristic of latitude-longitude grids. This is especially important for stratospheric analysis where strong cross-polar flow events occur frequently, especially during major sudden warming events, as planetary-scale Rossby waves disturb the polar vortex. Ertel's Potential Vorticity (EPV), a scalar based on the horizontal vorticity, is often used to characterize the stratospheric circulation (Andrews et al. 1987),

920 where stronger EPV gradients imply stronger flow. Figure 20 illustrates a case where
 921 the analyzed wind speeds in MERRA-2 reached nearly 170 m s^{-1} close to the polar
 922 stratopause on 2 January 1995 at 12 UTC. On a global scale (Figure 20a and b), the
 923 MERRA and MERRA-2 EPV fields appear similar, with the polar vortex (indicated by
 924 green and orange colors) displaced well off the pole. In both cases, strong winds cross
 925 the North Pole as they circle around the region of high EPV. However, a closer look
 926 reveals that the EPV in MERRA (Figure 20c) has anomalous radial perturbations near
 927 the pole, while the EPV in MERRA-2 (Figure 20d) shows a smooth and strong EPV
 928 gradient in this region. Note also that while the largest discontinuities in the MERRA
 929 EPV field occur close to the pole itself, their effects can extend well beyond this location.

930 Figure 21 provides an example of how the assimilation of MLS temperature measure-
 931 ments in MERRA-2 improves the representation of the dynamics near the stratopause.
 932 The figure shows the time-height evolution of polar temperatures during the 2005–2006
 933 Northern Hemisphere winter in which a major stratospheric sudden warming occurred.
 934 In a comprehensive study of this winter based on MLS observations, Manney et al.
 935 (2008) documented the disappearance of the warm polar stratopause during the warm-
 936 ing and its later high-altitude reformation and subsequent descent. This breakdown
 937 and high-altitude reformation in early February 2006 is now well captured in MERRA-2
 938 (Figure 21b), in contrast to MERRA (Figure 21a).

939 The characteristics of the assimilation on longer time scales is illustrated in Figure 22,
 940 which shows the time-height evolution of global monthly averaged temperature anomalies
 941 in MERRA-2. The 35-year mean and annual cycle for the period 1980–2015 have been
 942 subtracted from each pressure level. The global temperatures in the lower stratosphere
 943 (100–10 hPa) show no obvious discontinuities as different instruments become available.
 944 There is a slight cooling with time over the 35 years, which is generally consistent with

945 recent analyses of the satellite-based stratospheric climate data record (see Seidel et al.,
 946 2016 and references therein). There are also episodic temperature increases associated
 947 with the two large volcanic eruptions, El Chichon in 1982 and Pinatubo in 1991. In
 948 the upper stratosphere, several discontinuities can be seen. There is a marked decrease
 949 in temperature near 1 hPa in 1995 when the transition from assimilating NOAA-11
 950 to NOAA-14 SSU channel 3 radiances occurs. The latter are demonstrably cooler (see
 951 Figure 16 of McCarty et al. 2016) and are assimilated without bias correction because of
 952 the relatively large model errors at this level. There is an overall increase in temperature
 953 when AMSU-A data are first assimilated in 1998, which was not as apparent in MERRA
 954 (Rienecker et al. 2011) due to the overlapping use of SSU channel 3 and AMSU-A
 955 channel 14 radiances in that reanalysis. The overall effect of assimilating the MLS
 956 temperature profiles beginning in 2004 is to sharpen the stratopause with warming at
 957 approximately 1 hPa and cooling above and below this level.

958 *b. Ozone*

959 The most notable aspects of the MERRA-2 ozone analysis, and those that constitute
 960 the main differences with MERRA, are the use of the improved version of SBUV data
 961 prior to October 2004 and subsequent assimilation of OMI and MLS observations. The
 962 latter provides high vertical resolution (~ 2.5 km) measurements of stratospheric ozone
 963 profiles during both night and day. The specification of background errors for ozone has
 964 also been upgraded to account for flow dependent error standard deviations as described
 965 in Wargan et al. (2015).

966 Many ozone data sets exist for various periods between 1980 and present. The decision
 967 to use only SBUV, MLS and OMI observations in MERRA-2 was motivated by the
 968 desire to avoid introducing multiple discontinuities into the ozone observing system

969 while taking advantage of high-quality data offered by SBUV and EOS Aura retrievals.
970 This approach leads to a relatively homogeneous MERRA-2 ozone record with only one
971 major discontinuity in 2004 when MLS and OMI data replace SBUV observations. The
972 price is a degraded quality of the analyzed ozone during the short periods when the
973 selected data are not available, most notably in the Southern Hemisphere in late 1994,
974 as discussed below.

975 An initial evaluation of the representation of ozone in MERRA-2 was presented in
976 Bosilovich et al (2015). A more comprehensive validation against independent satel-
977 lite and ozonesonde data, including evaluation of the vertical structure and variability,
978 is given in Wargan et al. (2017). In particular, it is shown there that the assimilation of
979 MLS observations in MERRA-2 leads to significant improvements in the representation
980 of lower stratospheric ozone when compared with MERRA or compared with the period
981 of SBUV assimilation in MERRA-2. The QBO signal in ozone is discussed in Coy et al.
982 (2016), who demonstrate an improvement in the vertical structure of the ozone QBO
983 signature from 2004 onward, when MLS data are assimilated in MERRA-2. The focus
984 here is on the Antarctic total column ozone in order to illustrate that MERRA-2 has
985 realistic climatic ozone in a poorly observed region, while also highlighting some of its
986 uncertainties. Two examples are presented: a comparative evaluation of the South Pole
987 ozone in MERRA and MERRA-2 and the representation of Antarctic ozone holes in the
988 present reanalysis. The former follows Wargan et al. (2017).

989 Figure 23a shows the time series of total ozone derived from ozonesonde measurements at
990 the South Pole, along with MERRA and MERRA-2 output sampled at the ozonesonde
991 times and location between 1986 and 2015. The ozonesonde data, including the inte-
992 grated column values were obtained from the Earth System Research Laboratory website
993 (<http://www.esrl.noaa.gov/gmd/ozwv/ozsondes/spo.html>). Note that the vertical range

994 of balloon-borne measurements typically does not extend to pressure levels above 10 hPa
 995 and so the upper-stratospheric portion of the column is obtained by extrapolating the
 996 mixing ratios from 7 hPa or from the highest observed altitude, whichever is lower. For
 997 completeness, Figure 23a also shows the reanalysis data between 1980 and 1985. In
 998 the absence of ozonesondes, the reanalyses are sampled four times monthly in one-week
 999 intervals for that period. The differences between each reanalysis and the ozonesonde
 1000 values are plotted in Figure 23b. Overall, both reanalyses capture the annual cycle and
 1001 much of the interannual variability observed in the ozonesonde data, although there
 1002 are large discrepancies (greater than 50%) during austral summer months in MERRA-2
 1003 prior to 2005 and in MERRA throughout the period of comparison. This is consis-
 1004 tent with the fact that the reanalyses are not constrained by SBUV data during polar
 1005 night. In addition, in late 1994, the SBUV coverage was limited to latitudes north of
 1006 approximately 30°S owing to an orbital drift of the NOAA-11 satellite, which left the
 1007 middle and high southern latitudes unobserved in both reanalyses. Nonetheless, these
 1008 differences are reduced in MERRA-2 compared to MERRA. MERRA-2 performs sig-
 1009 nificantly better than MERRA relative to the South Pole ozonesondes from October
 1010 2004 onward, when EOS Aura ozone data are assimilated. In particular, the standard
 1011 deviation of the differences between MERRA-2 and the ozonesonde values drops from
 1012 12.5% between 1991 and 2004 to 5% between 2005 and 2014. At the same time, the
 1013 correlation between MERRA-2 and the ozonesonde measurements increases from 0.88
 1014 to 0.98. The large excursions seen in Figure 23b in MERRA between 2008 and 2012 are
 1015 due to degraded coverage of the NOAA-17 SBUV instrument. In contrast, the behavior
 1016 of the MERRA-2 South Pole ozone is remarkably steady relative to the ozonesondes in
 1017 the period when MLS and OMI data are assimilated. Only small seasonal variations
 1018 are seen during that period. The MERRA-2 South Pole total ozone exhibits a small
 1019 negative bias of approximately 6.7 Dobson units (DU), or roughly 2%, throughout the

1020 period of comparison. This bias does not vary significantly between the periods when
1021 either SBUV or EOS Aura ozone data are assimilated.

1022 As discovered by Molina and Rowland (1974), anthropogenic emissions of chlorofluo-
1023 rocarbons provide the main contribution to the chlorine loading in the stratosphere,
1024 leading to destruction of the ozone layer. One prominent feature of the ozone loss in
1025 recent decades is the occurrence of springtime ozone holes over Antarctica since the
1026 early 1980's (Farman et al. 1985). Ozone holes are regions of extremely low values of
1027 total ozone forming inside the polar vortex due to a series of chlorine-catalyzed reactions
1028 (WMO 2014). The climatological importance of this phenomenon warrants its accurate
1029 representation in long-term reanalyses. The discussion here focuses on only one simple
1030 diagnostic, the ozone hole area, defined as the region with total ozone values less than
1031 220 DU.

1032 Figure 24 shows the time series of the ozone hole area calculated from the MERRA-2
1033 total ozone averaged between 20 September and 10 October in each year between 1980
1034 and 2015. Also plotted in Figure 24 are the ozone hole area values derived from the Total
1035 Ozone Mapping Spectrometer (TOMS) instruments on Nimbus-7 (1980–1992), Meteor-3
1036 (1992–1994) and Earth Probe (1996–2005), and from OMI (2004–2015). Note that OMI
1037 data are assimilated in MERRA-2 but TOMS observations are not. With the excep-
1038 tion of 1994 there is remarkable agreement between MERRA-2 and these observations.
1039 In particular, MERRA-2 realistically captures the ozone hole interannual variability
1040 throughout the period of the reanalysis. There is an upward trend between 1980 and
1041 the mid-1990s followed by a plateau with the area oscillating around 22×10^6 km².
1042 This is consistent with the late twentieth century increase of anthropogenic chlorine and
1043 bromine loadings and the subsequent slow recovery after the gradual implementation of
1044 the Montreal Protocol of 1986 (WMO 2014). The Protocol, which went into effect in the

late 1990s, banned the release of the main ozone depleting substances. Because the rate of the springtime polar ozone depletion depends on temperature and the strength of the Antarctic polar vortex in a given year, the size of the ozone hole exhibits a dynamically driven interannual variability superimposed on decadal-scale trends. This dynamical modulation is also evident in Figure 24. The extremely small (less than 3×10^6 km²) ozone hole in 2002 occurred in conjunction with the only major sudden stratospheric warming in the Southern Hemisphere on record (Newman and Nash 2005).

It should be noted that the southern high-latitude ozone for 1994 in MERRA-2 is not recommended for scientific use. The degraded result for that year is due to limited SBUV data coverage, as explained above, and the decision not to use data sources other than SBUV, OMI and MLS throughout the reanalysis. This particular deficiency is not shared with other major reanalyses (except MERRA), which replaced the missing data with other available observations such as from the short-lived Meteor-3 TOMS instrument (ERA-Interim) or NOAA-9 SBUV (CFSR and JRA-55). The latter were not considered in MERRA-2 because of the poorer quality of its partial columns compared to other SBUV instruments.

Realistic ozone hole interannual variability is also present in MERRA (Sean M. Davis, personal communication 2016) with the exception of 1993, 1994 (as in MERRA-2), and the period between 2010 and 2012 when poor coverage from NOAA-17 SBUV resulted in degraded quality of the Antarctic ozone. The inferior performance of MERRA in 1993 compared to MERRA-2 is a consequence of applying more stringent data quality criteria to the older version of the SBUV data, resulting in limited data coverage near the terminator.

1068 7. Representation of the cryosphere

1069 Reanalyses provide a global context for assessing recent, pronounced high latitude cli-
1070 mate variability and provide seamless information on linkages to lower latitudes. As
1071 compared to midlatitudes, reanalyses in polar regions are particularly challenged by the
1072 paucity of the *in-situ* observational network, by the difficulty of satellite microwave and
1073 infrared sensors to profile the lower atmosphere over snow and ice surfaces, and by an
1074 inadequate representation of physical processes in models that are specific to these areas.
1075 Of these three challenges, improvement of model representations of physical processes—
1076 particularly as they relate to ice and snow surfaces—was seen as the most tractable in
1077 the development of MERRA-2.

1078 Several changes in the representation of physical processes between MERRA and MERRA-
1079 2 are directly relevant to polar regions. These include the use in MERRA-2 of the
1080 cubed-sphere computational grid (e.g., Putman and Lin 2007), which removes the need
1081 for gravity wave filtering at high latitudes, as well as daily sea ice concentration and
1082 sea surface temperature boundary conditions (Donlon et al. 2012; Reynolds et al. 2007;
1083 Taylor et al. 2000), as compared with the weekly fields used in MERRA.

1084 In MERRA, a fixed surface albedo of 0.6 was used with sea-ice cover. This resulted in
1085 erroneously warm surface temperatures in the Arctic spring, when the observed albedo
1086 is typically much higher (Cullather and Bosilovich 2012). In MERRA-2, Northern Hemi-
1087 sphere sea-ice albedo varies seasonally based on flux tower observations from the Surface
1088 Heat Budget of the Arctic Ocean (SHEBA) field experiment (Duynderke and de Roode
1089 2001). Monthly values are computed and then linearly interpolated in time to produce
1090 instantaneous values. Sea-ice albedo in the Southern Hemisphere remains fixed as in
1091 MERRA, as there are few reliable albedo observations there. Sea ice in the Southern

1092 Hemisphere also does not endure an extended period of surface melting and a resulting
1093 decreased albedo as in the Northern Hemisphere. Comparisons with SHEBA observa-
1094 tions indicate a substantial reduction in 2-m air temperature biases during boreal spring
1095 in MERRA-2.

1096 These comparisons also find a warm bias in winter months over sea ice in MERRA-2
1097 of approximately 1.2°C in comparison to SHEBA. Larger air temperature differences
1098 of greater than 3°C are found in comparison to Soviet ice drifting station observations
1099 made during the 1980's (Colony et al. 1992). Simmons et al. (2016) showed that
1100 MERRA-2 is an outlier in near-surface temperature trends in polar regions as compared
1101 to ERA-Interim, JRA-55, and several conventional data sets. For the period 1980–
1102 2009, annual 2-m air temperatures for the north polar cap bounded by 60°N increased
1103 by $0.35 \pm 0.08^{\circ}\text{C}$ per decade in MERRA-2. This is the trend determined from linear
1104 regression; the uncertainty denotes the standard error of the trend. By comparison,
1105 north polar cap temperatures increased by $0.46 \pm 0.09^{\circ}\text{C}$ per decade in NOAA CFSR,
1106 by $0.55 \pm 0.10^{\circ}\text{C}$ per decade in ERA-Interim, and by $0.56 \pm 0.09^{\circ}\text{C}$ per decade in JRA-
1107 55. The behavior in MERRA-2 may be attributable to spurious changes in the SST and
1108 SIC boundary conditions and the response of the model to changes in surface forcing.
1109 Investigation of these issues is ongoing.

1110 A particular focus during the development of MERRA-2 was on the representation of
1111 glaciated land surfaces (Cullather et al. 2014). In MERRA, ice sheets had an unrealistic
1112 design, with a fixed surface albedo and no representation of surface hydrology. Surface
1113 energy fluxes were computed using a fixed sub-surface temperature of 230 K (-43°C). In
1114 MERRA-2, energy conduction properties of the upper 15 meters of ice are represented,
1115 as well as the energy and hydrologic properties of an overlying, variable snow cover.
1116 Snow hydrology follows a modified version of the Stieglitz model that is also used over

1117 terrestrial land surfaces (Lynch-Stieglitz 1994; Stieglitz et al. 2001). This provides an
1118 explicit representation of snow densification, meltwater runoff, percolation, refreezing,
1119 and a prognostic surface albedo based on Greuell and Konzelmann (1994).

1120 Figure 25 shows the effects of the different surface configurations in MERRA and
1121 MERRA-2 on near-surface air temperatures over ice sheets. In MERRA, biases are
1122 found when the observed surface temperature differs markedly from the fixed sub-surface
1123 temperature of -43°C . This includes South Pole station in winter (Figure 25a), where
1124 MERRA values are more than 5 K too warm; over the central Ross Ice Shelf in summer
1125 (Figure 25b), where MERRA is 8 K too cold; and over central Greenland in summer
1126 (Figure 25c), where MERRA is 4 K too cold. It may be seen from Figure 25 that these
1127 seasonal air temperature differences between MERRA and the station values are signifi-
1128 cant over interannual time periods. In contrast, 2-m air temperatures for these locations
1129 in MERRA-2 more closely agree with the observed values.

1130 The surface representation in MERRA-2 also allows for the computation of surface
1131 mass balance over ice sheets, which may be defined as the net of precipitation minus
1132 evaporation minus runoff. The MERRA system does not provide runoff over land ice
1133 and, as seen in Figure 26, lacks ablation areas (in which the annual surface mass balance
1134 is negative) along the periphery of the ice sheet. For Greenland these occur mostly as a
1135 result of runoff from surface melt. The corresponding fields in MERRA-2, on the other
1136 hand, compare well with those from the widely-used *Modèle Atmosphérique Régional*
1137 regional climate model (MAR; Fettweis 2007), particularly in terms of the accumulation
1138 distribution in southeastern and western Greenland and the location of the zero-contour
1139 line along the western coast. However, some differences are also evident. For example,
1140 the regional climate model indicates average annual mean ablation values of up to 4 m
1141 yr^{-1} in southwestern Greenland, as compared with values of approximately 1 m yr^{-1} in

MERRA-2. In addition to differing surface representations, differences in grid spacing between MAR (25 km) and MERRA-2 (roughly 50 km) may also play a role. A final point of comparison in Figure 26 is with regard to topography. The MERRA system used a dated topography which contained large errors of up to 600 m over the Greenland Ice Sheet (Box and Rinke 2003). These differences are apparent in the topography contours shown for MERRA and MERRA-2 in Figure 26.

8. MERRA-2 products and access

The complete list of analyzed and diagnosed fields produced by MERRA-2 is given in the product file specification document available at the GMAO's MERRA-2 web site (<https://gmao.gsfc.nasa.gov/pubs/docs/Bosilovich785.pdf>). The GEOS IAU procedure allows for higher-frequency products than just the 6-hourly ones generated directly from the analysis. There are three time-invariant and 39 time-varying product collections, all produced on a $0.625^\circ \times 0.5^\circ$ horizontal grid. Variables are provided on either the native vertical grid (at 72 model layers or the 73 edges), or interpolated to 42 standard pressure levels. Detailed information and a description of each variable are available in the MERRA-2 file specification document. As in MERRA, MERRA-2 provides closed atmospheric budgets, including the analysis increment terms. The observational forcing from the assimilation increments during the IAU segment is summed in the output budgets of the model. Bosilovich et al. (2015) show the magnitudes of these terms in water and energy budgets.

The NASA Goddard Earth Sciences Data Information Services Center (GES DISC) provides access to MERRA-2 products through a new unified user interface connected to three different search engines. Many of the tools will be familiar to MERRA users, such as the popular Giovanni visualization and analysis tool, web based FTP servers

1166 and OpenDAP web services. The subsetting capability has been updated to include
1167 grid transformation options, while retaining the essential functionality of selecting lev-
1168 els, variables, time and domain. Citations for the individual MERRA-2 data collections
1169 are included in the GES DISC MERRA-2 data access pages. As noted in section 1,
1170 these citations are included in the figure captions of this paper (except where results for
1171 MERRA-2 are derived from other sources such as diagnostic output from the data assim-
1172 ilation scheme). Results shown for MERRA are from similarly named data collections,
1173 as described by Rienecker et al. (2011).

1174 **9. Summary and outlook**

1175 The Modern Era Retrospective Analysis for Research Applications Version 2 (MERRA-
1176 2) was developed with two primary objectives: to provide an ongoing near-real time cli-
1177 mate analysis of the satellite era that addresses known limitations of the now-completed
1178 MERRA reanalysis (January 1979–February 2016), and to demonstrate progress toward
1179 development of a future integrated Earth system analysis (IESA) capability. MERRA-2
1180 has achieved those objectives in several respects. These include the assimilation of satel-
1181 lite observations not available to MERRA—which assimilated no new satellite observa-
1182 tions after NOAA-18 (launched in 2005)—the reduction of certain biases and imbalances
1183 in the water cycle, and the reduction of spurious trends and jumps in precipitation related
1184 to changes in the observing system. As a step toward a future IESA, MERRA-2 includes
1185 aerosol data assimilation and improved representations of aspects of the cryosphere and
1186 stratosphere, including ozone, as compared with MERRA.

1187 At the same time, because of the fairly rapid development schedule required to produce
1188 a timely replacement for MERRA, other aspects of the MERRA-2 development received
1189 less attention. For example, there was little focus on the preparation and improvement of

1190 input conventional data types and minimal tuning of the model physics for the current
1191 application. Notable shortcomings of MERRA-2 compared with MERRA include an
1192 increased warm bias in the upper troposphere—as revealed by the background forecast fit
1193 to radiosonde temperature observations and mean analysis increments of temperature—
1194 as well as excessive precipitation over high topography in the tropics and, to a lesser
1195 extent, over northern high latitudes. Subsequent experimentation indicates that these
1196 behaviors are most affected by the model parameterizations of deep convection and
1197 gravity wave drag in GEOS, as well as the representation of topography. They are being
1198 addressed in more recent model versions.

1199 Ongoing development in other aspects of modeling and data assimilation are likely to pro-
1200 vide benefit for reanalyses in the near future. For example, while MERRA-2 assimilates
1201 only clear-sky satellite radiances, the use of cloud- and rain-affected radiances—referred
1202 to as all-sky assimilation (Bauer et al. 2010)—has matured or become operational at
1203 several centers including GMAO. This should improve the assimilation of moisture-
1204 sensitive data types which, as shown here and by Bosilovich et al. (2017), can still
1205 induce unexpected changes in global precipitation and moisture fields. Direct assimi-
1206 lation of land surface observations, including remotely sensed soil moisture and snow
1207 cover fraction, is another area of improving capability that is likely to provide bene-
1208 fit to reanalysis, especially for capturing extreme events like droughts and heat waves.
1209 Implementation of an improved land model that includes dynamic phenology and pho-
1210 tosynthesis is a key component of the GMAO’s land surface modeling and assimilation
1211 efforts (Koster et al. 2014). To improve the specification of ocean surface boundary
1212 conditions, many centers are developing some form of coupled ocean-atmosphere anal-
1213 ysis system. The GMAO has recently implemented a coupled data assimilation scheme
1214 for analyzing ocean skin temperature within the existing atmospheric analysis (Akella
1215 et al. 2016). It uses background fields from a near-surface ocean diurnal layer model

1216 to assimilate surface-sensitive radiances plus in-situ observations along with all other
1217 observations in the atmospheric assimilation system. The scheme may be described as
1218 being weakly coupled in the sense that the atmospheric observations do not affect the
1219 ocean fields directly, but only through the increment of ocean skin temperature during
1220 the next analysis cycle.

1221 Improving the representation of aerosol effects on climate is another important area of
1222 development for reanalysis. As the aerosol observing system continues to evolve and
1223 provide additional global information on aerosol absorption, size and vertical distribu-
1224 tion, the discrepancy among reanalyses and satellite-only estimates of aerosol radiative-
1225 climate effects should decrease. For example, the GMAO is working to incorporate
1226 aerosol vertical distribution information from space-based lidars, as well as implicit spe-
1227 ciation and size information from multi-channel radiometers on low-orbiting and geosta-
1228 tionary satellites. Unlike satellite estimates alone, reanalyses like MERRA-2 can provide
1229 detailed information on how the anthropogenic component of aerosols, and thus radia-
1230 tive forcing, has changed during the modern satellite era, as well as its interaction with
1231 the circulation and the climate at large. This should lead to reduced uncertainty in
1232 assessing, for example, the human impact on climate.

1233 More extensive analysis coupling between the atmosphere, ocean, land and chemistry as
1234 envisioned for IESA, while progressing, still presents significant challenges (e.g., Brass-
1235 ington et al. 2015). These include model biases that can be exacerbated when coupled,
1236 component systems with different physical characteristics and different spatial and tem-
1237 poral scales, and component observations in different media with different spatial and
1238 temporal frequencies and different latencies. These challenges may be offset at least
1239 partially by the fact that, in practice, where the time scales and observation laten-
1240 cies between components differ greatly—as between the deep ocean and atmosphere for

1241 example—a weak coupling approach may suffice. Prospects for success are also bolstered
1242 by the fact that the numerical weather prediction community is placing increasing focus
1243 on the need to analyze currently uncoupled components of the Earth system in a more
1244 consistent manner. The GMAO strategy is to progress incrementally toward an IESA
1245 through an evolving combination of coupled systems and offline component reanalyses
1246 driven by, for example, MERRA-2 atmospheric forcing.

1247 Quantifying uncertainty in reanalyses remains important for expanding their utility,
1248 especially as a potential tool for climate change assessment. Dee et al. (2011) argued
1249 that advances in observational bias correction and other aspects of data assimilation
1250 have reduced uncertainty in the representation of low-frequency variability to the point
1251 where ERA-Interim can be used to estimate certain atmospheric temperature trends.
1252 More recently, Simmons et al. (2014) compared multi-annual variability and trends
1253 in atmospheric temperature from ERA-Interim, JRA-55 and MERRA and found them
1254 to be in generally good agreement in the upper troposphere and lower stratosphere
1255 but more uncertain in the middle stratosphere. Nonetheless, for less well constrained
1256 quantities such as precipitation and surface fluxes, there still appear to be substantial
1257 differences between recent reanalyses. For example, the 12-month running mean values
1258 of global precipitation in ERA-Interim, MERRA-2, and JRA-55 can at times differ by
1259 almost 20%. Uncertainty in sea surface temperature, as illustrated by the surprising
1260 differences between the prescribed values used in different reanalyses (Figure 5) is likely
1261 to be a contributing factor. Impacts from observing system changes also appear to play
1262 a significant role in explaining these precipitation differences, pointing to the need for
1263 new sources of high-quality observations of these or closely related variables not only
1264 for assimilation but for improving our understanding and modeling of the underlying
1265 physical processes. Ongoing efforts to improve the quality of existing historical data
1266 sets are also critical in this regard.

1267 The increasing use of ensemble and hybrid ensemble-variational methods in Earth sys-
1268 tem data assimilation has the potential to make at least some measures of uncertainty a
1269 standard component of reanalysis data sets (e.g., Compo et al. 2011; Poli et al. 2013).
1270 The GMAO has recently implemented a hybrid four-dimensional ensemble-variational
1271 (4D-ENVAR) assimilation scheme with similar capability. Finally, ECMWF, JMA and
1272 GMAO are conducting multi-decadal atmospheric model integrations (without data as-
1273 simulation) for comparison with reanalyses as a means of assessing internal variability
1274 and distinguishing boundary-forced climate signals from those imposed by changes in
1275 the observing system. All these efforts will benefit from the continued assessment of ex-
1276 isting reanalysis products by the research community, and from the sharing of key data
1277 assimilation diagnostic quantities (e.g., background departures, analysis increments, bias
1278 estimates) between both reanalysis developers and data providers.

1279 **Acknowledgments**

1280 Development of the GEOS data assimilation system and the MERRA-2 project were
1281 funded by NASA’s Modeling Analysis and Prediction program. Computational resources
1282 and support for the execution of MERRA-2 were provided by the NASA High-End
1283 Computing Capability Project and NASA Center for Climate Simulation. GEOS and
1284 MERRA-2 are the result of years of dedicated research, development and analysis by
1285 many individuals at GMAO whose efforts are greatly appreciated. We gratefully ac-
1286 knowledge the GMAO operations group for monitoring the production of MERRA-2
1287 and the GMAO software integration group who helped improve the performance and
1288 flexibility of GEOS. We thank Julio Bacmeister for his contribution to the development
1289 of the model physics, Qing Liu for processing the precipitation input data, and Allison
1290 Collow and Edmond Brent Smith for providing some of the figures for this paper. We

1291 also thank the GES DISC for providing on-line access to MERRA-2 products. Finally,
1292 we thank the three reviewers, whose comments and suggestions helped improve the paper
1293 substantially.

3DVAR	Three-dimensional variational data assimilation
4DENVAR	Four-dimensional ensemble-variational data assimilation
AAOD	Aerosol absorption optical depth
ACARS	Aircraft Communications Addressing and Reporting
AeroCom	Aerosol Comparison Project
AERONET	Aerosol Robotics Network
AIREP	Aircraft report
AIRS	Advanced Infrared Sounder
AMDAR	Aircraft Meteorological Data Relay
AMSR-E	Advanced Microwave Scanning Radiometer-EOS
AMSU-A	Advanced Microwave Sounding Unit-A
AMSU-B	Advanced Microwave Sounding Unit-B
AOD	Aerosol optical depth
ASCAT	Advanced Scatterometer
ASDAR	Aircraft to Satellite Data Relay
ATMS	Advanced Technology Microwave Sounder
ATOVS	Advanced TIROS Operational Vertical Sounder
AVHRR	Advanced Very High Resolution Radiometer
CFSR	Climate Forecast System Reanalysis
CAMS	Copernicus Atmosphere Monitoring Service
CMIP	Coupled Model Intercomparison Project
CPC	Climate Prediction Center
CrIS	Cross-track Infrared Sounder
CRTM	Community Radiative Transfer Model

DMSP	Defense Meteorological Satellite Program
DRE	Direct radiative effect
ECMWF	European Centre for Medium-Range Weather Forecasts
EOS	Earth Observing System
ERA-20C	ECMWF Reanalysis from 1900–2010
ERA-Interim	ECMWF Reanalysis from 1979–present
ERS	Environmental Research Satellite
FGAT	First guess at appropriate time
GEOS	Goddard Earth Observing System
GES DISC	Goddard Earth Sciences Data Information Services Center
GLATOVs	Goddard Laboratory for Atmospheres TOVS forward model
GMAO	Global Modeling and Assimilation Office
1296 GMS	Geostationary Meteorological Satellite
GOCART	Goddard Chemistry, Aerosol, Radiation and Transport model
GOES	Geostationary Operational Environmental Satellites
GPCP	Global Precipitation Climatology Project
GPSRO	Global Positioning System radio occultation
GSI	Gridpoint Statistical Interpolation
GWD	Gravity wave drag
HIRS	High-resolution Infrared Radiation Sounder
IASI	Infrared Atmospheric Sounding Interferometer
IAU	Incremental analysis update
IESA	Integrated Earth system analysis
IPCC	Intergovernmental Panel on Climate Change
JMA	Japan Meteorological Agency

JPSS	Joint Polar Satellite System
JRA-55	Japanese 55-year Reanalysis
MACC	Monitoring Atmospheric Composition and Climate project
MAR	Modèle Atmosphérique Régional regional climate model
MDCRS	Meteorological Data Collection and Reporting System
MERRA	Modern-Era Retrospective Analysis for Research and Applications
MERRA-2	Modern-Era Retrospective Analysis for Research and Applications, Version 2
Metop	Meteorological Operational Satellite
MHS	Microwave Humidity Sounder
MISR	Multi-angle SpectroRadiometer
MLS	Microwave Limb Sounder
MODIS	Moderate Resolution Imaging Spectroradiometer
MSG	Meteosat Second Generation satellite
MSU	Microwave Sounding Unit
MTSAT	Multifunctional Transport Satellite
NAAPS	Navy Aerosol Analysis and Prediction System
NASA	National Aeronautics and Space Administration
NCEP	National Centers for Environmental Prediction
NEXRAD	Next-Generation Radar
NOAA	National Oceanic and Atmospheric Administration
NRL	Naval Research Laboratory
OISST	Optimum Interpolation Sea Surface Temperature
OMI	Ozone Monitoring Instrument
OPAC	Optical Properties of Aerosols and Clouds
OSTIA	Operational Sea Surface Temperature and Sea Ice Analysis
PAOB	Synthetic surface pressure observation

Pibal	Pilot balloon
PIREP	Pilot report
QBO	Quasi-Biennial Oscillation
QFED	Quick Fire Emission Dataset
Raob	Radiosonde observation
RAS	Relaxed Arakawa-Schubert convection scheme
RMS	Root mean square
RSS	Remote Sensing Systems
SBUV	Solar Backscatter Ultraviolet Radiometer
SEVIRI	Spinning Enhanced Visible Infrared Imager
SHEBA	Surface Heat Budget of the Arctic Ocean
SIC	Sea ice concentration
SMAP	Soil Moisture Active Passive satellite
SMOS	Soil Moisture and Ocean Salinity satellite
SNPP	Suomi National Polar-orbiting Partnership
SSM/I	Special Sensor Microwave Imager
SSMIS	Special Sensor Microwave Imager/Sounder
SST	Sea surface temperature
SSU	Stratospheric Sounding Unit
TIROS	Television Infrared Observation Satellite
TLNMC	Tangent linear normal mode constraint
TMI	Tropical Rainfall Measuring Mission Microwave Imager
TOA	Top of the atmosphere
TOMS	Total Ozone Mapping Spectrometer
VAD	Velocity Azimuth Display
WMO	World Meteorological Organization

1299 References

- 1300 Adler, R. F., and Coauthors, 2003: The version-2 Global Precipitation Climatology
1301 Project (GPCP) monthly precipitation analysis (1979–present). *J. Hydrometeor.*,
1302 **4**, 1147–1167.
- 1303 Akella, S., R. Todling, M., and M. Suárez, 2016: Assimilation for skin SST in the NASA
1304 GEOS atmospheric data assimilation system. *Quart. J. Roy. Meteor. Soc.*,
1305 doi:10.1002/qj.2988.
- 1306 Andrews, D. G., J. R. Holton, and C. B. Leovy, 1987: Middle Atmosphere Dynamics.
1307 Academic Press, 489 pages.
- 1308 Bacmeister, J. T. and Stephens, G., 2011: Spatial statistics of likely convective clouds
1309 in CloudSat data. *J. Geophys. Res.*, **116**, D04104, doi:10.1029/2010JD014444.
- 1310 Ballish, B. A., and V. K. Kumar, 2008: Systematic differences in aircraft and radiosonde
1311 temperatures. *Bull. Amer. Meteor. Soc.*, **89**, 1689–1707.
- 1312 Bauer, P., A. J. Geer, P. Lopez, and D. Salmond, 2010: Direct 4D-Var assimilation of
1313 all-sky radiances. Part I: Implementation. *Quart. J. Roy. Meteor. Soc.*, **136**,
1314 1868–1885. doi:10.1002/qj.659
- 1315 Bellouin, N., J. Quaas, J.-J. Morcrette and O. Boucher, 2013: Estimates of aerosol
1316 radiative forcing from the MACC re-analysis. *Atmos. Chem. Phys.*, **13**, 2045–
1317 2062, doi:10.5194/acp-13-2045-2013.
- 1318 Berrisford, P., P. Kallberg, S. Kobayashi, D. Dee, S. Uppala, A. J. Simmons, P. Poli,
1319 and H. Sato, 2011: Atmospheric conservation properties in ERA-Interim. *Quart.*
1320 *J. Roy. Meteor. Soc.*, **137**, 1381–1399.
- 1321 Bloom, S., L. Takacs, A. DaSilva, and D. Ledvina, 1996: Data assimilation using incre-
1322 mental analysis updates. *Mon. Wea. Rev.*, **124**, 1256–1271.
- 1323 Bocquet M., and Coauthors, 2015:, Data assimilation in atmospheric chemistry models:
1324 Current and future prospects for coupled chemistry meteorology models. *Atmos.*
1325 *Chem. Phys.*, **15** (10), 5325–5358, doi:10.5194/acp-15-5325-2015.
- 1326 Bosilovich, M. G., 2013: Regional climate and variability in NASA MERRA and recent
1327 reanalyses: US summertime precipitation and temperature, *J. Appl. Meteor.*
1328 *Climatol.*, **52**, 1939–1951, doi: <http://dx.doi.org/10.1175/JAMC-D-12-0291.1>.
- 1329 Bosilovich, M.G., F. R. Robertson, and J. Chen, 2011: Global energy and water budgets

- 1330 in MERRA. *J. Climate*, **24**, 282–300.
- 1331 Bosilovich, M.G., and Coauthors, 2015: MERRA-2: Initial Evaluation of the Climate.
 1332 NASA/TM2015104606, Vol. **43**, 139 pp.
 1333 <https://gmao.gsfc.nasa.gov/pubs/docs/Bosilovich803.pdf>.
- 1334 Bosilovich, M., F. Robertson, L. Takacs, A. Molod, and D. Mocko, 2017: Atmospheric
 1335 water balance and variability in the MERRA-2 reanalysis. *J. Climate*, **30**, 1177–
 1336 1196, doi: 10.1175/JCLI-D-16-0338.1.
- 1337 Box, J. E., and A. Rinke, 2003: Evaluation of Greenland Ice Sheet surface climate in
 1338 the HIRHAM regional climate model using automatic weather station data. *J.*
 1339 *Climate*, **16**, 1302–1319, doi:10.1175/1520-0442-16.9.1302.
- 1340 Brassington, G. B., M. J. Martin, H. L. Tolman, S. Akella, M. Balmeseda, C. R. S. Cham-
 1341 bers, J. A. Cummings, Y. Drillet, P. A. E. M. Jansen, P. Laloyaux, D. Lea, A.
 1342 Mehra, I. Mirouze, H. Ritchie, G. Samson, P. A. Sandery, G. C. Smith, M. Suárez,
 1343 and R. Todling, 2015: Progress and challenges in short- to medium- range coupled
 1344 prediction, *J. Op. Oceanogr.*, **8**, 239–258, doi:10.1080/1755876X.2015.1049875.
- 1345 Buchard, V., and Coauthors, 2015: Using the OMI aerosol index and absorption aerosol
 1346 optical depth to evaluate the NASA MERRA Aerosol Reanalysis. *Atmos. Chem.*
 1347 *Phys.*, **15** (10), 5743–5760, 10.5194/acp-15-5743-2015.
- 1348 Buchard, V., C. A. Randles, A. M. da Silva, A. Darmanov, P. R. Colarco, R. Govin-
 1349 daraju, R. Ferrare, J. Hair, A. J. Beyersdorf, L. D. Ziemka, and H. Yu, 2017:
 1350 The MERRA-2 Aerosol Reanalysis, 1980–onward, Part 2: Evaluation and case
 1351 studies. *J. Climate*, in review.
- 1352 Cardinali, C., L. Isaksen, and E. Anderson, 2003: Use and impact of automated aircraft
 1353 data in a global 4DVAR data assimilation system. *Mon. Wea. Rev.*, **131**, 1865–
 1354 1877.
- 1355 Chen Y., F. Weng, Y. Han, and Q. Liu, 2008: Validation of the community radiative
 1356 transfer model (CRTM) by using CloudSat Data. *J. Geophys. Res.*, **113** (D8),
 1357 2156–2202.
- 1358 Chin, M., P. Ginoux, S. Kinne, O. Torres, B. N. Holben, B. N. Duncan, R. V. Martin,
 1359 J. A. Logan, A. Higurashi, and T. Nakajima, 2002: Tropospheric aerosol op-
 1360 tical thickness from the GOCART model and comparisons with satellite and
 1361 sun photometer measurements. *J. Atmos. Sci.*, **59**, 461–483, 10.1175/1520-
 1362 0469(2002)059<0461:TAOTFT>2.0.CO;2,
 1363 [http://dx.doi.org10.1175/1520-0469\(2002\)059<0461:TAOTFT>2.0.CO;2](http://dx.doi.org10.1175/1520-0469(2002)059<0461:TAOTFT>2.0.CO;2).

- 1364 Chýlek, P., and J. A. Coakley, 1974: Aerosol and climate. *Science*, **183**, 75–77.
- 1365 Colarco, P., A. da Silva, M. Chin, and T. Diehl, 2010: Online simulations of global
1366 aerosol distributions in the NASA GEOS-4 model and comparisons to satel-
1367 lite and ground-based aerosol optical depth. *J. Geophys. Res.*, **115** (D14207),
1368 10.1029/2009JD012820, <http://dx.doi.org/10.1029/2009JD012820>.
- 1369 Collow, A. B. M., M. G. Bosilovich, and R. D. Koster, 2016: Large scale influences on
1370 summertime extreme precipitation in the northeastern United States. To appear
1371 in *J. Hydromet.*, doi: 10.1175/JHM-D-16-0091.1.
- 1372 Collow, A. B. M., and M. A. Miller, 2016: The seasonal cycle of the radiation budget
1373 and cloud radiative effect in the Amazon rainforest of Brazil. *J. Climate*, doi:
1374 10.1175/JCLI-D-16-0089.1.
- 1375 Colony, R., I. Appel, and I. Rigor, 1992: Surface air temperature observations in the
1376 Arctic Basin. Tech. Memo. TM 1-92, 120 pp. Available from Applied Physics
1377 Laboratory, University of Washington, Seattle, WA 98195.
- 1378 Compo, G. P., and Coauthors, 2011: The Twentieth Century Reanalysis Project. *Quart.*
1379 *J. Roy. Meteor. Soc.*, **137**, 1–28, doi:10.1002/qj.776.
- 1380 Coy, L., K. Wargan, A. M. Molod, W. R. McCarty, and S. Pawson, 2016: Structure
1381 and dynamics of the quasi-biennial oscillation in MERRA-2. *J. Climate*, **29**,
1382 5339–5354, doi:10.1175/JCLI-D-15-0809.1.
- 1383 Cullather, R. I., and M. G. Bosilovich, 2012: The energy budget of the polar atmosphere
1384 in MERRA. *J. Climate*, **25**, 5–24, doi:10.1175/2011JCLI4138.1.
- 1385 Cullather, R.I., S.M.J. Nowicki, B. Zhao, and M. J. Suárez, 2014: Evaluation of the
1386 surface representation of the Greenland Ice Sheet in a general circulation model.
1387 *J. Climate*, **27**, 4835–4856, doi: 10.1175/JCLI-D-13-00635.1.
- 1388 Darmenov, Anton, and Arlindo da Silva, 2015. The Quick Fire Emissions Dataset
1389 (QFED): Documentation of versions 2.1, 2.2 and 2.4. NASA/TM2015104606,
1390 Vol. 38, 201 pp.
- 1391 Decker, M., M. A. Brunke, Z. Wang, K. Sakaguchi, X. Zeng, and M. G. Bosilovich, 2011:
1392 Evaluation of the reanalysis products from GSFC, NCEP, and ECMWF using flux
1393 tower observations. *J. Climate*, **24**, 221–249, doi:10.1175/JCLI-D-11-00004.1.
- 1394 Dee, D. P., and Coauthors, 2011: The ERA-Interim reanalysis: configuration and per-
1395 formance of the data assimilation system. *Q. J. R. Meteorol. Soc.*, **137**, 553–597,

doi:10.1002/qj.828.

Dee D. P., and A. M. da Silva, 2003: The choice of variable for atmospheric moisture analysis. *Mon. Weather Rev.*, **131**, 155–171.

Dee, D., and S. Uppala, 2009: Variational bias correction of satellite radiance data in the ERA-Interim reanalysis. *Quart. J. Roy. Meteor. Soc.*, **135**, 1830–1841.

Derber, J. C., and W.-S. Wu, 1998: The use of TOVS cloud-cleared radiances in the NCEP SSI analysis system. *Mon. Wea. Rev.*, **126**, 2287–2299.

Diehl, T., A. Heil, M. Chin, X. Pan, D. Streets, M. Schultz, and S. Kinne, 2012: Anthropogenic, biomass burning, and volcanic emissions of black carbon, organic carbon, and SO₂ from 1980 to 2010 for hindcast model experiments. *Atmos. Chem. Phys. Discuss.*, **12** (9), 24 895–24 954, 10.5194/acpd-12-24895-2012, <http://www.atmos-chem-phys-discuss.net/12/24895/2012/>.

Donlon, C.J., M. Martin, J. Stark, J. Roberts-Jones, E. Fiedler, and W. Wimmer, 2012: The Operational Sea Surface Temperature and Sea Ice Analysis (OSTIA) system. *Remote Sens. Environ.*, **116**, 140–158, doi:10.1016/j.rse.2010.10.017.

Draper, C., R. Reichle, and R. Koster, 2017: Assessment of the MERRA-2 land surface energy flux estimates. *J. Climate*, in review.

Duykerke, P., and S. de Roode, 2001: Surface energy balance and turbulence characteristics observed at the SHEBA Ice Camp during FIRE III. *J. Geophys. Res.*, **106**, 15313–15322, doi:10.1029/2000JD900537.

Farman, J., B. Gardiner, B., and J. Shanklin, 1985: Large losses of total ozone in Antarctica reveal seasonal ClO_x/NO_x interaction *Nature*, **315** (6016), 207–210, doi: 10.1038/315207a0.

Fettweis, X., 2007: Reconstruction of the 1979–2006 Greenland ice sheet surface mass balance using the regional climate model MAR. *The Cryosphere*, **1**, 21–40, doi:10.5194/tc-1-21-2007.

Flemming, J., A. Benedetti, A. Inness, R. Engelen, L. Jones, V. Huijnen, S. Remy, M. Parrington, M. Suttie, A. Bozzo, V.-H. Peuch, D. Akritidis, and E. Katragkou, 2017: The CAMS interim Reanalysis of Carbon Monoxide, Ozone and Aerosol for 2003–2015, *Atmos. Chem. Phys.*, **17**, 1945–1983, doi:10.5194/acp-17-1945-2017.

Froidevaux, L., and Coauthors, 2006: Early validation analyses of atmospheric profiles from EOS MLS on the Aura satellite. *IEEE Transactions on Geoscience and*

1428 Remote Sensing 44, no. 5, doi:10.1109/TGRS.2006.864366.

1429 Global Modeling and Assimilation Office (GMAO), 2015a: MERRA-2 inst1_2d_asm_Nx:
 1430 2d, 3-Hourly, Instantaneous, Single-Level, Assimilation, Single-Level Diagnostics
 1431 V5.12.4, Greenbelt, MD, USA, Goddard Earth Sciences Data and Information
 1432 Services Center (GES DISC), accessed June 2016, doi:10.5067/3Z173KIE2TPD.

1433 Global Modeling and Assimilation Office (GMAO), 2015b: MERRA-2 inst1_2d_int_Nx:
 1434 2d, 1-Hourly, Instantaneous, Single-Level, Assimilation, Vertically Integrated Di-
 1435 agnostics V5.12.4, Greenbelt, MD, USA, Goddard Earth Sciences Data and In-
 1436 formation Services Center (GES DISC), accessed June 2016,
 1437 doi:10.5067/G0U6NGQ3BLE0.

1438 Global Modeling and Assimilation Office (GMAO), 2015c: MERRA-2 inst3_3d_asm_Np:
 1439 3d, 3-Hourly, Instantaneous, Pressure-Level, Assimilation, Assimilated Meteo-
 1440 rological Fields, V5.12.4, Greenbelt, MD, USA: Goddard Space Flight Center
 1441 Distributed Active Archive Center (GSFC DAAC), accessed June 2016,
 1442 doi:10.5067/QBZ6MG944HW0.

1443 Global Modeling and Assimilation Office (GMAO), 2015d: MERRA-2 tavg1_2d_flux_Nx:
 1444 2d, 1-Hourly, Time-Averaged, Single-Level, Assimilation, Surface Flux Diagnos-
 1445 tics V5.12.4, Greenbelt, MD, USA, Goddard Earth Sciences Data and Information
 1446 Services Center (GES DISC), accessed June 2016, doi:10.5067/7MCPBJ41Y0K6.

1447 Global Modeling and Assimilation Office (GMAO), 2015e: MERRA-2 tavg1_2d_int_Nx:
 1448 2d, 1-Hourly, Time-Averaged, Single-Level, Assimilation, Vertically Integrated
 1449 Diagnostics V5.12.4, Greenbelt, MD, USA, Goddard Earth Sciences Data and
 1450 Information Services Center (GES DISC), accessed June 2016,
 1451 doi:10.5067/Q5GVUVUIVGO7.

1452 Global Modeling and Assimilation Office (GMAO), 2015f: MERRA-2 tavg1_2d_slv_Nx:
 1453 2d, 1-Hourly, Time-Averaged, Single-Level, Assimilation, Single-Level Diagnos-
 1454 tics V5.12.4, Greenbelt, MD, USA, Goddard Earth Sciences Data and Information
 1455 Services Center (GES DISC), accessed June 2016, doi:10.5067/VJAFPLI1CSIV.

1456 Global Modeling and Assimilation Office (GMAO), 2015g: MERRA-2 tavgM_2d_aer_Nx:
 1457 2d, Monthly mean, Time-averaged, Single-Level, Assimilation, Aerosol Diagnos-
 1458 tics V5.12.4, Greenbelt, MD, USA: Goddard Space Flight Center Distributed
 1459 Active Archive Center (GSFC DAAC), accessed June 2016,
 1460 doi:10.5067/FH9A0MLJPC7N.

1461 Global Modeling and Assimilation Office (GMAO), 2015h: MERRA-2 tavgM_2d_flux_Nx:
 1462 2d, Monthly mean, Time-Averaged, Single-Level, Assimilation, Surface Flux Di-

1463 agnostics V5.12.4, Greenbelt, MD, USA, Goddard Earth Sciences Data and In-
 1464 formation Services Center (GES DISC), accessed June 2016,
 1465 doi:10.5067/0JRLVL8YV2Y4.

1466 Global Modeling and Assimilation Office (GMAO), 2015i: MERRA-2 tavgM_2d_glc_Nx:
 1467 2d, Monthly mean, Land Ice Surface Diagnostics, V5.12.4, Greenbelt, MD, USA:
 1468 Goddard Space Flight Center Distributed Active Archive Center (GSFC DAAC),
 1469 accessed June 2015, doi:10.5067/5W8Q3I9WUFGX.

1470 Global Modeling and Assimilation Office (GMAO), 2015j: MERRA-2 tavgM_2d_lnd_Nx:
 1471 2d, Monthly mean, Land Surface Diagnostics, V5.12.4, Greenbelt, MD, USA:
 1472 Goddard Space Flight Center Distributed Active Archive Center (GSFC DAAC),
 1473 accessed June 2015, doi:10.5067/8S35XF81C28F.

1474 Global Modeling and Assimilation Office (GMAO), 2015k: MERRA-2 tavgM_2d_int_Nx:
 1475 2d, Monthly mean, Time-Averaged, Single-Level, Assimilation, Vertically Inte-
 1476 grated Diagnostics V5.12.4, Greenbelt, MD, USA, Goddard Earth Sciences Data
 1477 and Information Services Center (GES DISC), accessed June 2015,
 1478 doi:10.5067/FQPTQ4OJ22TL.

1479 Global Modeling and Assimilation Office (GMAO), 2015l: MERRA-2 tavgM_3d_qdt_Np:
 1480 3d, Monthly mean, Time-Averaged, Pressure-Level, Assimilation, Moist Tenden-
 1481 cies V5.12.4, Greenbelt, MD, USA, Goddard Earth Sciences Data and Informa-
 1482 tion Services Center (GES DISC), accessed June 2016,
 1483 doi:10.5067/2ZTU87V69ATP.

1484 Global Modeling and Assimilation Office (GMAO), 2015m: MERRA-2 tavgM_2d_slv_Nx:
 1485 2d, Monthly mean, Single-Level Diagnostics, V5.12.4, Greenbelt, MD, USA: God-
 1486 dard Space Flight Center Distributed Active Archive Center (GSFC DAAC),
 1487 accessed April 2015, doi:10.5067/AP1B0BA5PD2K.

1488 Global Modeling and Assimilation Office (GMAO), 2015n: MERRA-2 tavgM_3d_tdt_Np:
 1489 3d, Monthly mean, Time-Averaged, Pressure-Level, Assimilation, Temperature
 1490 Tendencies V5.12.4, Greenbelt, MD, USA, Goddard Earth Sciences Data and
 1491 Information Services Center (GES DISC), accessed June 2016,
 1492 doi:10.5067/VILT59HI2MOY.

1493 Gong, S. L., 2003: A parameterization of sea-salt aerosol source function for sub- and
 1494 super-micron particles. *Global Biogeochemical Cycles*, **17** (4),
 1495 doi:10.1029/2003GB002079.

1496 Greuell, W., and T. Konzelmman, 1994: Numerical modelling of the energy balance
 1497 and englacial temperature of the Greenland Ice Sheet. Calculations for the ETH-

- 1498 Camp location (West Greenland, 1155m a.s.l.). *Global Planet. Change*, **9**, 91–114,
1499 doi:10.1016/0921-8181(94)90010-8.
- 1500 Ham, Y.-G., S. Schubert, Y. Vikhliayev, and M. J. Suárez, 2014: An assessment of the
1501 ENSO forecast skill of GEOS-5 system. *Clim. Dynam.*, doi:10.1007/s00382-014-
1502 2063-2.
- 1503 Han, Y., P. van Delst, Q. Liu, F. Weng, B. Yan, R. Treadon, and J. Derber, 2006:
1504 JCSDA Community Radiative Transfer Model (CRTM)–Version 1. NOAA Tech.
1505 Rep. 122, 33 pp.
- 1506 Heidinger, A. K., C. Cao, and J. T. Sullivan, 2002: Using Moderate Resolution Imaging
1507 Spectrometer (MODIS) to calibrate Advanced Very High Resolution Radiometer
1508 reflectance channels. *J. Geophys. Res. Atmos.*, **107** (D23), 10.1029/2001JD002035,
1509 <http://dx.doi.org/10.1029/2001JD002035>.
- 1510 Hoch, S.W., 2005: Radiative flux divergence in the surface boundary layer. A study
1511 based on observations at Summit, Greenland. Ph.D. dissertation, Swiss Federal
1512 Institute of Technology (ETH), Zurich, 164 pp.
- 1513 Holben, B., and Coauthors, 1998: AERONET - A federated instrument network and
1514 data archive for aerosol characterization. *Remote Sens. Environ.*, **66** (1), 1–16,
1515 [http://dx.doi.org/10.1016/S0034-4257\(98\)00031-5](http://dx.doi.org/10.1016/S0034-4257(98)00031-5),
1516 <http://www.sciencedirect.com/science/article/pii/S0034425798000315>.
- 1517 Holm, E. V., 2003: Revision of the ECMWF humidity analysis: Construction of a
1518 Gaussian control variable. In *Proceedings of Workshop on Humidity Analysis*,
1519 1–3. ECMWF/GEWEX: Reading, UK.
- 1520 Inness, A., F. Baier, A. Benedetti, I. Bouarar, S. Chabrillat, H. Clark, H., and Coauthors,
1521 2013: The MACC reanalysis: An 8 yr data set of atmospheric composition.
1522 *Atmos. Chem. Phys.*, **13**, 4073–4109, doi:10.5194/acp-13-4073-2013.
- 1523 Kahn, R. A., B. J. Gaitley, J. V. Martonchik, D. J. Diner, K. A. Crean, and B. Holben,
1524 2005: Multiangle Imaging Spectroradiometer (MISR) global aerosol optical depth
1525 validation based on 2 years of coincident Aerosol Robotic Network (AERONET)
1526 observations. *J. Geophys. Res. Atmos.*, **110** (D10), 10.1029/2004JD004706,
1527 URL <http://dx.doi.org/10.1029/2004JD004706>.
- 1528 Kleist, D. T., D. F. Parrish, J. C. Derber, R. Treadon, R. M. Errico, and R. Yang, 2009a:
1529 Improving incremental balance in the GSI 3DVAR analysis system. *Mon. Wea.*
1530 *Rev.*, **137**, 1046–1060.

- 1531 Kleist D. T., D. F. Parrish, J. C. Derber, R. Treadon, W.-S. Wu, and S. Lord, 2009b:
1532 Introduction of the GSI into the NCEPs Global Data Assimilation System. *Wea.*
1533 *Forecasting*, **24**, 1691–1705.
- 1534 Kinne, S., and Coauthors, 2006:, An AeroCom initial assessment - optical properties in
1535 aerosol component modules of global models. *Atmos. Chem. Phys.*, **6**, 1815–
1536 1834, doi:10.5194/acp-6-1815-2006.
- 1537 Kobayashi, S., M. Matricardi, D. Dee, and S. Uppala, 2009: Toward a consistent reanal-
1538 ysis of the upper stratosphere based on radiance measurements from SSU and
1539 AMSU-A. *Quart. J. Roy. Meteor. Soc.*, **135**, 2086–2099, doi:10.1002/qj.514.
- 1540 Kobayashi, S., Y. Ota, Y. Harada, A. Ebita, M. Moriya, H. Onoda, K. Onogi, H.
1541 Kamahori, C. Kobayashi, H. Endo, K. Miyaoka, and K. Takahashi, 2015: The
1542 JRA-55 reanalysis: General specifications and basic characteristics. *J. Meteorol.*
1543 *Soc. Japan*, **93** (1), 5–48. doi:10.2151/jmsj.2015-001.
- 1544 Koster, R. D., G. Walker, G. J. Collatz, and P. E. Thornton, 2014: Hydroclimatic
1545 controls on the means and variability of vegetation phenology and carbon uptake.
1546 *J. Climate*, **27**, 5632–5652. doi: 10.1175/JCLI-D-13-00477.
- 1547 Kunkel, K. E., and Coauthors, 2013: Monitoring and understanding trends in ex-
1548 treme storms: State of knowledge. *Bull. Amer. Meteor. Soc.*, **94**, 499–514,
1549 doi:10.1175/BAMS-D-11-00262.1.
- 1550 Levy, R. C., L. A. Remer, S. Mattoo, E. F. Vermote, and Y. J. Kaufman, 2007:
1551 Second-generation operational algorithm: Retrieval of aerosol properties over land
1552 from inversion of Moderate Res-olution Imaging Spectroradiometer spectral re-
1553 flectance. *J. Geophys. Res. Atmos.*, **112** (D13), 10.1029/2006JD007811, URL
1554 <http://dx.doi.org/10.1029/2006JD007811>.
- 1555 Lim, Y.-K., R. Kovach, S. Pawson, and G. Vernieres, 2017: The 2015/2016 El Niño event
1556 in context of the MERRA-2 reanalysis: A comparison of the tropical Pacific with
1557 1982/1983 and 1997/1998. *J. Climate*, doi:10.1175/JCLI-D-16-0800.1, in press.
- 1558 Liu, Q. and S. Boukabara, 2014: Community Radiative Transfer Model (CRTM) ap-
1559 plications in supporting the Suomi National Polar-orbiting Partnership (SNPP)
1560 mission validation and verification. *Remote Sens. Environ.*, **140**, 744–754.
- 1561 Lynch, P., and Coauthors, 2016:, An 11-year global gridded aerosol optical thickness
1562 reanalysis (v1.0) for atmospheric and climate sciences. *Geosci. Model Dev.*, **9**,
1563 1489–1522, doi:10.5194/gmd-9-1489-2016.

- 1564 Lynch-Stieglitz, M., 1994: The development and validation of a simple snow model for
1565 the GISS GCM. *J. Climate*, **7**, 1842–1855,
1566 doi:10.1175/1520-0442(1994)007,1842:TDAVOA.2.0.CO;2.
- 1567 Manney, G. L., K. Kruger, S. Pawson, K. Minschwaner, M. J. Schwartz, W. H. Daffer,
1568 N. J. Livesey, M. G. Mlynczak, E. E. Remsberg, J. M. Russell, J.W. Waters,
1569 2008: The evolution of the stratopause during the 2006 major warming: Satellite
1570 data and assimilated meteorological analyses. *J. Geophys. Res.*, **113**, D11115,
1571 doi:10.1029/2007JD00909.
- 1572 Marticorena, B., and G. Bergametti, 1995: Modeling the atmospheric dust cycle: 1.
1573 Design of a soil-derived dust emission scheme. *J. Geophys. Res. Atmos.*, **100**
1574 (**D8**), 16415–16430, doi:10.1029/95JD00690.
- 1575 McCarty, W., L. Coy, R. Gelaro, A. Huang, D. Merkova, E. B. Smith, M. Sienkiewicz,
1576 and K. Wargan, 2016: MERRA-2 input observations: Summary and initial assess-
1577 ment. *NASA Technical Report Series on Global Modeling and Data Assimilation*,
1578 NASA/TM-2016-104606, Vol. **46**, 61 pp.
- 1579 McPeters, R., M. Kroon, G. Labow, E. Brinksma, D. Balis, I. Petropavlovskikh, J. P.
1580 Veefkind, P. K. Bhartia, and P. F. Levelt, 2008: Validation of the Aura Ozone
1581 Monitoring Instrument total column ozone product. *J. Geophys. Res.*, **113**,
1582 D15S14, doi:10.1029/2007JD008802.
- 1583 Meng, J., R. Yang, H. Wei, M. Ek, G. Gayno, P. Xie, and K. Mitchell, 2012: The
1584 Land Surface Analysis in the NCEP Climate Forecast System Reanalysis. *J.*
1585 *Hydrometeor.*, **13**, 1621–1630, doi: 10.1175/JHM-D-11-090.1.
- 1586 Mesinger, F., and Coauthors, 2006: North American Regional Reanalysis. *Bull. Amer.*
1587 *Meteor. Soc.*, **87**, 343–360, doi:10.1175/BAMS-87-3-343.
- 1588 Molina, M. J., and F. S. Rowland, 1974: Stratospheric sink for chlorouoromethanes:
1589 Chlorine atom-catalysed destruction of ozone. *Nature*, **249** (**28**), 810–812.
- 1590 Molod, A., L. Takacs, M. Suárez, and J. Bacmeister, 2015: Development of the GEOS-5
1591 atmospheric general circulation model: evolution from MERRA to MERRA2,
1592 *Geosci. Model Dev.*, **8**, 1339–1356, doi:10.5194/gmd-8-1339-2015.
- 1593 Moorthi, S., and M. J. Suárez, 1992: Relaxed Arakawa-Schubert: A parameterization of
1594 moist convection for general circulation models. *Mon. Wea. Rev.*, **120**, 978–1002.
- 1595 Newman, P. A., and E. R. Nash, 2005: The unusual southern hemisphere stratosphere
1596 winter of 2002. *J. Atmos. Sci.*, **62**, 614–628, doi: 10.1175/JAS-3323.1.

- 1597 Myhre, G., 2009:, Consistency between satellite-derived and modeled estimates of the
1598 Direct Aerosol Effect. *Science*, **325**, 187–190.
- 1599 Parrish, D. F., and J. C. Derber, 1992: The National Meteorological Center’s spectral
1600 statistical-interpolation analysis system. *Mon. Wea. Rev.*, **120**, 1747–1763.
1601 [http://dx.doi.org/10.1175/1520-0493\(1992\)120;1747:TnMCSS;2.0.CO;2](http://dx.doi.org/10.1175/1520-0493(1992)120;1747:TnMCSS;2.0.CO;2)
- 1602 Poli, P., and Coauthors, 2013: The data assimilation system and initial performance
1603 evaluation of the ECMWF pilot reanalysis of the 20th-century assimilating surface
1604 observations only (ERA-20C). ERA Report Series 14
- 1605 Putman, W. and S.-J. Lin, 2007: Finite Volume Transport on Various Cubed Sphere
1606 Grids. *J. Comput. Phys.*, **227**, 55–78. doi:10.1016/j.jcp.2007.07.022.
- 1607 Randles, C. A., A. M. da Silva, V. Buchard, A. Darmanov, P. R. Colarco, V. Aquila, H.
1608 Bian, E. P. Nowottnick, X. Pan, A. Smirnov, H. Yu, and R. Govindaraju, 2016:
1609 The MERRA-2 aerosol assimilation. *NASA Technical Report Series on Global*
1610 *Modeling and Data Assimilation*, NASA/TM-2016-104606, Vol. **45**, 143 pp.
- 1611 Randles, C. A., A. da Silva, V. Buchard, P.R. Colarco, A. Darmanov, R. Govindaraju,
1612 A. Smirnov, B. Holben, R. Ferrare, J. Hair, Y. Shinozuka, and C.J. Flynn, 2017:
1613 The MERRA-2 Aerosol Reanalysis, 1980–onward, Part 1: System description and
1614 data assimilation evaluation. *J. Climate*, in review.
- 1615 Reichle, R. H., R. D. Koster, G. J. M. De Lannoy, B. A. Forman, Q. Liu, S. Mahanama,
1616 and A. Toure, 2011: Assessment and enhancement of MERRA land surface hy-
1617 drology estimates. *J. Climate*, **24**, 6322–6338. doi:10.1175/JCLI-D-10-05033.1.
- 1618 Reichle, R. H., and Q. Liu, 2014: Observation-Corrected Precipitation Estimates in
1619 GEOS-5. NASA/TM2014-104606, Vol. 35.
- 1620 Reichle, R. H., C. S. Draper, Q. Liu, M. Girotto, S. P. P. Mahanama, R. D. Koster, and
1621 G. J. M. De Lannoy, 2017b: Assessment of MERRA-2 land surface hydrology
1622 estimates, *J. Climate*, doi:10.1175/JCLI-D-16-0720.1.
- 1623 Reichle, R. H., Q. Liu, R. D. Koster, C. S. Draper, S. P. P. Mahanama, and G. S.
1624 Partyka, 2017a: Land surface precipitation in MERRA-2, *J. Climate*, **30**, 1643–
1625 1664, doi:10.1175/JCLI-D-16-0570.1.
- 1626 Remer, L. A., and Coauthors, 2005: The MODIS aerosol algorithm, products, and
1627 validation. *J. Atmos. Sci.*, **62**, 947–973, 10.1175/JAS3385.1, [http://dx.doi.org/](http://dx.doi.org/10.1175/JAS3385.1)
1628 [10.1175/JAS3385.1](http://dx.doi.org/10.1175/JAS3385.1).

- Reynolds, R. W., N. A. Rayner, T. M. Smith, D. C. Stokes, and W. Wang, 2002: An improved in situ and satellite SST analysis for climate. *J. Climate*, **15**, 1609–1625.
- Reynolds, R. W., T. M. Smith, C. Liu, D. B. Chelton, K. S. Casey, and M. G. Schlax, 2007: Daily high-resolution-blended analyses for sea surface temperature. *J. Climate*, **20**, 5473–5496, doi:10.1175/2007JCLI1824.1.
- Rienecker, M. M., and Coauthors, 2008: The GEOS-5 Data Assimilation System—Documentation of versions 5.0.1 and 5.1.0, and 5.2.0. *NASA Technical Report Series on Global Modeling and Data Assimilation*, NASA/TM-2008-104606, Vol. **27**, 118 pp.
<https://gmao.gsfc.nasa.gov/pubs/docs/Rienecker369.pdf>.
- Rienecker and Coauthors, 2011: MERRA - NASA’s Modern-Era Retrospective Analysis for Research and Applications. *J. Climate*, **24**, 3624–3648, doi:10.1175/JCLI-D-11-00015.1.
- Robertson, F. R., M. G. Bosilovich, J. Chen, and T. L. Miller, 2011: The effect of satellite observing system changes on MERRA water and energy fluxes. *J. Climate*, **24**, 5197–5217. doi: <http://dx.doi.org/10.1175/2011JCLI4227.1>.
- Saha, S., and Coauthors, 2010: The NCEP Climate Forecast System Reanalysis. *Bull. Amer. Meteor. Soc.*, **91**, 1010–1057, doi:10.1175/2010BAMS3001.1.
- Schubert, S. D., R. Rood, and J. Pfaendtnr, 1993: An assimilated dataset for earth science applications. *Bull. Amer. Meteor. Soc.*, **74**, 2331–2342, doi:10.1175/1520-0477(1993)0742.0.CO;2.
- Schultz, M. G., A. Heil, J. J. Hoelzemann, A. Spessa, K. Thonicke, J. Goldammer, A. C. Held, J. M. Pereira, and M. van het Bolscher, 2008: Global Wildland Fire Emissions from 1960 to 2000. *Global Biogeochem. Cyc.*, **22**, GB2002, doi:10.1029/2007GB003031.
- Schwartz, M.J., and Coauthors, 2008: Validation of the Aura Microwave Limb Sounder temperature and geopotential height measurements. *J. Geophys. Res.* **113**, D15S11, doi:10.1029/2007JD008783.
- Segal-Rosenhemier, M., N. Barton, J. Redmann, S. Schmidt, S. LeBlanc, B. Anderson, E. Winstead, C. Corr, R. Moore, L.K. Thornhill, and R.I. Cullather., 2017: Improving our understanding of surface radiative flux bias in Arctic reanalysis over the marginal ice zone: Observational based sensitivity analysis during ARISE. *J. Clim.*, in review.

- 1662 Seidel, D. J., J. Li, C. Mears, I. Moradi, J. Nash, W. J. Randel, R. Saunders, D. W. J.
1663 Thompson, and C.-Z. Zou, 2016: Stratospheric temperature changes during the
1664 satellite era. *J. Geophys. Res. Atmos.*, **121**, doi:10.1002/2015JD024039.
- 1665 Simmons, A. J., P. Berrisford, D. P. Dee, H. Hersbach, S. Hirahara, and J.-N. Thpaut,
1666 2016: A reassessment of temperature variations and trends from global reanalyses
1667 and monthly surface climatological datasets. *Quart. J. Roy. Meteor. Soc.*,
1668 doi10.1002/qj.2949.
- 1669 Simmons, A. J., P. Poli, D. P. Dee, P. Berrisford, H. Hersbach, S. Kobayashi, and
1670 C. Peubey, 2014: Estimating low-frequency variability and trends in atmospheric
1671 temperature using ERA-Interim. *Q. J. R. Meteorol. Soc.*, **140**, 329–353, doi:10.1002/qj.2317.
- 1672 Stieglitz, M., A. Ducharne, R. D. Koster, and M. J. Suárez, 2001: The impact of de-
1673 tailed snow physics on the simulation of snow cover and subsurface thermody-
1674 namics at continental scales. *J. Hydrometeor.*, **2**, 228–242, doi:10.1175/1525-
1675 7541(2001)002,0228:TIODSP.2.0.CO;2.
- 1676 Susskind, J., J. Rosenfield, and D. Reuter, 1983: An accurate radiative transfer model
1677 for use in the direct physical inversion of HIRS and MSU temperature sounding
1678 data. *J. Geophys. Res.*, **88**, 8550–8568.
- 1679 Takacs, L. L., M. J. Suárez, and R. Todling, 2016: Maintaining atmospheric mass and
1680 water balance in reanalyses. *Quart. J. Roy. Meteor. Soc.*, **142** 1565–1573. doi:
1681 10.1002/qj.2763.
- 1682 Taylor, K. E., D. Williamson, and F. Zwiers, 2000: The sea surface temperature and
1683 sea ice concentration boundary conditions for AMIP II simulations. Program for
1684 Climate Model Diagnosis and Intercomparison (PCMDI). Report 60, Lawrence
1685 Livermore National Laboratory.
- 1686 Trenberth, K.E., and L. Smith, 2005: The mass of the atmosphere: A constraint on
1687 global analysis. *J. Climate*, **18**, 864–875.
- 1688 Turner, J., S. Colwell, G. Marshall, T. Lachlan-Cope, A. Carleton, P. Jones, V. Lagun,
1689 P. Reid, and S. Iagovkina, 2004: The SCAR READER Project: Toward a High-
1690 Quality Database of Mean Antarctic Meteorological Observations. *J. Climate*,
1691 **17**, 2890–2898, doi:10.1175/1520-0442(2004)017<2890:TSRPTA>2.0.CO;2.
- 1692 van der Werf, G. R., J. Y. Randerson, L. Giglio, G. J. Collatz, P. S. Kasibhatla, and A.
1693 F. Arellano Jr., 2006: Interannual variability in global biomass burning emissions
1694 from 1997 to 2004. *Atmos. Chem. Phys.*, **6**, 3423–3441, doi:10.5194/acp-6-3423-
1695 2006.

- 1696 Wargan, K., and L. Coy, 2016: Strengthening of the Tropopause Inversion Layer during
1697 the 2009 Sudden Stratospheric Warming: A MERRA-2 Study. *J. Atmos. Sci.*,
1698 **73**, 1871–1887, doi: 10.1175/JAS-D-15-0333.1
- 1699 Wargan, K., G. Labow, S. Frith, S. Pawson, and G. Partyka, 2017: Evaluation of the
1700 ozone fields in NASAs MERRA-2 reanalysis. *J. Climate*, doi: 10.1175/JCLI-D-
1701 16-0699.1.
- 1702 Wargan, K., S. Pawson, M. A. Olsen, J. C. Witte, A. R. Douglass, J. R. Ziemke, S. E.
1703 Strahan, and J. E. Nielsen, 2015: The global structure of upper troposphere-lower
1704 stratosphere ozone in GEOS-5: A multiyear assimilation of EOS Aura data, *J.*
1705 *Geophys. Res. Atmos.*, **120**, 2013–2036, doi:10.1002/2014JD022493.
- 1706 World Meteorological Organization (WMO 2014): Scientific Assessment of Ozone De-
1707pletion: 2014. Global Ozone Research and Monitoring Project - Report no. 55.
- 1708 Wu, W.-S., R. J. Purser, and D. F. Parrish, 2002: Three-dimensional variational analysis
1709 with spatially inhomogeneous covariances. *Mon. Wea. Rev.*, **130**, 2905–2916.
- 1710 Xie, P., A. Yatagai, M. Chen, T. Hayasaka, Y. Fukushima, C. Liu, and S. Yang, 2007:
1711 A gauge-based analysis of daily precipitation over East Asia. *J. Hydrometeorol.*,
1712 **8**, 607–626.
- 1713 Yu, H., and Coauthors, 2006: A review of measurement-based assessments of the
1714 aerosol direct radiative effect and forcing. *Atmos. Chem. Phys.*, **6**, 613–666,
1715 doi:10.5194/acp-6-613-2006.

Table 1: Observation types assimilated in MERRA-2, including their usage dates and sources. Bold fonts indicate observation types not assimilated in MERRA. Acronyms are defined in the Appendix.

Data Type	MERRA-2 Dates	Source
<i>Conventional</i>		
Raob, Pibal, Dropsonde	1 Jan 1980–present	See Rienecker et al. (2011)
AIREP, PIREP, ASDAR, MDCRS aircraft	1 Jan 1980–present	NCEP, ECMWF, JMA
PAOB	1 Jan 1980–17 Aug 2010	BOM
Surface land	1 Jan 1980–present	NCEP
Surface ship and buoy	1 Jan 1980–present	ICOADS
<i>Ground-Based Remotely Sensed</i>		
Wind profiler	14 May 1992–present	UCAR, NCEP
NEXRAD VAD wind	16 June 1997–present	NCEP
<i>Satellite-Derived Wind</i>		
GMS, MTSAT, Himawari atmos. motion vector	1 Jan 1980–present	NCEP, JMA
Meteosat atmos. motion vector	1 Jan 1980–present	NCEP, EUMETSAT
GOES atmos. motion vector	1 Jan 1980–present	NCEP
AVHRR atmos. motion vector	1 Oct 1982–present	CIMSS
SSM/I surface wind speed	9 Jul 1987–4 Nov 2009	RSS
ERS-1 surface wind vector	5 Aug 1991–21 May 1996	ESA
ERS-2 surface wind vector	19 Mar 1996–29 Mar 2011	ESA
QuikSCAT surface wind vector	19 Jul 1999–22 Nov 2009	JPL
MODIS atmos. motion vector	2 Jul 2002–present	CIMSS, NCEP
SSMIS surface wind speed	23 Oct 2003–29 Oct 2013	RSS
WindSat surface wind vector	13 Aug 2007–4 Aug 2012	NCEP
ASCAT surface wind vector	15 Sep 2008–present	NCEP
<i>Satellite-Retrieved</i>		
SBUV, SBUV/2 ozone	1 Jan 1980–31 Sep 2004	NASA/GES DISC
SSM/I rain rate	9 Jul 1987–16 Sep 2009	NASA/GES DISC
TMI rain rate	1 Jan 1998–8 Apr 2015	NASA/GES DISC
MLS temperature	13 Aug 2004–present	NASA/GES DISC
MLS ozone	1 Oct 2004–present	NASA/GES DISC
OMI total column ozone	1 Oct 2004–present	NASA/GES DISC
<i>Radio Occultation</i>		
GPSRO bending angle	14 July 2004–present	NCAR, NCEP
<i>Satellite Radiance</i>		
TOVS	1 Jan 1980–10 Oct 2006	NCAR, NESDIS
SSM/I	9 Jul 1987–4 Nov 2009	RSS
ATOVS (NOAA-15, -16, -17, -18)	21 Jul 1998–present	NESDIS
GOES (G08, G10, G11, G12 Low Res.)	24 April 2001–31 March 2007	NCEP, NESDIS
AMSU-A (Aqua)	1 Sep 2002–present	NASA/GES DISC
AIRS	1 Sep 2002–present	NASA/GES DISC
GOES (G11, G12, G13, G15 Full Res.)	1 April 2007–present	NESDIS
ATOVS (NOAA-19, Metop-A, -B)	21 May 2007–present	NESDIS
IASI	17 Sep 2008–present	NESDIS
ATMS	16 Nov 2011–present	NESDIS
SEVIRI	15 Feb 2012–present	NESDIS
CrIS	7 Apr 2012–present	NESDIS

Table 2: Nominal channel selections for satellite radiances assimilated in MERRA-2. Usage can vary for individual satellite platforms as a result of sensor failure or quality control decisions.

Sensor	Assimilated Channels
MSU	2–4
AMSU-A	4–14
ATMS	5–15, 17–22
AMSU-B	1–5
MHS	1–5
SSM/I	1–7
SSU	1–3
HIRS	2–8, 10–12
AIRS	See McCarty et al. 2016
IASI	See McCarty et al. 2016
CrIS	See McCarty et al. 2016
GOES Sounder	1–8, 10–12
SEVIRI	2, 3

Table 3: Sea surface temperature and sea ice concentration data products used in MERRA-2.

MERRA-2 dates	SST and SIC product
1 January 1980 – 31 December 1981	CMIP mid-monthly 1°
1 January 1982 – 31 December 2002	NOAA OISST daily 1/4° (AVHRR)
1 January 2003 – 31 March 2006	NOAA OISST daily 1/4° (AVHRR, AMSR-E)
1 April 2006 – present	OSTIA daily 1/20°

Table 4: Clear-sky Direct Radiative Effect (DRE) from Reanalyses and Observations

	Yu et al. (2006) Obs. ^a	Yu et al. (2006) Models ^b	MERRA-2 ^c	MERRAero ^c	MACC ^d
<i>Land-area Average</i>					
AOD	0.225 ± 0.038	0.178 ± 0.029	0.180 ± 0.027	0.171 ± 0.030	0.203 ± 0.030
AAOD	–	–	0.012 ± 0.002	0.016 ± 0.003	0.010 ± 0.003
TOA DRE	-4.85 ± 0.45	-2.80 ± 1.19	-3.09 ± 0.62	-3.11 ± 0.70	-6.40 ± 1.00
SFC DRE	-11.70 ± 1.20	-7.20 ± 1.86	-8.35 ± 1.82	-8.64 ± 2.04	-11.50 ± 1.90
ATM DRE	6.85 ± 0.75	4.90 ± 0.81	5.26 ± 1.23	5.53 ± 1.37	5.10
<i>Ocean-area Average</i>					
AOD	0.138 ± 0.024	0.100 ± 0.042	0.123 ± 0.008	0.111 ± 0.010	0.170 ± 0.030
AAOD	–	–	0.005 ± 0.001	0.005 ± 0.001	0.007 ± 0.001
TOA DRE	-5.45 ± 0.70	-3.50 ± 1.28	-3.65 ± 0.21	-3.44 ± 0.24	-7.70 ± 1.50
SFC DRE	-8.80 ± 1.65	-4.80 ± 1.60	-5.74 ± 0.41	-5.58 ± 0.47	-10.60 ± 1.90
ATM DRE	3.60 ± 1.30	1.30 ± 0.72	2.09 ± 0.27	2.14 ± 0.29	2.90

^aMedian and standard deviation from satellite-derived estimates in Yu et al. (2006).

^bMedian and standard deviation from 4 global models in Yu et al. (2006).

^cClimatological global area-weighted average (\pm monthly standard deviation) for Y2003–Y2010.

^dFor MACC, the Y2003–Y2010 global mean and uncertainty is given following Bellouin et al. (2013).

1716 List of Figures

1717	1	Observations assimilated per 6-hr cycle in (a) MERRA and (b) MERRA-	
1718		2. The temporary spike in the number of surface wind observations assim-	
1719		ilated in MERRA-2 in late 2000 is due to an error in the pre-processing	
1720		of QuikSCAT data.	78
1721	2	Globally integrated monthly-mean mass anomalies from the mean sea-	
1722		sonal cycle for (a) MERRA and (b) MERRA-2. Shown are the anoma-	
1723		lies of total mass (black dotted), and their decomposition into atmo-	
1724		spheric water (blue) and dry air (orange). The units are hPa. Results	
1725		for MERRA-2 are derived from the data collection described in GMAO	
1726		(2015b).	79
1727	3	Globally integrated monthly-mean total water budget terms for (a) MERRA	
1728		and (b) MERRA-2. Shown are the water source term ($E - P$, blue), verti-	
1729		cally integrated analysis increment of water (green), and atmospheric wa-	
1730		ter storage (black dotted). The units are mm day^{-1} . Results for MERRA-	
1731		2 are derived from the data collections described in GMAO (2015b, d, e).	80
1732	4	Mean difference (1980–2015) between the (corrected) MERRA-2 precip-	
1733		itation seen by the land surface and the model-generated precipitation	
1734		within the MERRA-2 system. The units are mm d^{-1} . Results are de-	
1735		derived from the data collections described in GMAO (2015h, j).	81
1736	5	Time series of 12-month running mean prescribed sea surface temperature	
1737		for various reanalyses, averaged between 60°N and 60°S . The units are K.	
1738		Results for MERRA-2 are derived from the data collection described in	
1739		GMAO (2015f).	82
1740	6	Monthly mean (thick lines) and RMS (thin lines) background depar-	
1741		tures for surface pressure observations assimilated in MERRA (blue) and	
1742		MERRA-2 (red). Results are shown for the (a) Northern Hemisphere	
1743		and (b) Southern Hemisphere. The units are hPa. Also shown are the	
1744		corresponding monthly mean counts of surface pressure observations as-	
1745		similated in MERRA-2 (gray shaded).	83

1746	7	Global monthly mean (thick lines) and RMS (thin lines) background departures for radiosonde temperature observations assimilated in MERRA (blue) and MERRA-2 (red). Results are shown for the pressure levels (a) 10 hPa, (b) 50 hPa, (c) 300 hPa and (d) 700 hPa. The units are K. Also shown are the corresponding monthly mean counts of radiosonde temperature observations assimilated in MERRA-2 (gray shaded).	84
1747			
1748			
1749			
1750			
1751			
1752	8	As in Figure 7, except for radiosonde specific humidity observations in the tropics (20°N–20°S) at (a) 500 hPa and (b) 850 hPa. The units are g kg ⁻¹	85
1753			
1754			
1755	9	(a) Mean and (b) standard deviation of the monthly mean analysis tendency of surface pressure for the period January 1980 through December 2015. Monthly mean values are based on four synoptic times daily. The units are hPa day ⁻¹ . Results are derived from the data collection described in GMAO (2015k).	86
1756			
1757			
1758			
1759			
1760	10	Global (a) mean and (b) standard deviation of the monthly mean analysis tendency of temperature from 1000 to 70 hPa. Monthly means values are based on four synoptic times daily. The units are K day ⁻¹ . Results are derived from the data collection described in GMAO (2015n).	87
1761			
1762			
1763			
1764	11	As in Figure 10, except for specific humidity in the tropics (20°N–20°S) from 1000 to 250 hPa. The units are g kg ⁻¹ day ⁻¹ . Results are derived from the data collection described in GMAO (2015l).	88
1765			
1766			
1767	12	Probability distribution functions (PDFs) of observation minus forecast (O-F, dashed) and observation minus analysis (O-A, solid) differences in observation space, collocated in space and time for each sensor in the MERRA-2 aerosol observing system. The PDFs are calculated from innovation data in log-transformed space ($\ln(\text{AOD}+0.01)$) to ensure distributions are positive and Gaussian. The time periods considered include AVHRR (1993–1999), MODIS Terra (2001–2014), MODIS Aqua (2003–2014), MISR (2001–2012), and AERONET (ANET 2000–2013).	89
1768			
1769			
1770			
1771			
1772			
1773			
1774			
1775	13	Time series of area-weighted aerosol optical depth (AOD) from the MERRA-2 aerosol reanalysis averaged over major aerosol source regions: (a) South and East Asia [5°N–55°N, 65°W–160°W], (b) northern Africa [2.5°S–30°N, 45°W–15°E], and (c) the Amazon Basin in South America [20°S–7.5°N, 80°W–30°W]. The total AOD (thick black line) is the sum of contributions from sea salt (blue), dust (yellow), carbonaceous (black and organic carbon, green), and sulfate (grey) AOD. Results are derived from the data collection described in GMAO (2015g).	90
1776			
1777			
1778			
1779			
1780			
1781			
1782			

1783	14	Aerosol optical depth (AOD) from aerosol reanalyses (MERRA-2, MERRAero, NAAPS, MACC), inter-model comparisons (AeroCom Phase I, Yu_Model), and observations (Yu_Obs) for the period 2003–2010. Where available, total AOD is broken down by component species (left bar) and by fine and coarse mode (right bar). For MERRA-2 and MERRAero, the error bar represents the standard deviation of the monthly-mean AOD for the period 2003–2010. For MACC, the error bar is the uncertainty in the total AOD from Bellouin et al. (2013). AeroCom (Kinne et al., 2006) and Yu et al. (2006) uncertainty are the inter-model or inter-observational standard deviations. Coarse mode is defined as the sum of dust plus sea salt AOD, with the remainder of the AOD assigned to the fine mode. Results for MERRA-2 are derived from the data collection described in GMAO (2015g).	91
1784			
1785			
1786			
1787			
1788			
1789			
1790			
1791			
1792			
1793			
1794			
1795			
1796	15	Time series of 12-month running mean globally averaged precipitation for several reanalyses and the GPCP merged gauge satellite data product. The units are mm day ⁻¹ . Results for MERRA-2 are derived from the data collection described in GMAO (2015h).	92
1797			
1798			
1799			
1800	16	Time-averaged precipitation differences during June-July-August for (a) MERRA minus GPCP and (b) MERRA-2 minus GPCP for the period 1980–2015. The units are mm day ⁻¹ . Results for MERRA-2 are derived from the data collection described in GMAO (2015h).	93
1801			
1802			
1803			
1804	17	Time series of midwestern US summer seasonal precipitation anomalies, following Bosilovich (2013). The anomalies are computed from the June-July-August mean for the period 1980–2011. The gauge data are from NOAA/CPC gridded daily data for the US (Xie et al. 2007). The units are mm day ⁻¹ . Results for MERRA-2 are derived from the data collection described in GMAO (2015h).	94
1805			
1806			
1807			
1808			
1809			
1810	18	Regional summary statistics for the US summer seasonal anomaly time series of precipitation: (a) mean (mm day ⁻¹), (b) standard deviation (mm day ⁻¹), and (c) anomaly correlation to CPC gauge observations. The anomalies are computed from the June-July-August mean for the period 1980–2011. The regions lie within the continental US and are defined as in Bosilovich (2013): Northeast (NE), Southeast (SE), Midwest (MW), Great Plains (GP), Southern Great Plains (SGP), Northern Great Plains (NGP), Northwest (NW), Southwest (SW), and the accumulation of all area in these regions (US). Results for MERRA-2 are derived from the data collection described in GMAO (2015h).	95
1811			
1812			
1813			
1814			
1815			
1816			
1817			
1818			
1819			

1820	19	Average amount of precipitation that exceeds the 99th percentile during June-July-August for the period 1980–2013 for (a) MERRA, (b) MERRA-2, and (c) CPC gauge observations. Panel (d) shows the closeness of each reanalysis to the CPC observations for the same period, defined as $ \text{MERRA-2} - \text{CPC} - \text{MERRA} - \text{CPC} $, where the vertical bars indicate absolute differences and the names indicate the set of time-averaged grid-point values for each data type. In (d), blue (red) shades indicate that MERRA-2 (MERRA) is closer to the CPC observations. The units in all panels are mm day^{-1} . Results for MERRA-2 are derived from the data collection described in GMAO (2015d).	96
1830	20	Ertel’s potential vorticity (EPV, $\times 10^3$ potential vorticity units, PVU; $1 \text{ PVU} = 10^{-6} \text{m}^{-2} \text{s}^{-1} \text{K kg}^{-1}$) at 0.7 hPa on 2 January 1995 12 UTC for (a) MERRA and (b) MERRA-2 for the Northern Hemisphere. Polar cap detail (80° – 90°N) for (c) MERRA and (d) MERRA-2. Color shading interval is 2.5×10^3 PVU. Black contour interval is 10×10^3 PVU in (a) and (b) and 5×10^3 PVU in (c) and (d). Cyan circle denotes 80°N latitude. Results are derived from the data collection described in GMAO (2015c).	97
1837	21	Time-altitude section of zonally averaged temperature at 70°N for (a) MERRA and (b) MERRA-2. The time resolution is twice daily (00 and 12 UTC) for December 2005–March 2006. The contour interval is 5 K.	98
1840	22	Monthly and globally averaged temperature anomaly for MERRA-2 as a function of time. The annual cycle and mean for 1980–2015 have been removed. The MLS temperatures were introduced at levels above 5 hPa beginning in August 2004. Results are derived from the data collection described in GMAO (2015c).	99
1845	23	Time series of (a) total ozone (Dobson units, DU) at the South Pole derived from individual ozonesonde measurements (gray) and from collocated values in MERRA (blue) and MERRA-2 (red). Note that ozonesonde measurements are unavailable prior to 1986; see text for details. The reanalysis-minus-ozonesonde differences divided by sonde total ozone are shown in (b) for MERRA (blue) and MERRA-2 (red). The black vertical line in (b) separates the SBUV and Aura periods. (Figure from Wargan et al. 2016.) Results for MERRA-2 are derived from the data collection described in GMAO (2015a).	100

1854	24	Time series of the Antarctic ozone hole area calculated from MERRA-2	
1855		ozone fields averaged between 20 September and 10 October for the years	
1856		1980–2015 (red curve with circles). Also shown are values derived from	
1857		TOMS (gray squares) and OMI (black triangles) observations. The units	
1858		are 10^6 km^2 . Results for MERRA-2 in 1994 are excluded due to insuf-	
1859		ficient SBUV data coverage in the Southern Hemisphere, which signifi-	
1860		cantly degraded the analysis; see text for details. Results for MERRA-2	
1861		are derived from the data collection described in GMAO (2015a).	101
1862	25	Average annual cycle of 2-m air temperature in MERRA and MERRA-2	
1863		at (a) South Pole station (90°S ; 1980–2014; Turner et al., 2004), (b) Gill	
1864		automatic weather station (80°S , 179°W ; 1985–2014; Turner et al., 2004),	
1865		and (c) Summit, Greenland (73°N , 38°W ; 2000–2002; Hoch, 2005). The	
1866		units are $^\circ\text{C}$. Vertical bars denote ± 1 standard deviation of the multi-year	
1867		time series for each month. Results for MERRA-2 are derived from the	
1868		data collections described in GMAO (2015i, j, m).	102
1869	26	Surface mass balance for the Greenland Ice Sheet for the period 1980–2012	
1870		in (a) MERRA, (b) MERRA-2, and (c) MAR regional climate model (Fet-	
1871		twais 2007). The units are mm yr^{-1} water-equivalent. Surface topography	
1872		(including ice sheet) is contoured with dashed lines every 200 m. Results	
1873		for MERRA-2 are derived from the data collections described in GMAO	
1874		(2015i, j, m).	103

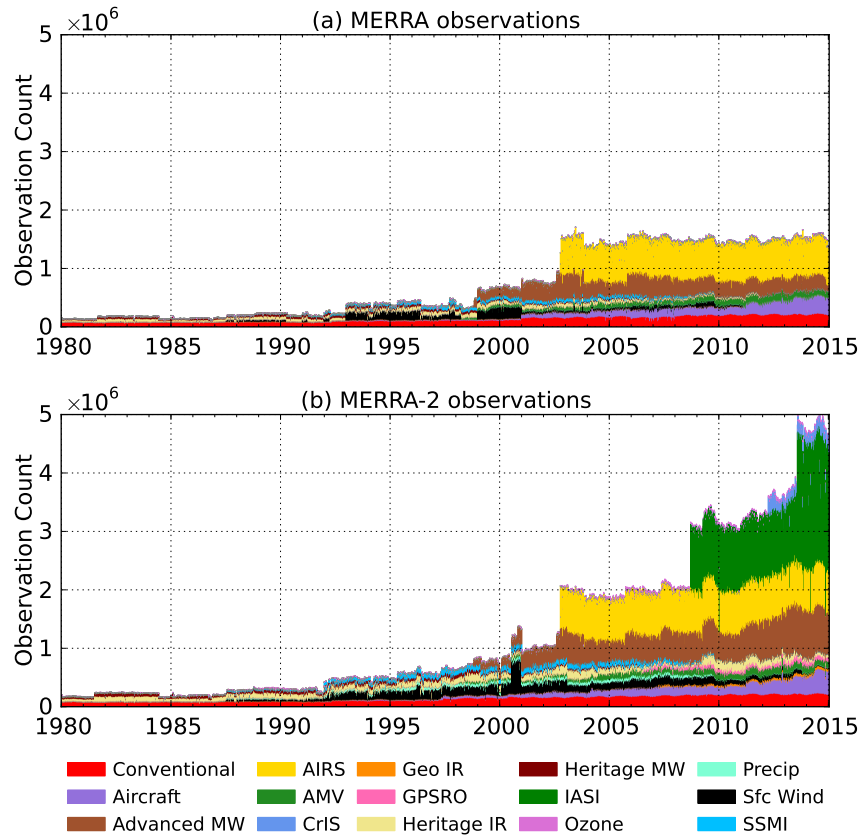


Figure 1: Observations assimilated per 6-hr cycle in (a) MERRA and (b) MERRA-2. The temporary spike in the number of surface wind observations assimilated in MERRA-2 in late 2000 is due to an error in the pre-processing of QuikSCAT data.

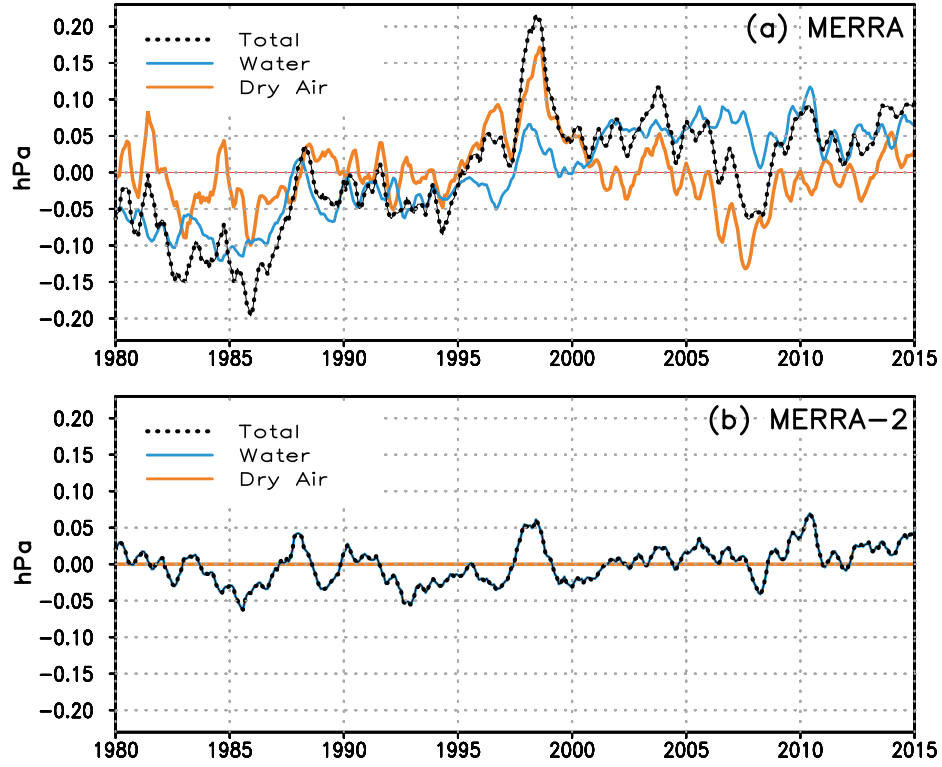


Figure 2: Globally integrated monthly-mean mass anomalies from the mean seasonal cycle for (a) MERRA and (b) MERRA-2. Shown are the anomalies of total mass (black dotted), and their decomposition into atmospheric water (blue) and dry air (orange). The units are hPa. Results for MERRA-2 are derived from the data collection described in GMAO (2015b).

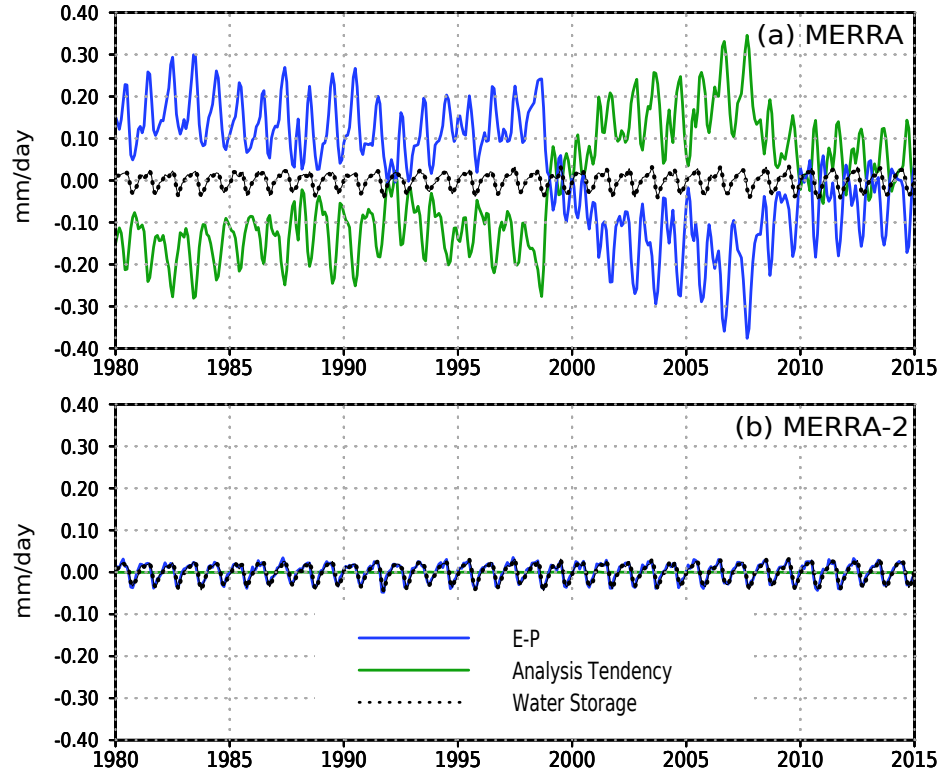


Figure 3: Globally integrated monthly-mean total water budget terms for (a) MERRA and (b) MERRA-2. Shown are the water source term ($E - P$, blue), vertically integrated analysis increment of water (green), and atmospheric water storage (black dotted). The units are mm day^{-1} . Results for MERRA-2 are derived from the data collections described in GMAO (2015b, d, e).

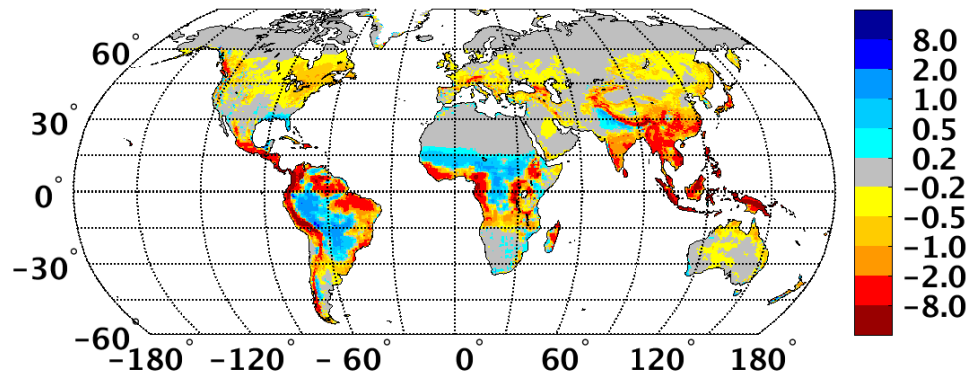


Figure 4: Mean difference (1980–2015) between the (corrected) MERRA-2 precipitation seen by the land surface and the model-generated precipitation within the MERRA-2 system. The units are mm d^{-1} . Results are derived from the data collections described in GMAO (2015h, j).

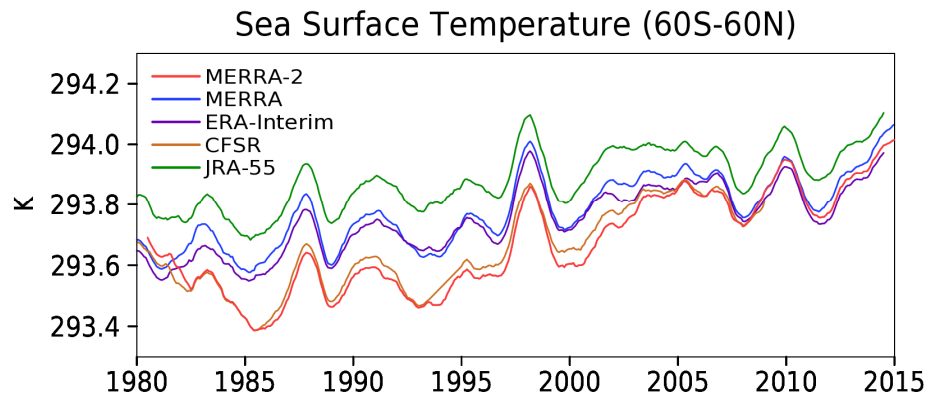


Figure 5: Time series of 12-month running mean prescribed sea surface temperature for various reanalyses, averaged between 60°N and 60°S. The units are K. Results for MERRA-2 are derived from the data collection described in GMAO (2015f).

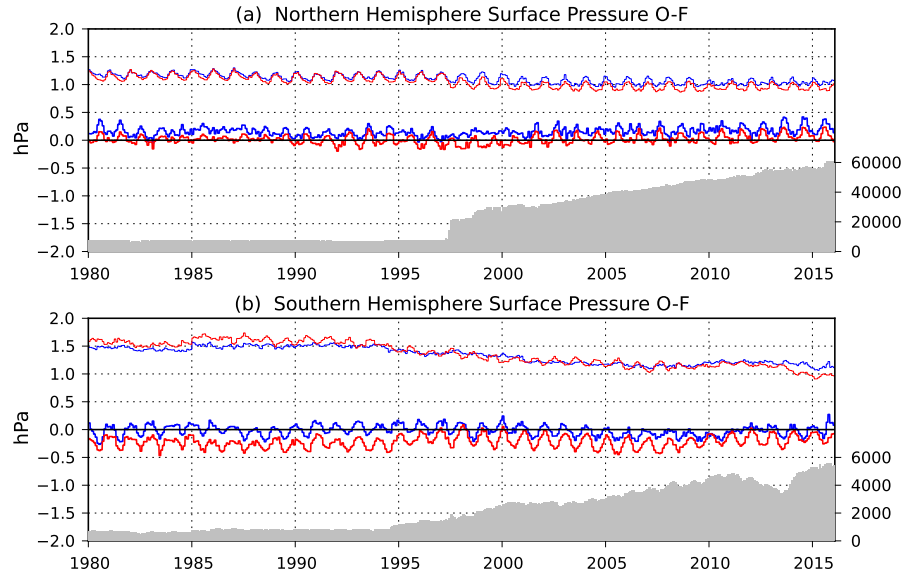


Figure 6: Monthly mean (thick lines) and RMS (thin lines) background departures for surface pressure observations assimilated in MERRA (blue) and MERRA-2 (red). Results are shown for the (a) Northern Hemisphere and (b) Southern Hemisphere. The units are hPa. Also shown are the corresponding monthly mean counts of surface pressure observations assimilated in MERRA-2 (gray shaded).

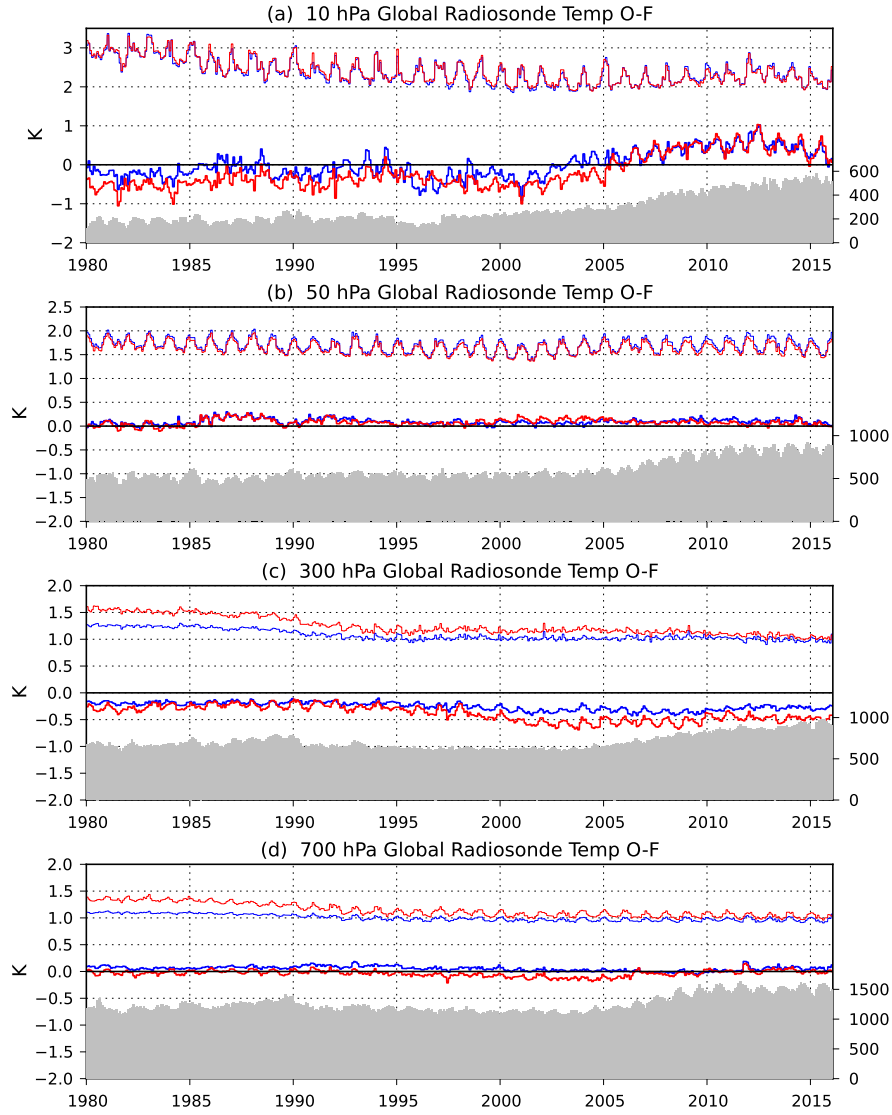


Figure 7: Global monthly mean (thick lines) and RMS (thin lines) background departures for radiosonde temperature observations assimilated in MERRA (blue) and MERRA-2 (red). Results are shown for the pressure levels (a) 10 hPa, (b) 50 hPa, (c) 300 hPa and (d) 700 hPa. The units are K. Also shown are the corresponding monthly mean counts of radiosonde temperature observations assimilated in MERRA-2 (gray shaded).

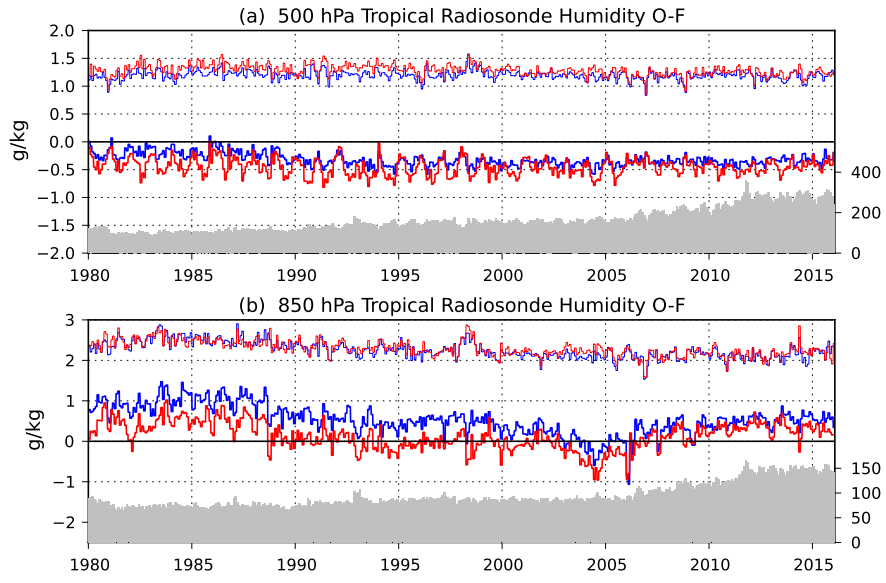


Figure 8: As in Figure 7, except for radiosonde specific humidity observations in the tropics (20°N – 20°S) at (a) 500 hPa and (b) 850 hPa. The units are g kg^{-1} .

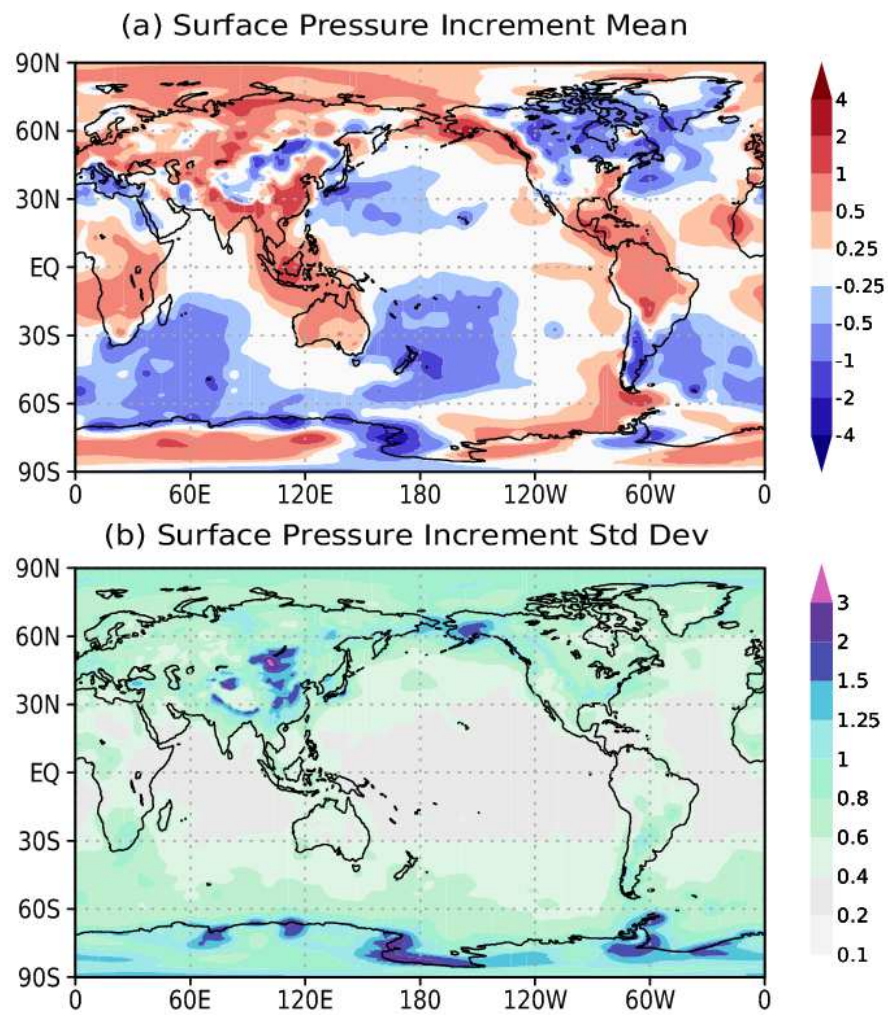


Figure 9: (a) Mean and (b) standard deviation of the monthly mean analysis tendency of surface pressure for the period January 1980 through December 2015. Monthly mean values are based on four synoptic times daily. The units are hPa day^{-1} . Results are derived from the data collection described in GMAO (2015k).

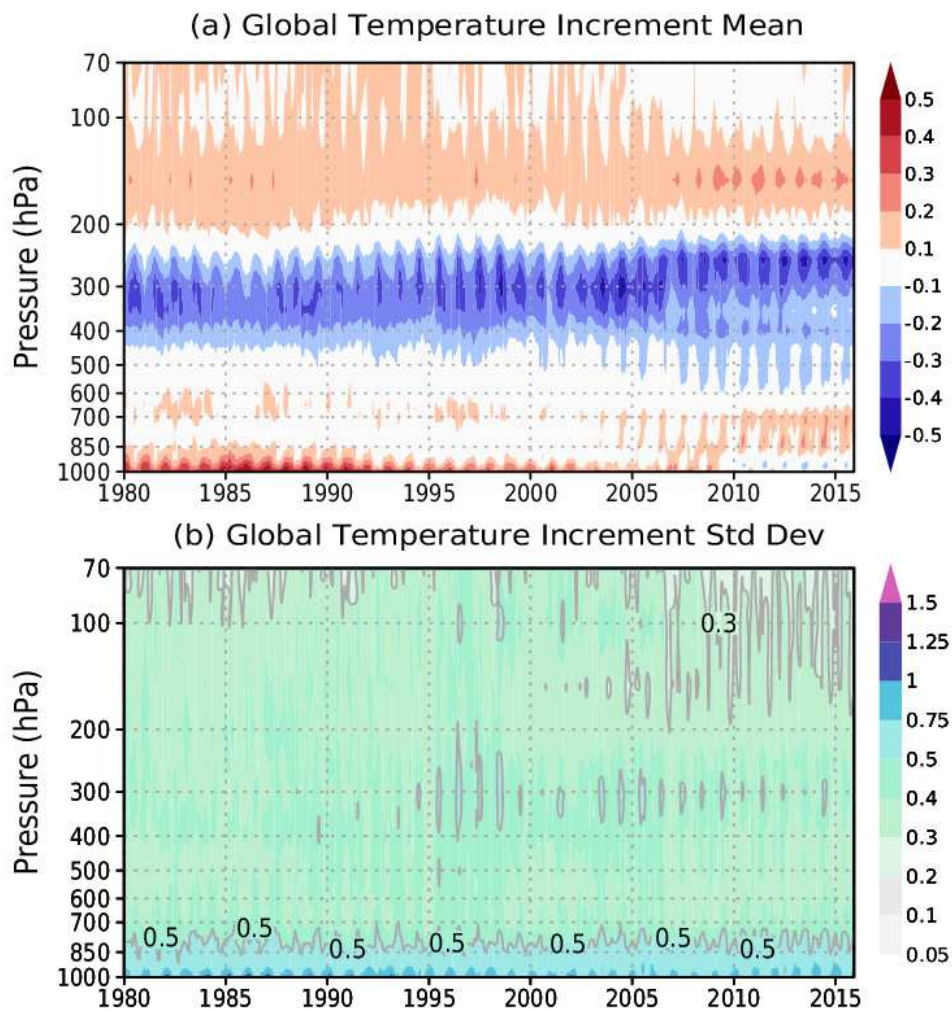


Figure 10: Global (a) mean and (b) standard deviation of the monthly mean analysis tendency of temperature from 1000 to 70 hPa. Monthly means values are based on four synoptic times daily. The units are K day⁻¹. Results are derived from the data collection described in GMAO (2015n).

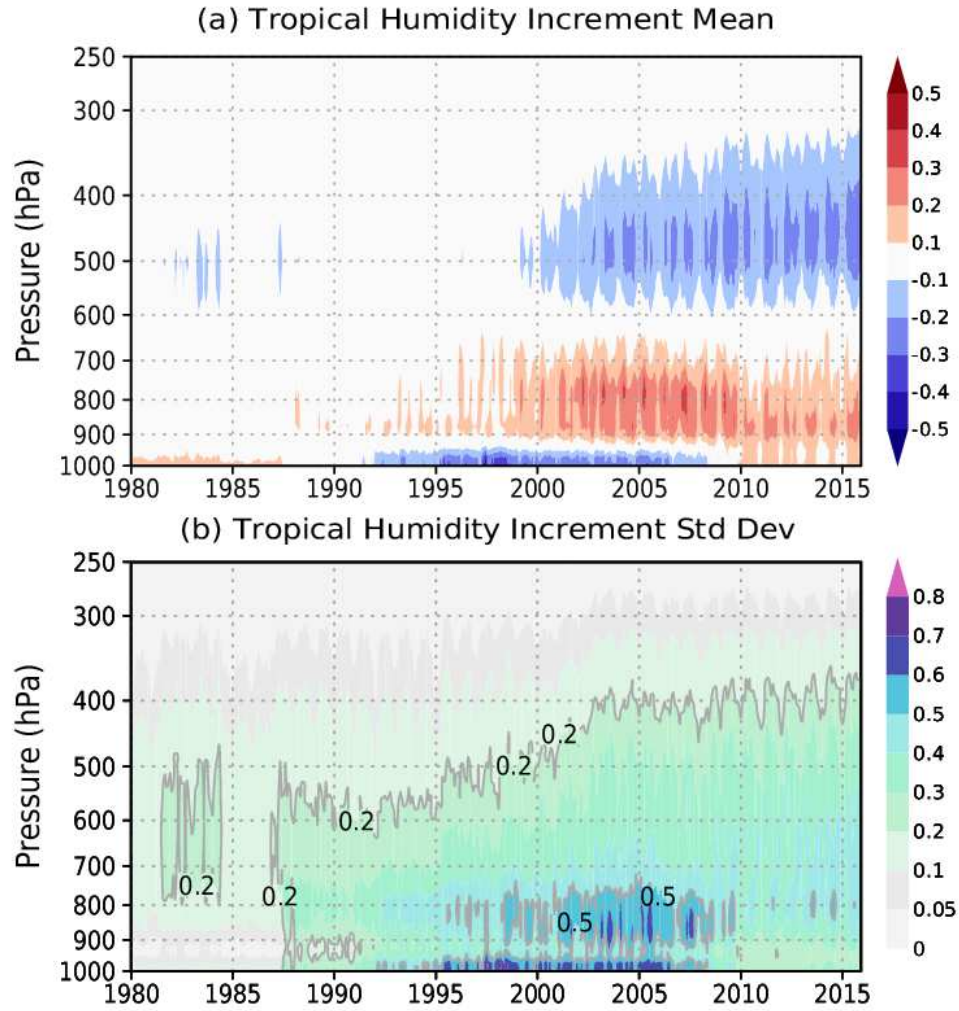


Figure 11: As in Figure 10, except for specific humidity in the tropics (20°N–20°S) from 1000 to 250 hPa. The units are $\text{g kg}^{-1} \text{ day}^{-1}$. Results are derived from the data collection described in GMAO (2015l).

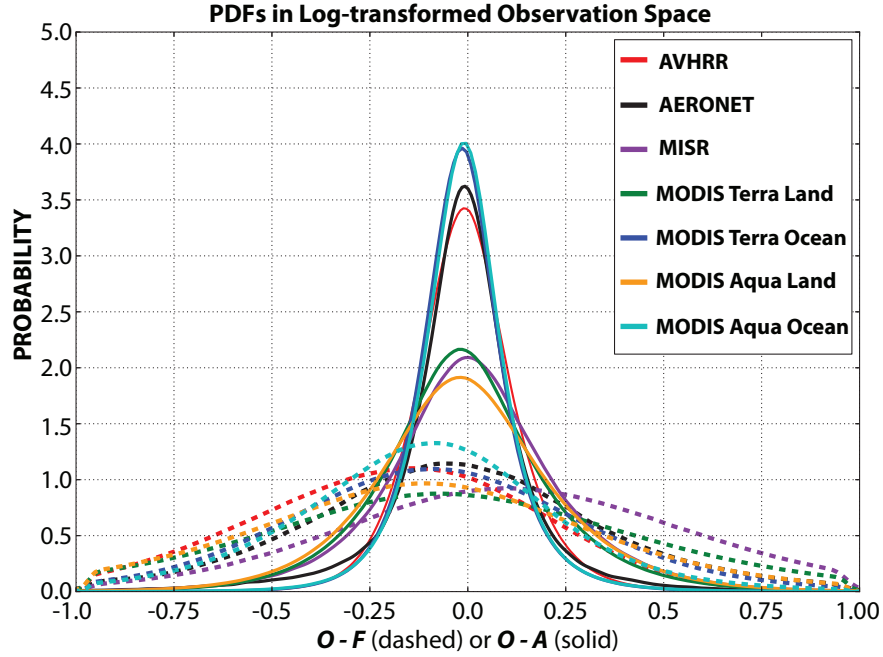


Figure 12: Probability distribution functions (PDFs) of observation minus forecast (O-F, dashed) and observation minus analysis (O-A, solid) differences in observation space, collocated in space and time for each sensor in the MERRA-2 aerosol observing system. The PDFs are calculated from innovation data in log-transformed space ($\ln(\text{AOD}+0.01)$) to ensure distributions are positive and Gaussian. The time periods considered include AVHRR (1993–1999), MODIS Terra (2001–2014), MODIS Aqua (2003–2014), MISR (2001–2012), and AERONET (ANET 2000–2013).

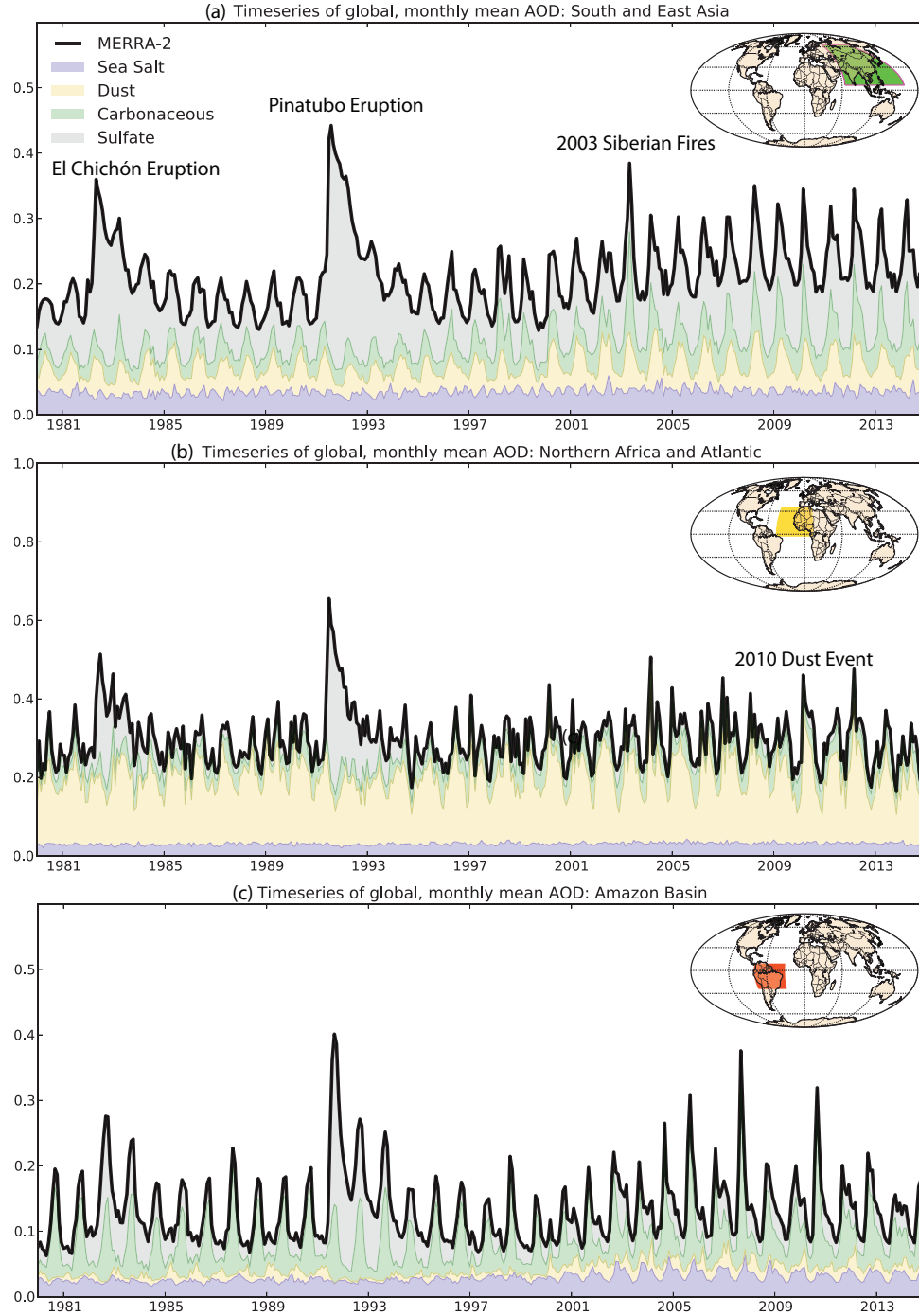


Figure 13: Time series of area-weighted aerosol optical depth (AOD) from the MERRA-2 aerosol reanalysis averaged over major aerosol source regions: (a) South and East Asia $[5^{\circ}\text{N}–55^{\circ}\text{N}, 65^{\circ}\text{W}–160^{\circ}\text{W}]$, (b) northern Africa $[2.5^{\circ}\text{S}–30^{\circ}\text{N}, 45^{\circ}\text{W}–15^{\circ}\text{E}]$, and (c) the Amazon Basin in South America $[20^{\circ}\text{S}–7.5^{\circ}\text{N}, 80^{\circ}\text{W}–30^{\circ}\text{W}]$. The total AOD (thick black line) is the sum of contributions from sea salt (blue), dust (yellow), carbonaceous (black and organic carbon, green), and sulfate (grey) AOD. Results are derived from the data collection described in GMAO (2015g).

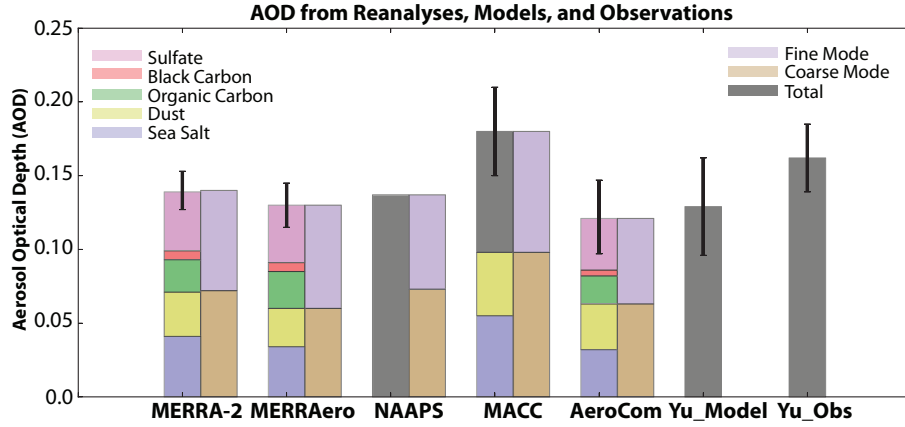


Figure 14: Aerosol optical depth (AOD) from aerosol reanalyses (MERRA-2, MERRAero, NAAPS, MACC), inter-model comparisons (AeroCom Phase I, Yu_Model), and observations (Yu_Obs) for the period 2003–2010. Where available, total AOD is broken down by component species (left bar) and by fine and coarse mode (right bar). For MERRA-2 and MERRAero, the error bar represents the standard deviation of the monthly-mean AOD for the period 2003–2010. For MACC, the error bar is the uncertainty in the total AOD from Bellouin et al. (2013). AeroCom (Kinne et al., 2006) and Yu et al. (2006) uncertainty are the inter-model or inter-observational standard deviations. Coarse mode is defined as the sum of dust plus sea salt AOD, with the remainder of the AOD assigned to the fine mode. Results for MERRA-2 are derived from the data collection described in GMAO (2015g).

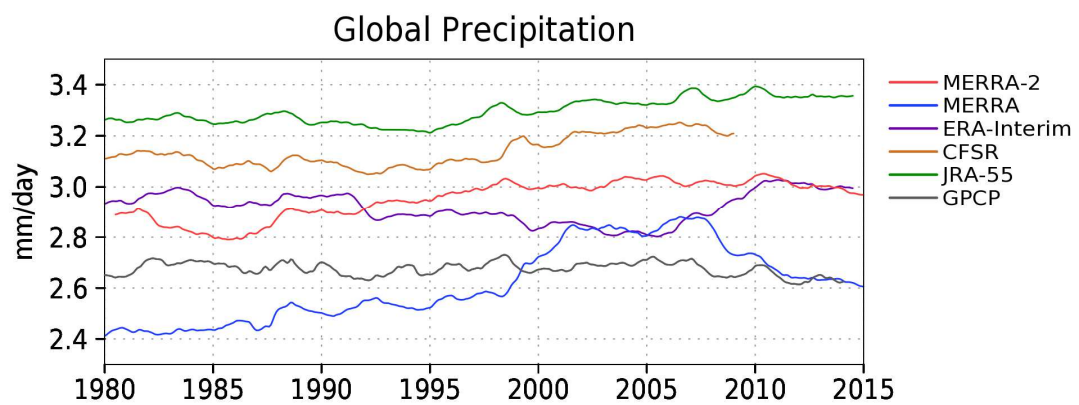


Figure 15: Time series of 12-month running mean globally averaged precipitation for several reanalyses and the GPCP merged gauge satellite data product. The units are mm day^{-1} . Results for MERRA-2 are derived from the data collection described in GMAO (2015h).

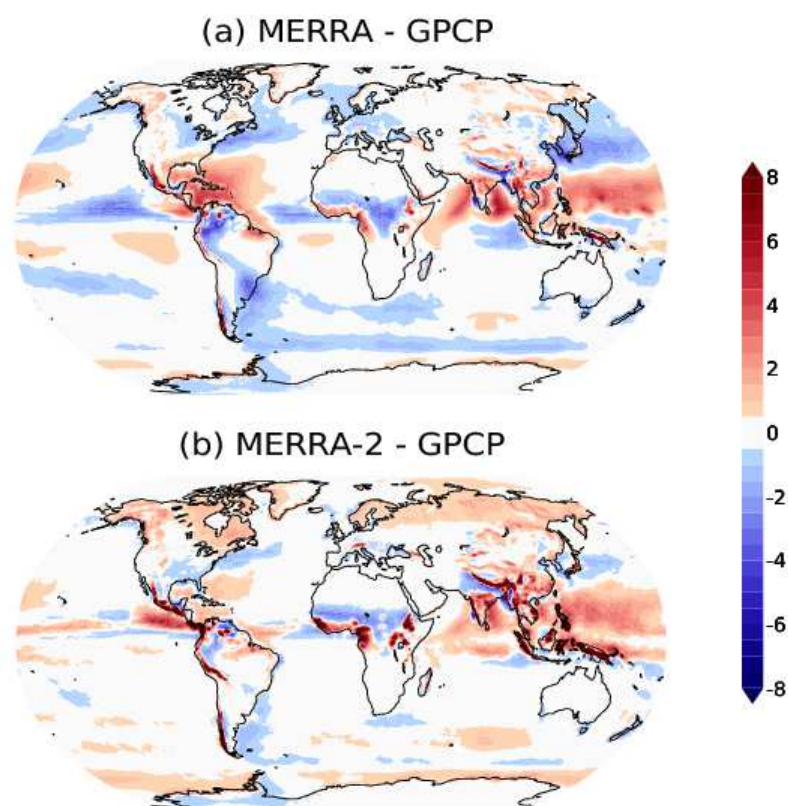


Figure 16: Time-averaged precipitation differences during June-July-August for (a) MERRA minus GPCP and (b) MERRA-2 minus GPCP for the period 1980–2015. The units are mm day^{-1} . Results for MERRA-2 are derived from the data collection described in GMAO (2015h).

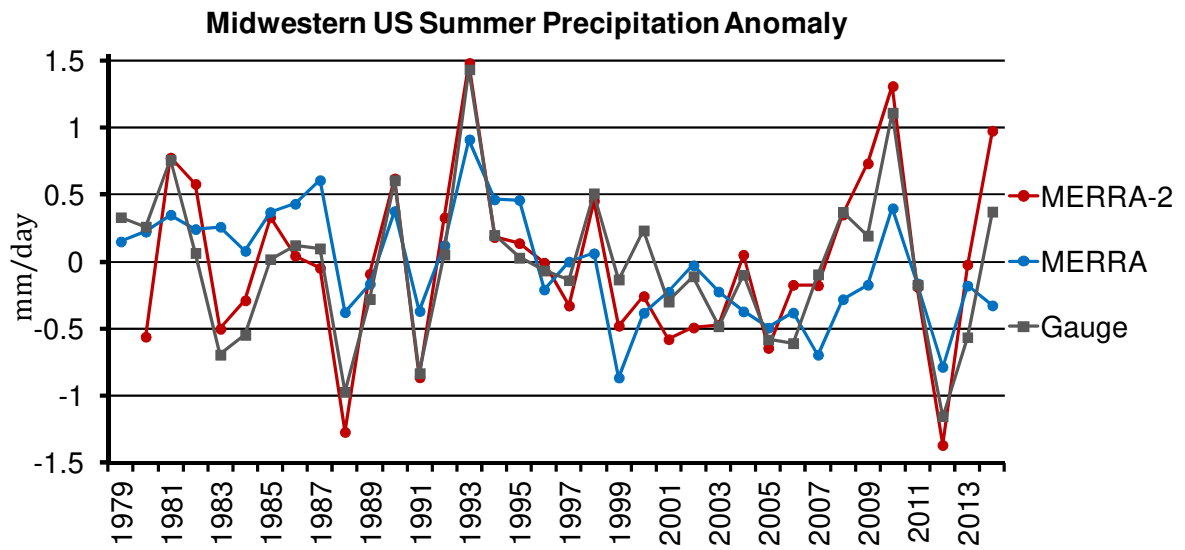


Figure 17: Time series of midwestern US summer seasonal precipitation anomalies, following Bosilovich (2013). The anomalies are computed from the June-July-August mean for the period 1980–2011. The gauge data are from NOAA/CPC gridded daily data for the US (Xie et al. 2007). The units are mm day^{-1} . Results for MERRA-2 are derived from the data collection described in GMAO (2015h).

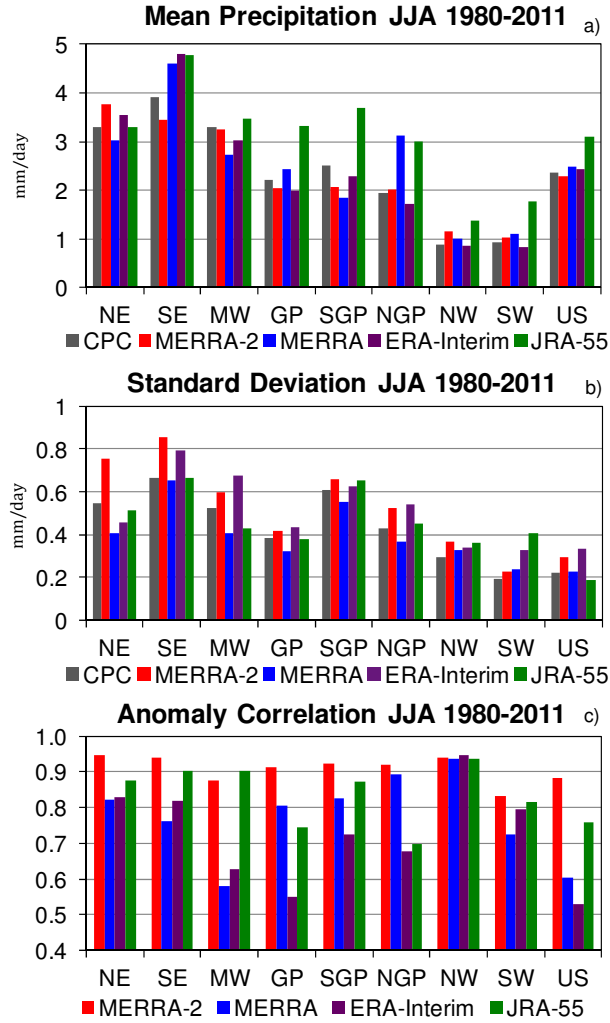


Figure 18: Regional summary statistics for the US summer seasonal anomaly time series of precipitation: (a) mean (mm day^{-1}), (b) standard deviation (mm day^{-1}), and (c) anomaly correlation to CPC gauge observations. The anomalies are computed from the June-July-August mean for the period 1980–2011. The regions lie within the continental US and are defined as in Bosilovich (2013): Northeast (NE), Southeast (SE), Midwest (MW), Great Plains (GP), Southern Great Plains (SGP), Northern Great Plains (NGP), Northwest (NW), Southwest (SW), and the accumulation of all area in these regions (US). Results for MERRA-2 are derived from the data collection described in GMAO (2015h).

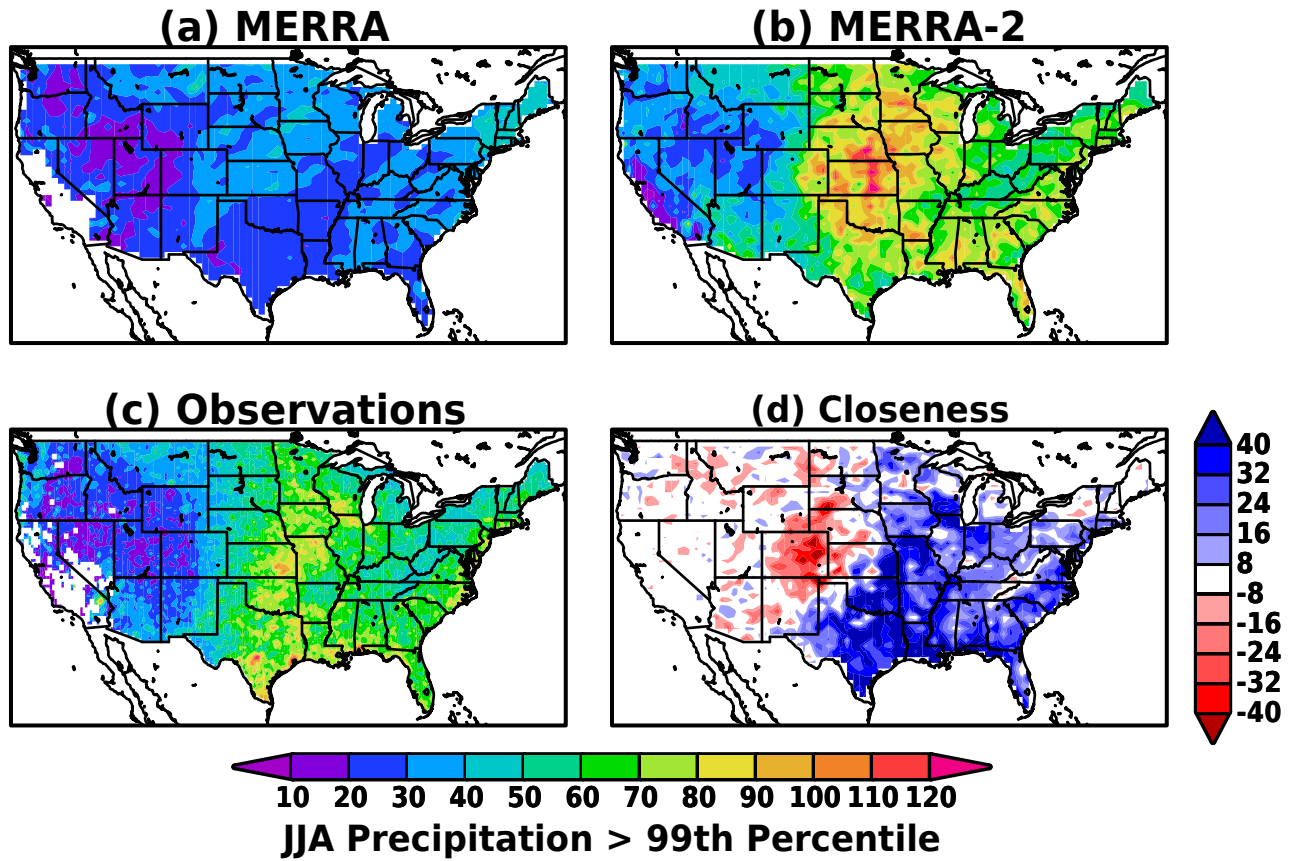


Figure 19: Average amount of precipitation that exceeds the 99th percentile during June-July-August for the period 1980–2013 for (a) MERRA, (b) MERRA-2, and (c) CPC gauge observations. Panel (d) shows the closeness of each reanalysis to the CPC observations for the same period, defined as $|\text{MERRA-2} - \text{CPC}| - |\text{MERRA} - \text{CPC}|$, where the vertical bars indicate absolute differences and the names indicate the set of time-averaged grid-point values for each data type. In (d), blue (red) shades indicate that MERRA-2 (MERRA) is closer to the CPC observations. The units in all panels are mm day^{-1} . Results for MERRA-2 are derived from the data collection described in GMAO (2015d).

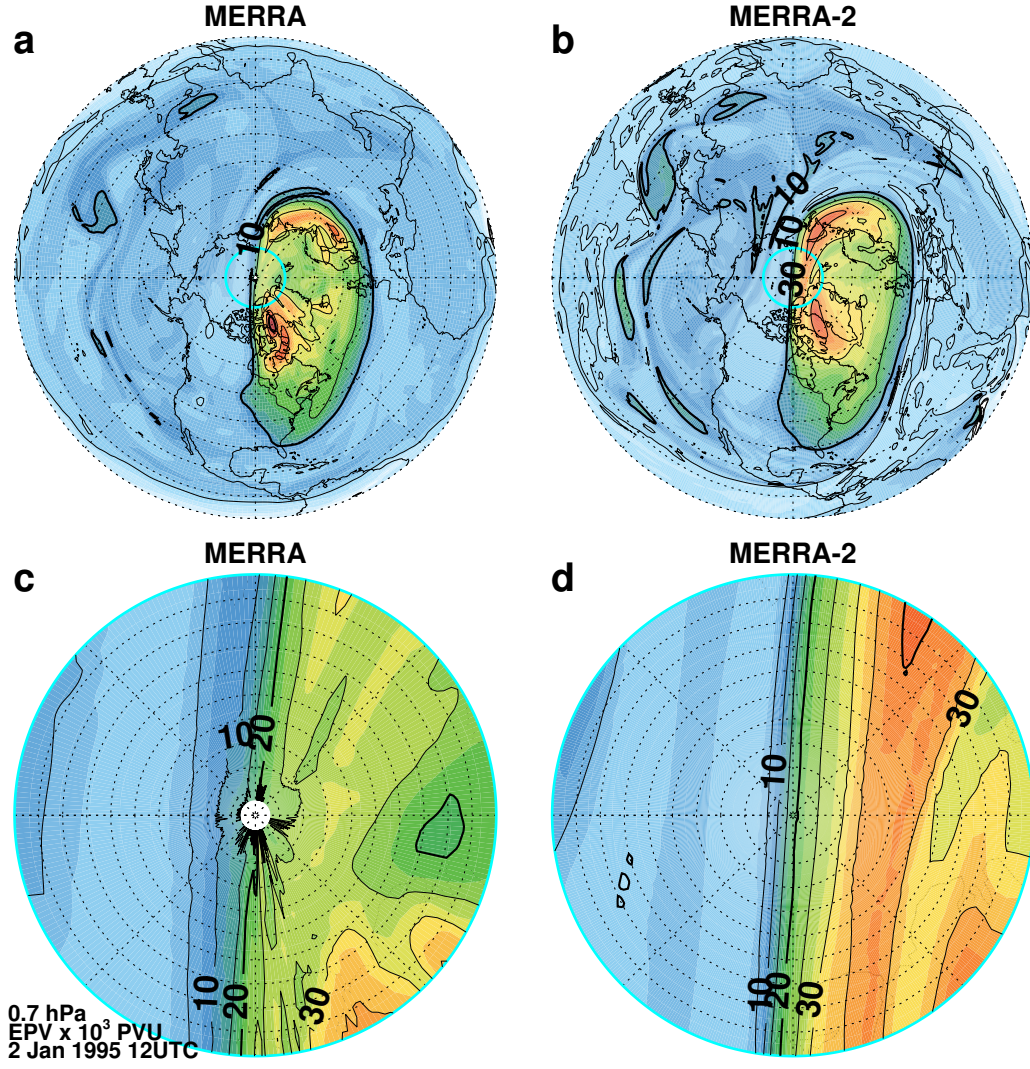


Figure 20: Ertel's potential vorticity (EPV, $\times 10^3$ potential vorticity units, PVU; 1 PVU = $10^{-6} \text{m}^{-2} \text{s}^{-1} \text{K kg}^{-1}$) at 0.7 hPa on 2 January 1995 12 UTC for (a) MERRA and (b) MERRA-2 for the Northern Hemisphere. Polar cap detail (80° – 90° N) for (c) MERRA and (d) MERRA-2. Color shading interval is 2.5×10^3 PVU. Black contour interval is 10×10^3 PVU in (a) and (b) and 5×10^3 PVU in (c) and (d). Cyan circle denotes 80° N latitude. Results are derived from the data collection described in GMAO (2015c).

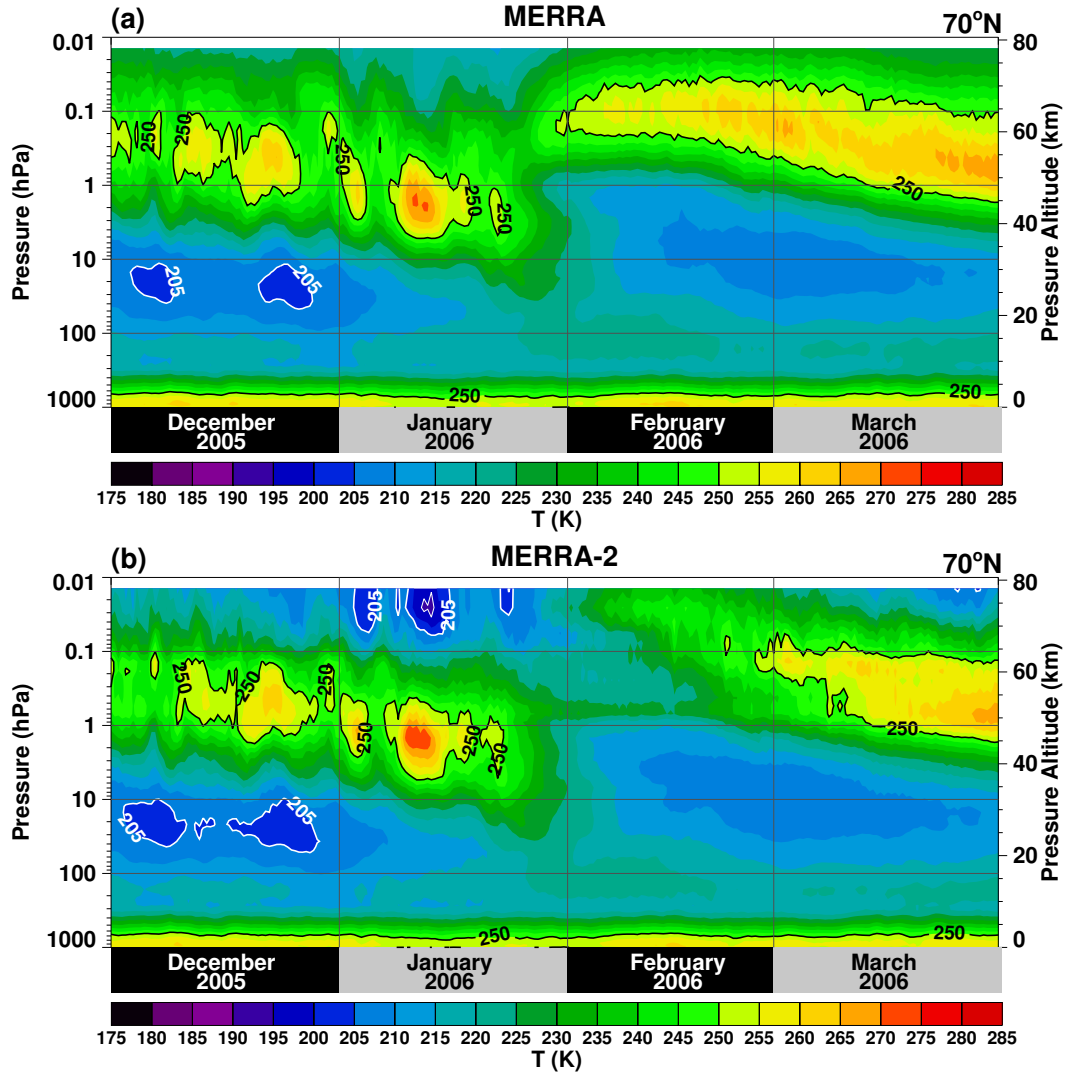


Figure 21: Time-altitude section of zonally averaged temperature at 70°N for (a) MERRA and (b) MERRA-2. The time resolution is twice daily (00 and 12 UTC) for December 2005–March 2006. The contour interval is 5 K.

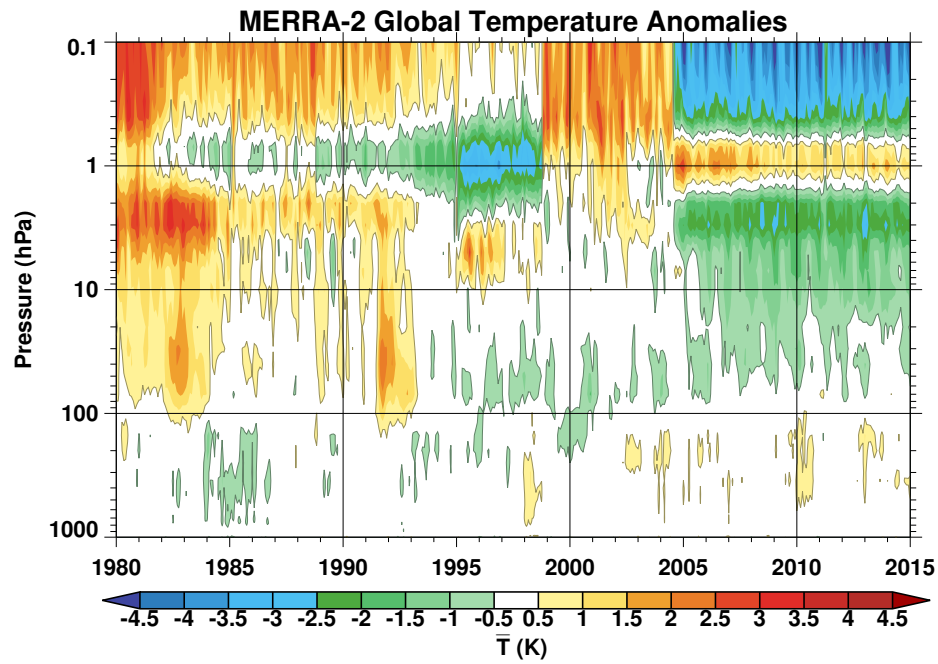


Figure 22: Monthly and globally averaged temperature anomaly for MERRA-2 as a function of time. The annual cycle and mean for 1980–2015 have been removed. The MLS temperatures were introduced at levels above 5 hPa beginning in August 2004. Results are derived from the data collection described in GMAO (2015c).

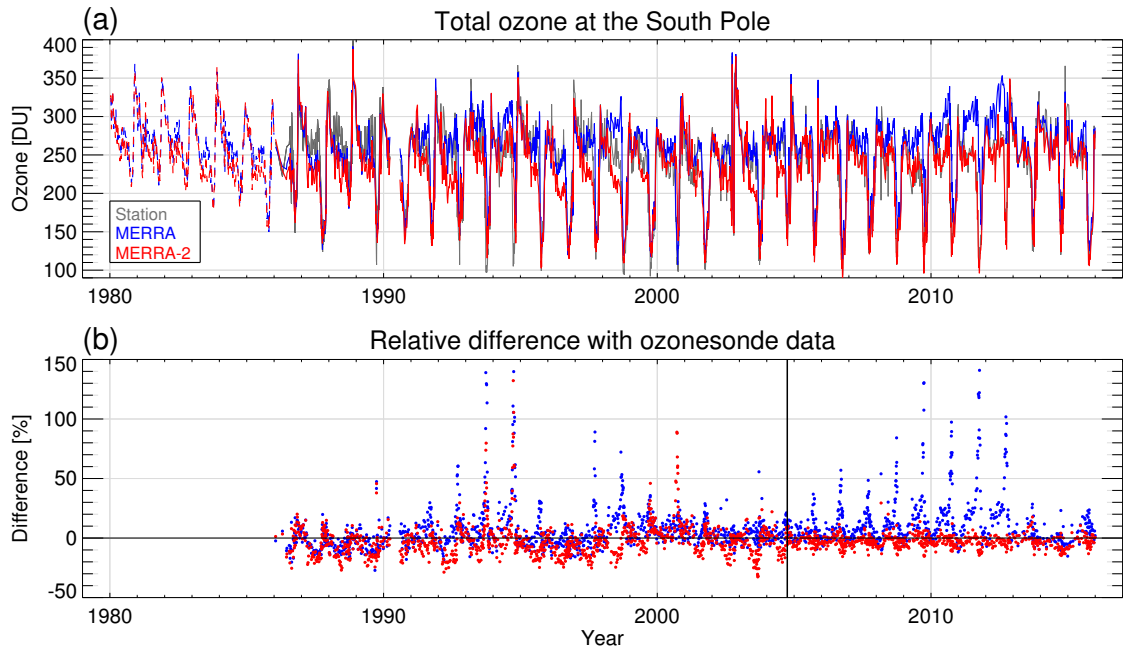


Figure 23: Time series of (a) total ozone (Dobson units, DU) at the South Pole derived from individual ozonesonde measurements (gray) and from collocated values in MERRA (blue) and MERRA-2 (red). Note that ozonesonde measurements are unavailable prior to 1986; see text for details. The reanalysis-minus-ozonesonde differences divided by sonde total ozone are shown in (b) for MERRA (blue) and MERRA-2 (red). The black vertical line in (b) separates the SBUV and Aura periods. (Figure from Wargan et al. 2016.) Results for MERRA-2 are derived from the data collection described in GMAO (2015a).

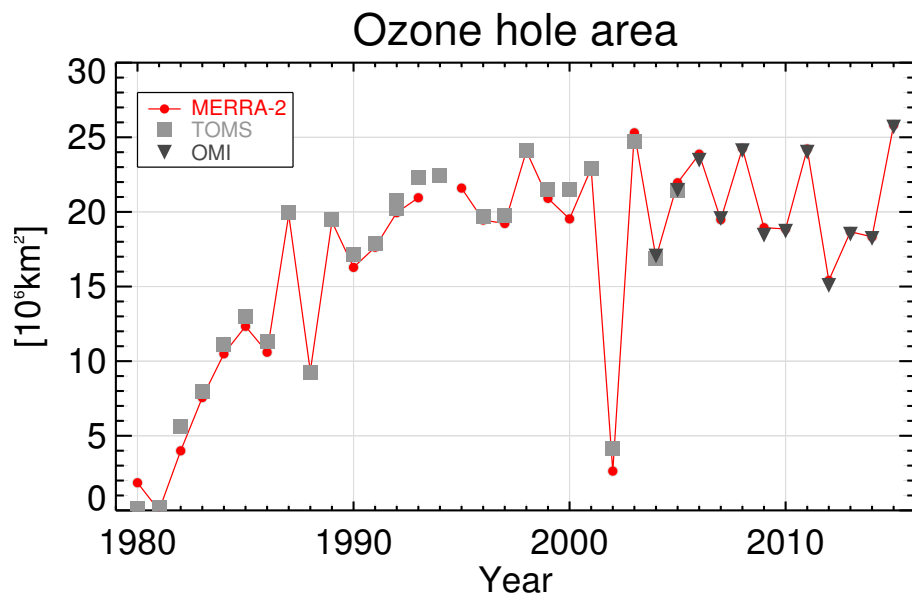


Figure 24: Time series of the Antarctic ozone hole area calculated from MERRA-2 ozone fields averaged between 20 September and 10 October for the years 1980–2015 (red curve with circles). Also shown are values derived from TOMS (gray squares) and OMI (black triangles) observations. The units are 10^6 km^2 . Results for MERRA-2 in 1994 are excluded due to insufficient SBUV data coverage in the Southern Hemisphere, which significantly degraded the analysis; see text for details. Results for MERRA-2 are derived from the data collection described in GMAO (2015a).

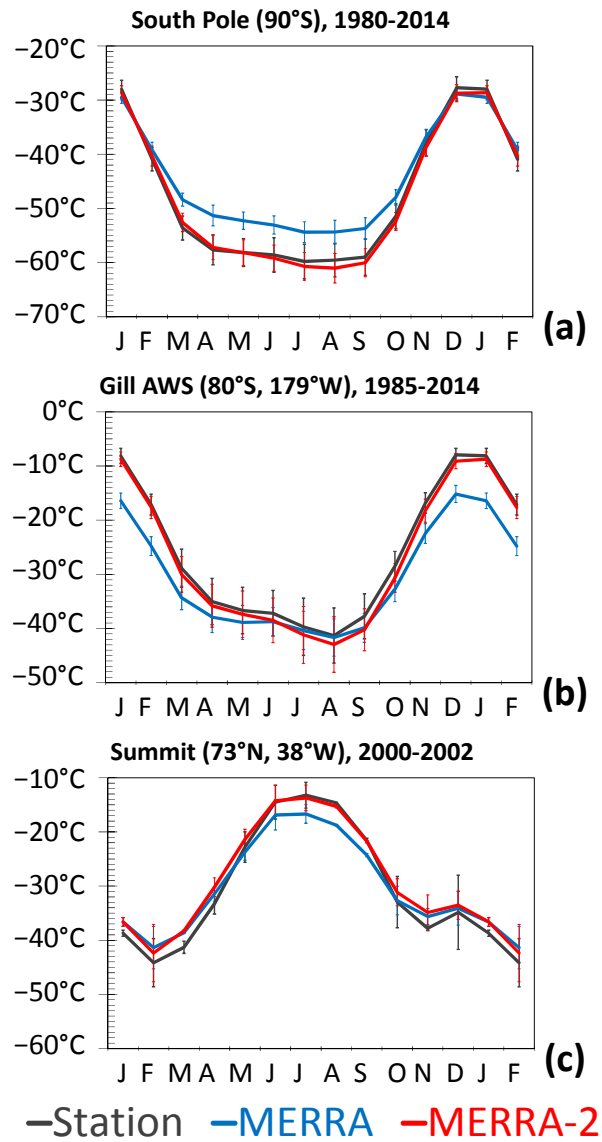


Figure 25: Average annual cycle of 2-m air temperature in MERRA and MERRA-2 at (a) South Pole station (90°S; 1980–2014; Turner et al., 2004), (b) Gill automatic weather station (80°S, 179°W; 1985–2014; Turner et al., 2004), and (c) Summit, Greenland (73°N, 38°W; 2000–2002; Hoch, 2005). The units are °C. Vertical bars denote ± 1 standard deviation of the multi-year time series for each month. Results for MERRA-2 are derived from the data collections described in GMAO (2015i, j, m).

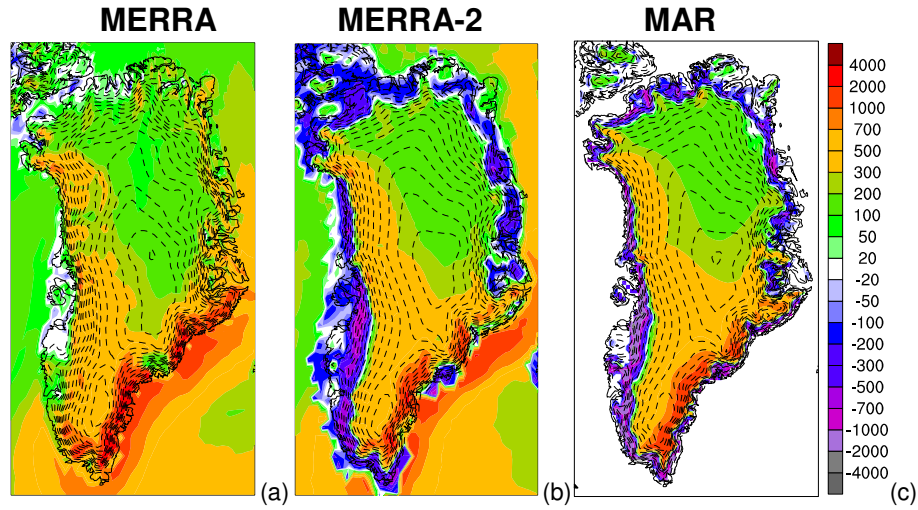


Figure 26: Surface mass balance for the Greenland Ice Sheet for the period 1980–2012 in (a) MERRA, (b) MERRA-2, and (c) MAR regional climate model (Fettweis 2007). The units are mm yr^{-1} water-equivalent. Surface topography (including ice sheet) is contoured with dashed lines every 200 m. Results for MERRA-2 are derived from the data collections described in GMAO (2015i, j, m).